A study on properties of fluorohydrogenate salts and their application as electrolytes for capacitors

Ryosuke Taniki

2013

Contents

II

IV

Chapter 1

General introduction

1.1 Ionic liquids

Ionic liquids (ILs) are liquids composed of only organic and/or inorganic ions. The unique properties often found for ILs are extremely low vapor pressure, non-flammability, excellent thermal and electrochemical stability, wide liquid phase temperature range, high polarity, and catalytic properties [1–4]. These properties enable applications of ILs as stable electrolytes in batteries, capacitors, fuel cells, dye-sensitized solar cells, and electrolytic bath, and as recyclable reaction media for various organic reactions, enzyme reactions, phase separations, and extractions [1–14]. Many efforts have been made to lower the melting temperatures of ionic compounds since handling of traditional inorganic high temperature molten salts is not easy and applications are limited. Nowadays, the salts with relatively low melting temperatures (below 373 K) are widely known. In particular, the salts with melting points below room temperature are called room temperature ionic liquids (RTILs).

Although the first low melting salt, $EtNH_3NO_3$ (melting point: 285 K), was reported by Walden in 1914 [15], detailed studies on ILs had not been done until the development of *N*,*N'*-dialkylimidazolium or *N*-alkylpyridinium halides and halogenoaluminate systems as electrolytes [16–18]. The halogenoaluminate salts have tunable properties such as viscosity, melting point, and acidity by changing the alkyl substituent or the ratio of imidazolium or pyridinium halide to aluminum halides [19]. However, the air-sensitive nature of these halides and halogenoaluminate salts have prevented them from some practical applications. In 1992, Wilkes and Zawarotko reported the first air-stable IL, 1-ethyl-3-methylimidazolium tetrafluoroborate ($EMImBF_4$) with a large electrochemical windows (> 4V), high

conductivities, and high thermal stabilities [20]. This discovery triggered a number of reports obtained by the combination of various cations and anions with a wide variety of properties. Onium cations such as imidazolium, pyridinium, pyrrolidinium, piperidinium, tetraalkylammonium, trialkylsulfonium, and tetraalkylphosphonium are combined with simple halide anions, fluoroanions, and non-fluoroanions such as perfluoroalkyltrifluoroborate (RBF_3^-), hexafluorophosphate (PF_6^-), fluorohydrogenate anions (($FH)_nF^-$), triflate ($CF_3SO_3^-$), bis(fluorosulfonyl)amide (FSA^-), bis(trifluoromethylsulfonyl)amide ($TFSA^-$), nitrate (NO_3^-), nitrite (NO_2^-), thiocyanate (SCN^-), dicyanamide ($N(CN)_2^-$) and tricyanomethanide ($C(CN)_3^-$) [21–27]. Some examples of the cations and anions used in previous studies on ILs are shown in Figures 1–1 and 1–2.

Different cationic structures give a variety of chemical and physical properties [3, 28]. It is indispensable to improve the electrochemical stability of ILs in use as electrolytes since a large applied voltage usually leads to the increase in an energy density of electrochemical devices. Salts of the aromatic cations such as 1,3-dialkylimmidazolium often exhibit low melting points and high conductivities compared to the salts of the nonaromatic cations such as N-alkyl-N-methylpyrrolidinium, whereas the electrochemical stability of 1,3-dialkylimidazolium is lower than that of N-alkyl-N-methylpyrrolidinium possibly because of the high reactivity at the C(2) proton in 1,3-dialkylimmidazolium cation [8, 28–30]. The improvements of the electrochemical and thermal stabilities of ILs are observed by introducing phosphonium cations. However, the high viscosity and low conductivity of the phosphonium ILs are the drawbacks for their application to electrochemical devices [31, 32]. On the other hand, the low viscosity and high ionic conductivity of ILs are obtained by the introduction of trialkylsulfonium cations, whereas the low thermal stability is their drawback [21, 33]. Hydrophobicity is achieved by introducing fluoroalkyl group, and the obtained ILs exhibit low viscosities [34]. An infinite variation of selection and combination of cations and

anions enables the design of the ILs with functions for each application.

Some ILs freeze into mesophases around room temperature, such as ionic plastic crystal or ionic liquid crystal phases [23, 35–42]. A schematic drawing of the phase behavior for the IL, ionic crystal, and mesophases in-between is summarized in Figure 1–3. Ionic plastic crystals are solid and have an isotropic crystal structure where ions are disordered to rotate. Ionic liquid crystals are liquid that have an anisotropic liquid structure where ions are ordered to align.

1.2 Ionic plastic crystals

Ionic liquids based on nonaromatic cations such as pyrrolidinium, tetraalkylammonium, and trialkylsulfonium, sometimes exhibit plastic properties around room temperature [23, 35–38]. These materials based on ionic species have been known as ionic plastic crystals (IPCs), whereas those based on organic molecules, by contrast, have been known as organic PCs. The first systematic study on the PC phase was done by Timmermans in 1961 [43]. Such a phase is an intermediate state formed by first-order solid–solid phase transitions below the melting point. The constituent molecules or ions in the crystal structure are characterized by a long-range positional order with rotating motions. This rotational behavior contributes to the formation of defects, which gives a liquid-like feature such as a fast ion diffusion in either matrix or doped materials and gives plastic mechanical properties [29, 44]. Timmermans proposed a general rule to organic molecules that a PC phase has a low final entropy of fusion ($\Delta S_\mathrm{f} < 20$ J K^{-1} mol^{-1}) since the constituent molecules or ions in the PC phase have already been rotating by solid–solid phase transitions and the entropy change corresponding to the rotational freedom is considered to be very small in the transition from the PC to liquid phase. With increase in temperature, the constituent molecules or ions start to rotate around one molecular axis either suddenly at a phase transition or over a range of temperatures [37]

3

Rotating motions in the PC phases below the melting point increases the entropy of the solid state to the degree close to that of the liquid state, rendering a small ΔS_{fus} compared to that for a fully ordered crystal.

In the IPC phases, the diffusional degree of freedom produces the ion conductivity. For examples, Li_2SO_4 with the IPC phase temperature range between 848 and 1133 K has the rotation of the SO_4^{2-} in the IPC phase, which facilitates the motion of Li^+ via a paddle-wheel mechanism and creates the substantial ion conductivity (~1 S cm^{-1}) at elevated temperatures [45–47]. Ion conduction in the IPC phases at lower temperatures enlarges the application of IPCs and considerable efforts have been made to find inorganic compounds with a low temperature IPC phase such as $LiAlCl_4$ [48]. In contrast, organic compounds often exhibit an IPC phase at low temperatures. The rotating motions of molecules or ions induce the motions of doped ions or matrix to give the potential use of IPCs as a new type of solid-state electrolytes to construct all solid-state electrochemical devices such as particularly lithium rechargeable batteries, dye-sensitized solar cells, and fuel cells [44, 49].

The IPC phase often appears in the case of ILs including the cation with a spherical shape (e.g., *N*-ethyl-*N*-methylpyrrolidinium: EMPyr$^+$) and does not appear in the case of the cation with a planar shape (e.g., EMIm$^+$). The different thermal property between EMPyr$^+$ and EMIm$^+$ is thought to be derived from two factors, the ease of rotating and the slow onset of melting. The cation EMIm$^+$ does seem to rotate around an axis normal to the ring, but it does not. The two substitutions in the EMIm$^+$ with the planar shape of aromatic ring protrude from the ring and may prevent to rotate, while EMPyr$^+$ with the nearly spherical shape may offer a smaller impediment to rotate than EMIm$^+$ as drawn in Figure 1–4. The melting points of ILs based on EMIm$^+$ are lower than those of EMPyr$^+$ and the crystal lattice of EMIm$^+$ based salts decomposes to melt before the rotation of ions begins [36].

Solid-state materials with a high ionic conductivity have been a matter of subject for

people studying electrolytes, since the present liquid electrolytes have some potential problems such as leakage, flammability, and toxicity [50]. Solid polymer electrolytes are interesting candidates to avoid such problems, since they are easy to fabricate into films. On the other hand, the conductivity of solid polymer electrolytes at room temperature is not sufficient enough for practical applications, limited by the chain motions above the glass-transition temperature with the values around 1×10^{-1} mS cm^{-1} [51]. The conductivity of the IPC phases are dramatically increased by several orders of magnitude by adding various lithium salts. For example, the IPC EMPyrTFSA, with a low solid-state conductivity of 10^{-4} mS cm^{-1} in the neat form at 333 K, gives a high conductivity of 2×10^{-1} mS cm^{-1} at 333 K with the addition of 5 mol% LiTFSA [35, 52]. Another example is a molecular PC, succinonitrile with a high solid-state conductivity around 1 mS cm^{-1} at 298 K with the addition of various lithium salts [53]. The molecular PCs have an advantage that the ionic conductivity is originated solely from the addition of the salts in a non-ionic matrix and not from the solvent matrix itself, but still suffer from the disadvantages (e.g., volatility and flammability) owing to the presence of the flammable molecular compounds. On the other hand, the IPCs consist entirely of ions with relatively low melting points and thus have the benefits of ILs, including extremely low vapor pressure and non-flammability, which is favorable for improving safety and reliability of electrochemical devices. Despite these advantages, the solid-state conductivity of 10^{-3} to 10^{-2} mS cm^{-1} at 298 K observed for most reported IPCs with various salts added is not high enough in their practical applications. Although Li-added pyrazolium IPCs show the high solid-state conductivities of 10^{-1} mS cm^{-1} at 298 K, their narrow IPC temperature ranges prevent these IPCs from applications to electrochemical devices [54, 55]. *N*,*N*-diethyl-*N*-methyl-*N*-(*n*-propyl)ammonium trifluoromethyltrifluoroborate (N$_{1223}$CF$_3$BF$_3$) exhibits a wide IPC phase temperature range of 253 to 368 K and solid-state conductivities as high as 10^{-1} to 10^0 mS cm^{-1} by doping small

5

amounts of LiCF$_3$BF$_3$ [38]. This IPC phase is one of the few candidates with the potential use in electrochemical devices such as all solid-state lithium batteries.

1.3 Fluorohydrogenate salts

In 1999, Hagiwara et al. reported 1-ethyl-3-methylimidazolium fluorohydrogenate (EMIm(FH)$_{2.3}$F) possessing a high conductivity of 100 mS cm^{-1} and low viscosity of 4.9 cP at 298 K, as well as a low melting temperature of 208 K [56, 57]. This IL is synthesized by simple metathesis of EMImCl and anhydrous hydrogen fluoride (HF), excess HF and byproduct hydrogen chloride being easily eliminated by pumping at room temperature. The nature of the IL, EMIm(FH)$_{2.3}$F, is nonvolatile, nonflammable, stable in air, and inert against borosilicate glass in spite of the anions containing a HF unit.

The report on EMIm(FH)$_{2.3}$F was followed by a series of fluorohydrogenate ILs combined with various cations. The cationic species used in the known fluorohydrogenate ILs are 1-alkyl-3-methylimidazolium, *N*-alkylpyridinium, *N*-alkyl-*N*-methylpyrrolidinium, *N*-alkyl-*N*-methylpiperidinium, and tetraalkylphosphonium [32, 58, 59]. They exhibit the lower viscosities and higher conductivities by one order of magnitude than those of ILs of the corresponding cation combined with the other anions. These properties lead to the applications as electrolytes in electric double layer capacitors, fuel cells, and dye-sensitized solar cell [12, 60–62].

Fluorohydrogenate anions ((FH)$_n$F$^-$), shown in Figure 1−5, are oligomeric complex ions, where several HF units are bound as ligands to the central fluorine atom. The number "*n*" means the average number of HF in the anion. Figure 1−6 shows the abundance ratio of the anionic species, FHF$^-$, (FH)$_2$F$^-$, and (FH)$_3$F$^-$ in (FH)$_n$F$^-$. Taking EMIm(FH)$_{2.3}$F ionic liquid for example, (FH)$_2$F$^-$ and (FH)$_3$F$^-$ are mixed in the ratio of 7 to 3. Dissociation of HF in these ILs is negligibly small (< 1 Pa) up to a certain temperature by vacuum-pumping these ILs at

the target temperature prior to use. The HF molecule is rapidly exchanging between $(FH)_2F^-$ and $(FH)_3F^-$ according to NMR study [57, 63, 64]. No neutral HF is detectable in the liquid by spectroscopic methods. Since the ^{1}H-NMR and ^{19}F-NMR give single signals and do not distinguish the hydrogen atoms or fluorine atoms in these two anions even at 233 K, HF exchange is considered to occur among the anions in shorter periods than the NMR time resolution [63]. The HF exchanging between the $(FH)_nF^-$ anions behaves like a solvent molecule with a certain dielectric moment to weaken the cation−anion interaction and the anion species actually diffusing in FHILs become small by the release of HF in a very short period as described in Figure 1−7 [64].

As described above, the HF fraction n of $EMIm(FH)_nF$ is stable in 2.3 at 298 K under vacuum. The physicochemical properties of $EMIm(FH)_nF$ depends on the HF content n [65, 66]. The n value is decreased by elimination of HF at elevated temperature, resulting in a more conventional IL with no dissociation of HF. The decrease in n raises their melting point and viscosity and lowers the ionic conductivity due to the stronger electrostatic interactions between the cations and the smaller anions.

1.4 Electrochemical capacitors

Electrochemical capacitors have been actively studied as electrochemical energy storage devices to regenerate energies efficiently in a few seconds [67−72]. Double layer capacitors generally have high power density and long cycle life due to their non-Faradaic charge−discharge mechanism (Figure 1−8). An electrical charge is stored at electric double layer formed between an ionic conductive electrolyte and an electronic conductive electrode with a large surface area. The solvated ions enter the nano-scale pores on the electrode to form the electric double layer and the capacitance C is optimized by the relation between the pore size and ion size [73, 73]. Although great efforts to increase the capacitance of double layer

capacitors have been undertaken by controlling the pore size distribution on the electrode, the capacitance is limited in the reversible electrostatic charging storage system due to the limited surface area. Performance of capacitors is evaluated by the power density of IV and energy density of $1/2CV^2$, where I and V mean the current density and operation voltage which has a large correlation with electrochemical stability of electrolytes [75]. Aqueous electrolytes exhibit a high conductivity (e.g., 800 mS cm^{-1} for a sulfuric acid) and give a high power density (~10^6 W L^{-1}), while their low electrochemical stability results in a low energy density (~1 Wh L^{-1}) [71]. On the other hand, non-aqueous electrolytes, typically organic electrolytes, exhibit a lower conductivity (~10 mS cm^{-1}) than that of aqueous electrolytes, but they have a wide electrochemical stability, affording the high energy density in electrochemical capacitors (often 10 times higher than that of aqueous electrolytes) [71, 76, 77].

Another type of electrochemical capacitor, pseudocapacitor, has also been widely studied. Charge storage of pseudocapacitor is based on reversible electrochemical reactions on redox active electrodes such as metal oxides (RuO_2, Fe_3O_4, and MnO_2) [78–83] and electrically conductive polymers (polyaniline and polythiophene) [84, 85]. These materials exhibit fast charge transfer reactions and high diffusivity of redox active species in electrodes. Metal oxides (hydroxides) give a large capacitance (e.g., 800 F g^{-1} for RuO_2) [78] by the surface adsorption and insertion of protons in aqueous electrolytes, while the operation voltage is limited to 1 V. Electrochemical capacitors using conductive polymers exhibit high charging voltage (~3 V) and high energy density (~ several dozens Wh kg^{-1}) [86].

Room temperature ionic liquids (RTILs) are attractive electrolytes to replace the conventional organic and aqueous electrolytes in electrochemical devices owing to their unique properties as described above [3, 6, 9, 87, 88]. The properties enhance the safety issues which are important in the large-scale applications. Electrochemical capacitors using RTILs have a performance comparable to organic electrolytes, while a drawback for conventional

RTILs is their low ionic conductivity as in the cases of most organic electrolytes. Highly conductive electrolytes offer a low internal resistance of electrochemical devices, giving a large power density, and low melting points enable an operation at low temperature (e.g., even at 233 K) [60, 61].

1.5 Aim of this study

This study deals with syntheses and characterization of the salts containing fluorohydrogenate anions and several cations, pyrrolidinium cations, azoniaspiro-type cations, sulfonium cations, and polyfluoroalkylated imidazolium cations, and deals with the applications to electrochemical capacitors using fluorohydrogenate salts as electrolytes. In chapter 2, apparatus and techniques required for their syntheses and handling are described

In chapter 3, the physicochemical, structural, and electrochemical properties of new IPCs composed of $(FH)_2F^-$ and N,N-dimethylpyrrolidinium $(DMPyr^+)$ or N-ethyl-N-methylpyrrolidinium $(EMPyr^+)$ cations are described. The diffusion mechanism in the fluorohydrogenate IPC phase is discussed.

In chapter 4, the effects of the HF content in $DMPyr(FH)_nF$ and $EMPyr(FH)_nF$ on their thermal and structural properties are described, followed by the discussion about the effect of cation structure on the IPC phase.

In chapter 5, the physicochemical, structural, and electrochemical properties of new fluorohydrogenate salts based on azoniaspiro-type cations are described. Effects of the carbon number of alkyl chain and introduction of oxygen atom in the azoniaspiro-type cations on their physicochemical properties are discussed.

In chapter 6, the physicochemical, structural and electrochemical properties of new trialkylsulfonium fluorohydrogenate salts are described. Effects of cationic structure and alkyl chain length on physicochemical properties of the ILs are discussed

In chapter 7, the physicochemical, structural and electrochemical properties of new fluorohydrogenate salts based on polyfluoroalkylated imidazolium cations are described. The effect of fluorine atoms in the side chain on physicochemical properties of the ILs are discussed.

In chapter 8, the electrochemical behavior of activated carbon electrodes in FHIL EMPyr(FH)$_{2.3}$F is investigated by separately monitoring the positive and negative electrode potentials. The double layer and redox capacitances are quantitatively separated by the impedance measurement and charge–discharge test at different voltages.

In chapter 9, the electrochemical capacitors using fluorohydrogenate IPC (DMPyr(FH)$_2$F) are characterized. The effect of replacement of electrolytes from FHIL to fluorohydrogenate IPC as the solid-state electrolyte is discussed.

In chapter 10, the studies in this thesis are summarized and the future prospective is given.

References

[1] J. S. Wikes, *Green Chemistry* **2002**, *4*, 73.

[2] K. R. Seddon, *J. Chem. Tech. Bioethnol.* **1997**, *68*, 351.

[3] R. Hagiwara, Y. Ito, *J. Fluorine Chem.* **2000**, *105*, 221.

[4] H. Xue, R. Verma, J. M. Shreeve, *J. Fluorine Chem.* **2006**, *127*, 159.

[5] M. Armand, F. Endres, D. R. MacFarlane, H. Ohno, B. Scrosati, *Nat. Mater.* **2009**, *8*, 621.

[6] T. Tsuda, C. L. Hussey, *Electrochem. Soc. Interface* **2007**, *Spring*, 42.

[7] M. Ue, M. Takeda, T. Takahashi, M. Takehara, *Electrochem. Solid-State Lett.* **2002**, *5*, A119.

[8] A. B. McEwen, H. L. Ngo, K. LeCompte, J. L. Goldman, *J. Electrochem. Soc.* **1999**, *146*, 1687.

[9] T. Welton, *Chem. Rev.* **1999**, *99*, 2071.

[10] S. G. Cull, J. D. Holbrey, V. Vargas-Mora, K. R. Seddon, G. J. Lye, *Biotechnol. Bioeng.* **2000**, *69*, 227.

[11] P. Wasserscheid, W. Keim, *Angew. Chem. Int. Ed.* **2000**, *39*, 3772.

[12] R. Hagiwara, T. Nohira, K. Matsumoto, Y. Tamba, *Electrochem. Solid-State Lett.* **2005**, *8*, A231.

[13] C. Nanjundiah, S. F. McDevitt, V. R. Koch, *J. Electrochem. Soc.* **1997**, *144*, 3392.

[14] R. D. Rogers, K. R. Seddon, *Science* **2003**, *302*, 792.

[15] P. Walden, *Bull. Acad. Imper. Sci.* (*St. Petersburg*) **1914**, 1800.

[16] E. M. Arnett, J. F. Wolf, *J. Am. Chem. Soc.* **1975**, *97*, 3264.

[17] J. Robinson, R. A. Osteryoung, *J. Am. Chem. Soc.* **1979**, *101*, 323.

[18] J. S. Wilkes, J. A. Levisky, R. A. Wilson, C. L. Hussey, *Inorg. Chem.* **1982**, *21*, 1263.

[19] R. J. Gale, R. A. Osteryoung, *Inorg. Chem.* **1979**, *18*, 1603.

[20] J. S. Wilkes, M. J. Zaworotko, *J. Chem. Soc., Chem. Commun.* **1992**, *13*, 965.

[21] Z-B. Zhou, H. Matsumoto, K. Tatsumi, *Chem. Eur. J.* **2004**, *10*, 6581.

[22] S. N. V. K. Aki, J. F. Brennecke, A. Samanta, *Chem. Commun.* **2001**, *5*, 413.

[23] H.-B. Han, J. Nie, K. Liu, W.-K. Li, W.-F. Feng, M. Armand, H. Matsumoto, Z.-B. Zhou, *Electrochim. Acta.* **2010**, *55*, 1221.

[24] M. J. Muldoon, C. M. Gordon, I. R. Dunkin, *J. Chem. Soc. Perkin trans.* **2001**, *2*, 433.

[25] Q. Zhou, W. A. Henderson, G. B. Appetecchi, M. Montanino, S. Passerini, *J. Phys. Chem. B* **2008**, *112*, 13577.

[26] D. R. MacFarlane, J. Golding, S. Forsyth, M. Forsyth, G. B. Deacon, *Chem. Commun.* **2001**, *16*, 1430.

[27] S. Forsyth, S. R. Batten, Q. Dai, D. R. MacFarlane, *Aust. J. Chem.* **2004**, *57*, 121.

[28] H. Tokuda, K. Ishii, M. A. B. H. Susan, S. Tsuzuki, K. Hayamizu, M. Watanabe, *J. Phys. Chem. B* **2006**, *110*, 2833.

[29] D. R. MacFarlane, P. Meakin, J. Sun, N. Amini, M. Forsyth, *J. Phys. Chem. B* **1999**, *103*, 4164.

[30] D. R. McFarlane, J. Sun, J. Golding, P. Meakin, M. Forsyth, *Electrochim. Acta*, **2000**, *45*, 1271.

[31] K. Tsunashima, A. Kawabata, M. Matsumiya, S. Kodama, R. Enomoto, M. Sugiya, Y. Kunugi, *Electrochem. Commun.* **2011**, *13*, 178.

[32] S. Kanematsu, K. Matsumoto, R. Hagiwara, *Electrochem. Commun.* **2009**, *11*, 1312.

[33] L. Yang, Z.-X. Zhang, X.-H. Gao, H.-Q. Zhan, K. Mashita, *J. Power Sources* **2006**, *162*, 614.

[34] H. Xue, J. M. Shreeve, *Eur. J. Inorg. Chem.* **2005**, *13*, 2573.

[35] D. R. MacFarlane, J. Huang, M. Forsyth, *Nature* **1999**, *402*, 792.

[36] D. R. MacFarlane, P. Meakin, N. Amini, M. Forsyth, *J. Phys.: Condens. Matter* **2001**, *13*,

8257.

[37] L. Jin, K. M. Nairn, C. M. Forsyth, A. J. Seeber, D. R. MacFarlane, P. C. Howlett, M. Forsyth, J. M. Pringle, *J. Am. Chem. Soc*. **2012**, *134*, 9688.

[38] Z. Zhou, H. Matsumoto, *Electrochem. Commun*. **2007**, *9*, 1017.

[39] Binnemans, K. *Chem. Rev.* **2005**, *105*, 4148.

[40] M. Yoshio, T. Kagata, K. Hoshino, T. Mukai, H. Ohno, T. Kato, *J. Am. Chem. Soc.* **2006**, *128*, 5570.

[41] T. Kato, *Science* **2002**, *295*, 2414.

[42] F. Xu, K. Matsumoto, R. Hagiwara, *Chem. Eur. J.* **2010**, *16*, 12970.

[43] J. Timmermans, *J. Phys. Chem. Solids* **1961**, *18*, 1.

[44] D. R. MacFarlane, M. Forsyth, *Adv. Mater*. **2001**, *13*, 957.

[45] R. Aronsson, B. Jansson, H. E. G. Knape, A. Lundén, L. Nilsson, C.-A. Sjöblom, L. M. Torell, *J. Phys. Colloq.* **1980**, *41*, C6.

[46] R. Aronsson, H. E. G. Knape, L. M. Torell, *J. Chem. Phys*. **1982**, *77*, 677.

[47] L. Börjesson, L. M. Torell, *Phys. Rev.* **1985**, *32*, 2471.

[48] W. Weppner, R. A. Huggins, *J. Electrochem. Soc.* **1977**, *124*, 35.

[49] J. M. pringle, P. C. Howlett, D. R. MacFarlane, M. Forsyth, *J. Mater. Chem*. **2010**, *20*, 2056.

[50] C. Masquelier, *Nat. Mater.* **2011**, *10*, 649.

[51] A. Nishimoto, K. Agehara, N. Furuya, T. Watanabe, M. Watanabe, *Macromolecules* **1999**, *32*, 1541.

[52] M. Forsyth, J. Huang, D. R. MacFarlane, *J. Mater. Chem.* **2000**, *10*, 2259.

[53] P.-J. Alarco, Y. Abu-Lebdeh, A. Abouimrane, M. Armand, *Nat. Mater*. **2004**, *3*, 476.

[54] P.-J. Alarco. Y. Abu-Lebdeh, N. Ravet, M. Armand, *Solid State Ionics* **2004**, *172*, 53.

[55] P.-J. Alarco. Y. Abu-Lebdeh, M. Armand, *Solid State Ionics* **2004**, *175*, 717.

[56] R. Hagiwara, T. Hirashige, T. Tsuda, Y. Ito, *J. Fluorine Chem.* **1999**, *99*, 1.

[57] R. Hagiwara, T. Hirashige, T. Tsuda, Y. Ito, *J. Electrochem. Soc.* **2002**, *149*, D1.

[58] K. Matsumoto, R. Hagiwara, Y. Ito, *Electrochem. Solid-State Lett*. **2004**, *7*, E41.

[59] M. Yamagata, S. Konno, K. Matsumoto, R. Hagiwara, *Electrochem. Solid-State Lett*. **2009**, *12*, F9.

[60] M. Ue, M. Takeda, A. Toriumi, A. Kominato, R. Hagiwara, Y. Ito, *J. Electrochem. Soc*. **2003**, *150*, A499.

[61] A. Senda, K. Matsumoto, T. Nohira, R. Hagiwara, *J. Power Sources* **2010**, *195*, 4414.

[62] H. Matsumoto, T. Matsuda, T. Tsuda, R. Hagiwara, Y. Ito, Y. Miyazaki, *Chem. Lett.* **2001**, 26.

[63] Y. Saito, K. Hirai, K. Matsumoto, R. Hagiwara, Y. Minamizaki, *J. Phys. Chem. B* **2005**, *109*, 2942.

[64] T. Enomono, Y. Nakamori, K. Matsumono, R. Hagiwara, *J. Phys. Chem. C* **2011**, *115*, 4324.

[65] R. Hagiwara, Y. Nakamori, K. Matsumoto, Y. Ito, *J. Phys. Chem. B* **2005**, *109,* 5445.

[66] F. Xu, K. Matsumoto, R. Hagiwara, *J. Phys. Chem. B* **2012**, *116*, 10106.

[67] P. Simon, Y. Gogotsi, *Nat*. *Mater.* **2008**, *7*, 845.

[68] Y. Gogotsi, P. Simon, *Science* **2011**, *334*, 917.

[69] J. R. Miller, P. Simon, *Science* **2008**, *321*, 651.

[70] A. Chu, P. Braatz, *J. Power Sources* **2002**, *112*, 236.

[71] B. E. Conway, *Electrochemical Supercapacitors: Scientific Fundamentals and Technological Applications*, Kluwer Academic/Plenum, New York, **1999**.

[72] E. Frackowiak, F. Béguin, *Carbon* **2001**, *39*, 937.

[73] C. Largeot, C. Portet, J. Chmiola, P.-L. Taberna, Y. Gogotsi, P. Simon, *J. Am. Chem. Soc*. **2008**, *130*, 2730.

[74] C. Portet, G. Yushin, Y. Gogotsi, *J. Electrochem. Soc.* **2008**, *155*, A531.

[75] K. Xu, M. S. Ding, T. R. Jow, *Electrochim. Acta* **2001**, *46*, 1823.

[76] M. Ue, M. Takeda, M. Takehara, S. Mori, *J. Electrochem. Soc.* **1997**, *144*, 2684.

[77] M. Ue, K. Ida, S. Mori, *J. Electrochem. Soc.* **1994**, *141*, 2989.

[78] K. Naoi, S. Ishimoto, N. Ogihara, Y. Nakagawa, S. Hatta, *J. Electrochem. Soc.* **2009**, *156*, A52.

[79] S. Ardizzone, G. Fregonara, S. Trasatti, *Electrochim. Acta* **1990**, *35*, 263.

[80] N.-L. Wu, S.-Y. Wang, C.-Y. Han, D.-S. Wu, L.-R. Shiue, *J. Power Sources*, **2003**, *113*, 173.

[81] T. Brousse, D. Bélanger, *Electrochem. Solid-State Lett.* **2003**, *6*, A244.

[82] T. Brousse, M. Toupin, R. Dugas, L. Athouël, O. Crosnier, D. Bélanger, *J. Electrochem. Soc.* **2006**, *153*, A2171.

[83] M. Toupin, T. Brousse. D. Bélanger, *Chem. Mater*. **2004**, *16*, 3184.

[84] A. Rudge, J. Davey, I. Raistrick, S. Gottersfeld, J. P. Ferraris, *J. Power Sources* **1994**, *47*, 89.

[85] K. Zhang, L. L. Zhang, X. S. Zhao, J. Wu, *Chem. Mater*. **2010**, *22*, 1392.

[86] M. Mastragostino, C. Arbizzani, F. Soavi, *Solid State Ionics* **2002**, *148*, 493.

[87] T. Sato G. Masuda, K. Takagi, *Electrochim. Acta* **2004**, *49*, 3603.

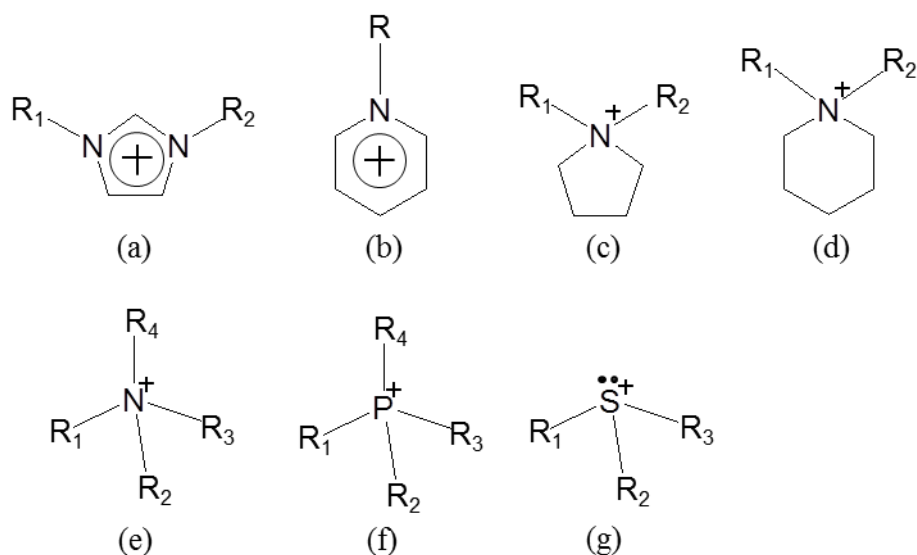[88] S. Shiraishi, T. Miyauchi, R. Sasaki, N. Nishina, A. Oya, R. Hagiwara, *Electrochemistry* **2007**, *75*, 619.

Figure 1–1. Structures of various cations for ILs; (a) dialkylimidazolium, (b) alkylpyridinium, (c) *N,N*-dialkylpyrrolidinium, (d) *N,N*-dialkylpipelidinium, (e) tetraalkylammonium, (f) tetraalkylphosphonium, and (g) trialkylsulfonium.
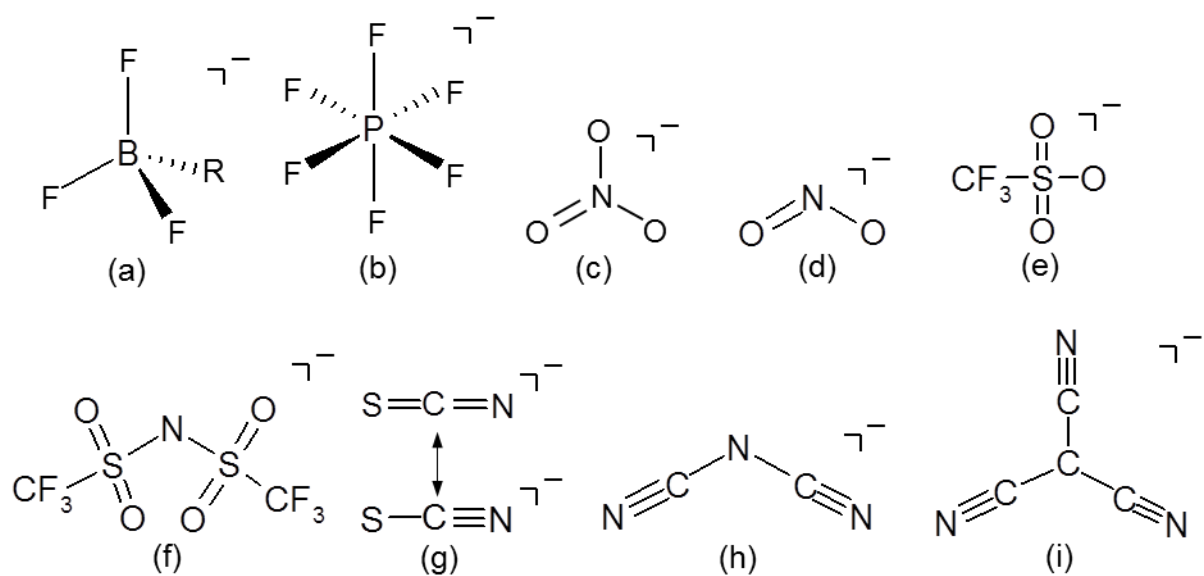

Figure 1–2. Structures of various anions for ILs; (a) perfluoroalkyltrifluoroborate, (b) hexafluorophosphate, (c) nitrate, (d) nitrite, (e) triflate, (f) bis(trifluoromethylsulfonyl)amide (g) thiocyanate, (h) dicyanamide, and (i) tricyanomethanide.
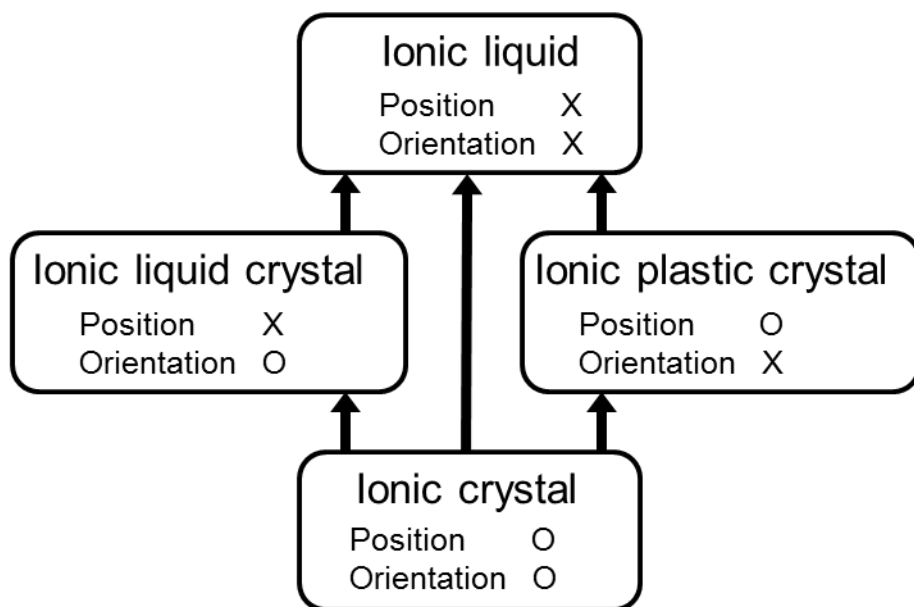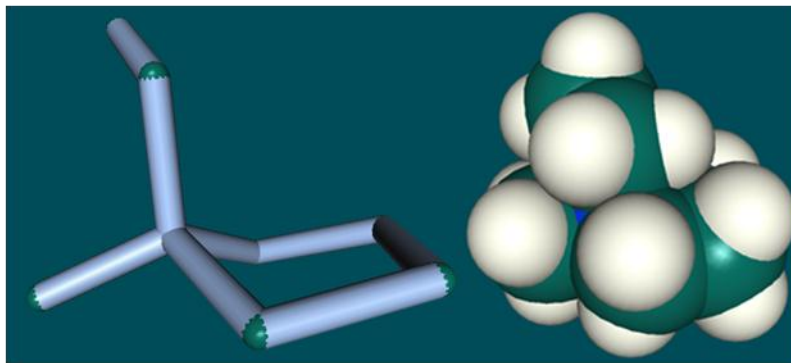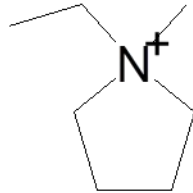
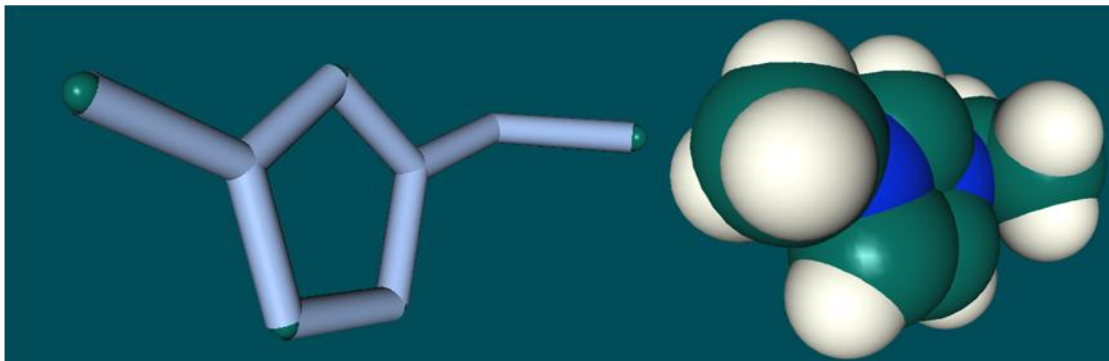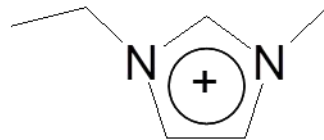Figure 1–3. Relationships of mesophases between IL and ionic crystal.

EMPyr⁺

EMIm⁺

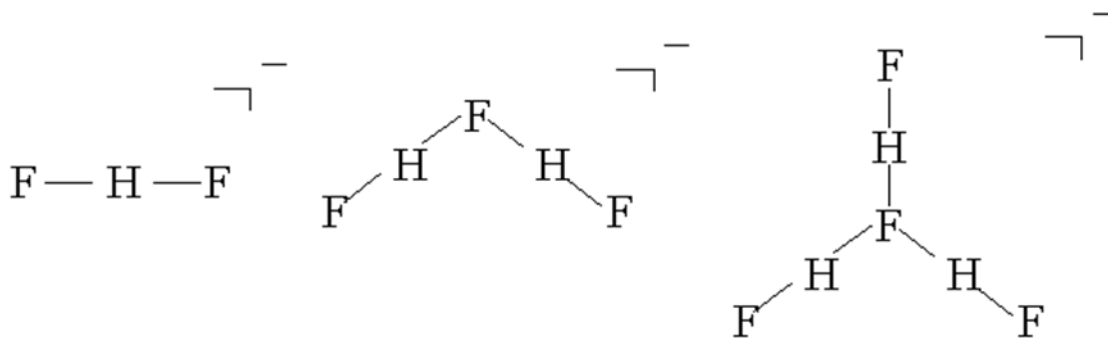Figure 1–4. Space-filling models of EMPyr⁺ and EMIm⁺.

Figure 1–5. Structures of some fluorohydrogenate anions.
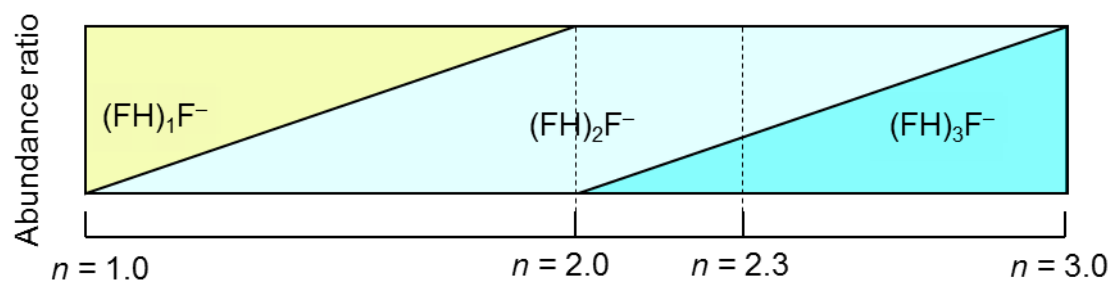

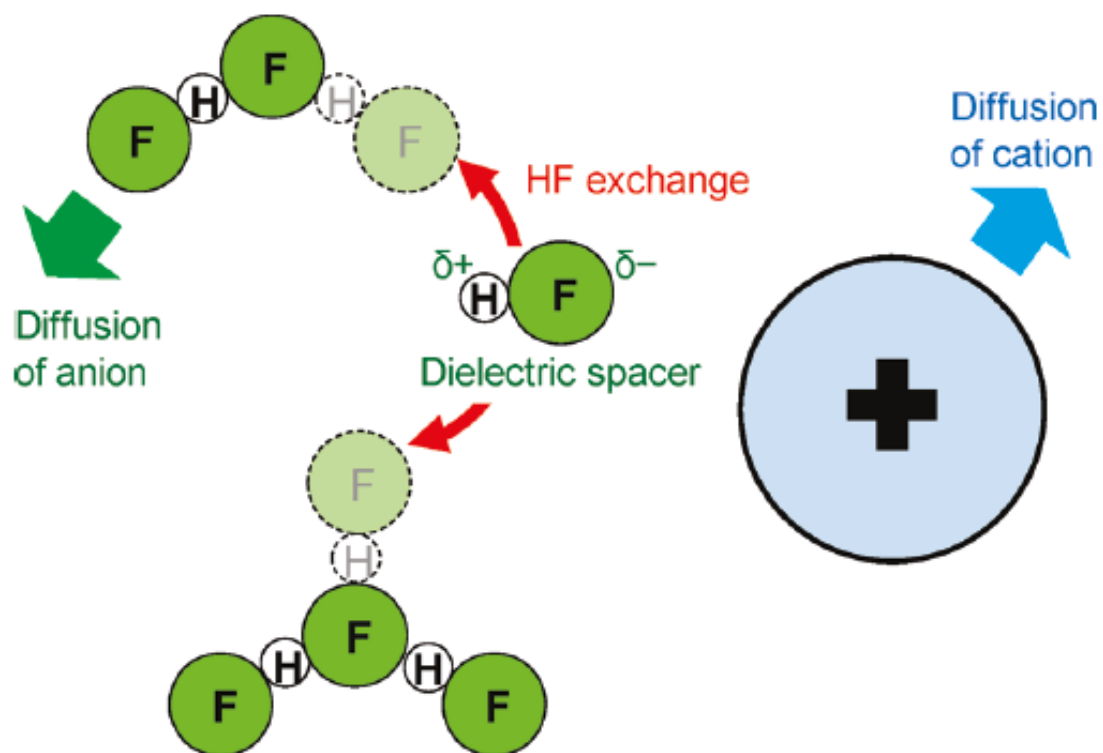Figure 1–6. Abundance ratio of fluorohydrogenate anions in ILs.

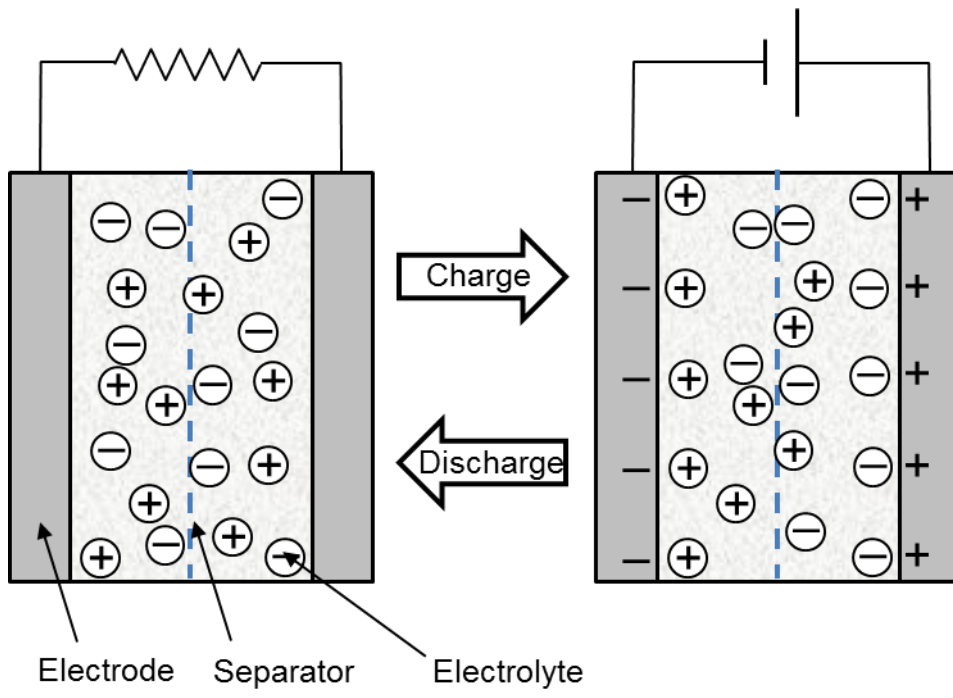Figure 1–7. Model for the ion conduction mechanism of fluorohydrogenate ILs [64].

Figure 1–8. The charge–discharge process of double layer capacitors.

Chapter 2

Experimental

2.1 Apparatus

Moisture sensitive materials were handled in a glove box (Miwa Manufacturing Co., Ltd., MDB-2BL-T1000+ MS-H60W-O) with a gas-refining instrument filled with dried and deoxygenated argon gas (Kyoto Teisan K.K., purity 99.995%). The humidity was always monitored during the experiment. An electric balance (Shimadzu Co., Ltd.) was equipped in the glove box to weigh reagents and samples.

A vacuum line was constructed to handle corrosive gases such as hydrogen fluoride. Figure 2–1 shows a schematic illustration of the vacuum line. The main line was made of corrosion-resistant stainless steel pipes (SUS-316, 1/2 inch o.d.) connected by the stainless unions and valves (SUS-316) with Kel-F (chlorotrifluoroethylene-vinylidene fluoride copolymer, Swagelok Co.) tips. Metal or PFA (tetrafluoroehylene-perfluoroalkylvinylether copolymer) tube (1/4 inch o.d.) were used as the connecting parts to a reaction tube. The line was connected to a rotary vacuum pump through a soda lime chemical trap and a glass cold trap in series. Another direct pumping pass was occasionally used to obtain a high vacuum. The highest vacuum achieved in this system was below 1 Pa. The pressure was monitored by Bourdon and Pirani gauges.

Hydrogen fluoride or fluorohydrogenate salts were mainly handled in PFA reactors (Figure 2–2). The PFA reactors were composed of heat-sealed PFA tubes connected to a stainless steel valve (Swagelok) with Kel-F tips and used as reaction vessels and anhydrous hydrogen fluoride (aHF) storage vessels. The reactor was disconnected from the vacuum line and transferred into the glove box after the reaction. Contact of fluorides with reducing

materials should be carefully avoided. Handling of aHF was carefully performed using appropriate protective gear with immediate access to proper treatment procedures in case of accidental contact with liquid HF, HF vapor, or HF-containing compounds [1,2].

2.2 Syntheses

2.2.1 Reagents

Anhydrous hydrogen fluoride, aHF (Daikin industries Co., Ltd., purity > 99%), was dried over dipotassium hexafluoronickelate, K_2NiF_6 (Ozark-Mahoning Elf Atochem North America, Inc.) prior to use in the PFA container. Anhydrous hydrogen fluoride was transferred from the container to a reactor by distillation. The reactions of aHF with chlorides, bromides, and iodides produce HCl, HBr, and HI as a byproduct. Since hydrogen halide gases have a danger to raise the pressure of the PFA reactor, the pressure inside must be monitored and the PFA reactor was vacuumed until the reaction ceases.

The starting materials for nucleophiles and electrophiles in syntheses of halide salts were used as purchased; N-methylpyrrolidine (Aldrich, 97%), chloromethane (Sumitomo Seika Chemicals, >99%), EMPyrCl (Yoyu Lab.), pyrrolidine (Aldrich, 99%), piperidine (Aldrich, 99.5%), morpholine (Wako Pure Chemical Industries, Ltd., 98%), N-ethylpyrrolidine (Tokyo Chemical Industry Co., Ltd., >97%), 1,4-dibromobutane (Aldrich, 99%), 1,5-dibromopentane (Aldrich, 97%), bis(2-bromoethy)ether (Aldrich, 90%), bromoethane (Aldrich, 99%), trimethylsulfonium bromide (Tokyo Chemical Industry Co., Ltd., >98%), dimetylsulfide (Wako Pure Chemical Industries, Ltd., 98%), diethylsulfide (Aldrich, 98%), iodomethane (Tokyo Chemical Industry Co., Ltd., 99.5%), iodoethane (Aldrich, 99%), 1-methylimidazole (Aldrich, 99%), 3,3,3-trifluoropropyl iodide (Wako Pure Chemical Industries, Ltd., 97%), 3,3,4,4,4-pentafluorobutyl iodide (Fluka, >99%), 3,3,4,4,5,5,6,6,6-nonafluorohexyl iodide (Tokyo Chemical Industry Co., Ltd., 99.5%), 3,3,4,4,5,5,6,6,7,7,8,8,8-tridecafluorooctyl

iodide (Aldrich, 96%), and 3,3,4,4,5,5,6,6,7,7,8,8,9,9,10,10,10-heptadecafluorodecyl iodide (Aldrich, 96%).

The materials used during processes of reaction and purification were purchased, acetonitrile (Wako Pure Chemical Industries, Ltd., water content < 50 ppm), ethanol (Wako Pure Chemical Industries, Ltd., water content < 50 ppm), acetone (Wako Pure Chemical Industries, Ltd., 99.5%), ethyl acetate (Wako Pure Chemical Industries, Ltd., water content < 50 ppm), diethyl ether (Wako Pure Chemical Industries, Ltd., 99.5%), potassium carbonate (Wako Pure Chemical Industries, Ltd., 99.5%), and activated alumina (Wako Pure Chemical Industries, Ltd., about 75 μm).

2.2.2 Halide and fluorohydrogenate salts

Halide salts were synthesized by the reaction of alkyl halides and tertiary amine, etc., in organic solvents, as summarized in Table 2–1. Purifications of the salts were conducted by washing, recrystallization, filtration, and drying. The detail procedures are described in each chapter.

Fluorohydrogenate salts were prepared by the reaction of aHF and halide salts as previously described [3–5]. A large excess of aHF was distilled onto halide salts in a PFA reactor at 77 K, followed by elimination of the unreacted HF and byproduct hydrogen halide at 298 K. Addition and elimination of aHF were repeated several times for effective elimination of halides.

2.3 Measurements of physicochemical and structural properties

2.3.1 Infrared spectroscopy

Infrared spectra were obtained by an FT-IR spectrometer, FTS-155 (Bio-Rad Laboratories, Inc.) at room temperature. The samples were sandwiched between a pair of AgCl windows fixed in a stainless airtight cell under a dry argon atmosphere. The solid sample, DMImCl, sandwiched in the cell was heated over its melting point in the thermostatic chamber and cooled to the room temperature before the measurement. The AgCl windows were washed by ethanol and stored without exposing to light.

2.3.2 Water content measurement

Residual water contents in samples were measured by Karl Fischer moisture titrator, MKC-510N (Kyoto Electronics Manufacturing Co., Ltd.). The titrator was calibrated by a standard solution (containing 1000 ppm water).

2.3.3 Titration of aqueous NaOH for confirmation of HF content

The HF content of the obtained salts was confirmed by titration using aqueous 0.1029 M NaOH (Aldrich). An endpoint of the titration was determined by adding 0.04 w/v% bromothymol blue solution (Wako Pure Chemical Industries).

2.3.4 Differential thermogravimetry

Thermal decomposition temperature was measured by differential thermogravimetric analyzer, DTG-60H (Shimadzu). Nickel cells (< 573 K) and platinum cells (> 573 K) were used for the samples containing HF. Cells were washed with acetone just before the measurements and dried in the apparatus at 473 K for ten minutes. The measurement was performed under the dry argon gas flow of 50 mL min^{-1}. The scan rate in the measurements

was 10 K min^{-1} unless otherwise noted in particular. As the samples with the low HF content (e.g., EMPyr(FH)$_{1.0}$F and DMPyr(FH)$_{1.0}$F) did not release HF before decomposition, the scan rate for the measurements was 1 K min^{-1} after holding the samples for 1 hour at 373 K to remove water as much as possible prior to the scanning the temperature.

2.3.5 Differential scanning calorimetry

Thermal analyses for determination of the melting point, glass transition, and solid–solid phase transition temperature were performed by a differential scanning calorimeter, DSC-60 (Shimadzu). The cells were washed with acetone and carefully dried before the measurements. As the samples were hygroscopic, they were packed and sealed in a pressure-resistant cell made of stainless steel using a pressing machine at about 25 MPa under the dry argon atmosphere. For the samples having phase transitions at low temperatures, cryogenic measurement using liquid nitrogen was conducted. A liquid nitrogen bath was cooled enough to be stable and a sample room was kept at the staring temperature for more than ten minutes to avoid artifactual noises. The scan rate in the measurements was 5 K min^{-1} unless otherwise noted in particular. Dry argon gas was always flowed in the sample room (50 mL min^{-1}) during the measurement.

2.3.6 Viscosity measurement

Viscosity was measured by a cone and plate rheometer, LVDV-II+PRO (Brookfield Engineering Laboratories, Inc.). The spindle of CPE-40 was used in the present study. The samples were transferred in the apparatus under a dry argon atmosphere in a glove bag.

2.3.7 Density measurement

Density was measured by weighing the samples in a hand-made PFA vessel of which the volume was calibrated by distilled water and ethanol. The measurements were performed

under a dry argon atmosphere at room temperature.

2.3.8 Self-diffusion coefficient measurement

Diffusion coefficients were measured via pulsed-field gradient spin-echo nuclear magnetic resonance (PGSE-NMR) using a JEOL JEM-ECX400 spectrometer. The attenuation as a result of free diffusion in the Stejskal–Tanner sequence using half-sine-shaped gradient pulses was given by

$$E = S/S_0 = \exp(-\gamma^2 g^2 \delta^2 D(4\Delta - \delta)/\pi^2) \qquad 2\text{--}1$$

where γ is the gyromagnetic ratio, S is the amplitude of the echo signal and S_0 is the amplitude at which $g = 0$, g is the amplitude of the gradient pulse, δ is the duration of the gradient pulse, and Δ is the interval between the gradient pulses. Thus, D could be determined from the slope of the plot of ln$E$ against varying g. In the present experiments, the maximum g value was 13.5 T/m, Δ was set to 10 ms, and the δ values varied in the range 0.1 to 1 ms.

2.3.9 X-ray diffraction analysis

The samples were transferred into a quartz capillary under a dry argon atmosphere. The capillary was flame-sealed using an oxygen burner and was centered on an X-ray diffractometer (R-axis Rapid II, Rigaku) equipped with an imaging plate area detector (using the program RAPID XRD 2.3.3 [6]) and graphite-monochromated MoKα radiation (0.71073 Å). The φ angle was rotated at a rate of $1° \text{ s}^{-1}$ and the ω and χ angles were fixed at 20° and 0°, respectively, during the data collection (1440 s). The sample temperature was controlled by using a nitrogen flow.

2.3.10 Conductivity measurement

Ionic conductivity was measured by an AC impedance technique using a calibrated cell

with a pair of platinum disk electrodes (Figure 2–3) with the aid of PARSTAT 2273 (Princeton Applied Research) or VSP (Bio-Logic) electrochemical measurement system. The temperature was controlled by an ethanol bath monitored by an alcohol thermometer or thermostatic air chamber. The cell was entirely filled with the liquefied sample at a temperature above its melting point prior to the measurement. The ionic conductivity data were measured after the sample was held at the target temperature for at least 1 hr. The steadiness of the ionic conductivity value was confirmed by plotting it against time during this period.

2.3.11 Linear sweep voltammetry

Electrochemical stabilities of the samples were investigated by linear sweep voltammetry (LSV) under a dry argon atmosphere with the aid of HZ-3000 (Hokuto Denko Corp.) or VSP. The electrochemical cell used for LSV is described in Figure 2–4. Vitreous carbon electrodes (Tokai Carbon Co., Ltd.) with a surface area of 0.0700 cm^2 and 0.200 cm^2 were used for the working and counter electrodes, respectively. They were polished with a sandpaper (#600– #2000) and α-alumina (Wako Pure Chemical Industries, Ltd., particle diameter of 0.5 μm) and washed with acetone and then dried under vacuum at 453 K prior to use. They were coated with PFA shrinkable tubes. A silver wire (Japan Metal Service, $\phi 1.0$ mm, purity 99.99%) immersed in $EMImBF_4$ containing 0.05 M $AgBF_4$ was used for the reference electrode and was partitioned in the electrolyte with a porous polytetrafluoroethylene (PTFE) membrane (Porex Corp., $45 - 60$ μm of pore diameter). A platinum plate (Nilaco Corp., 0.1 mm thickness) with a surface area of 0.15 cm^2 was also used for the working electrode. The platinum electrode was washed with acetone and carefully dried prior to use. The scan rate of 10 mV s^{-1} was selected and the obtained potentials were referenced to the redox potential of ferrocenium/ferrocene (Fc^+/Fc) couple dissolved in the electrolyte.

2.4 Characterization of electrochemical capacitors

2.4.1 Fabrication of the cell

The electrolyte, $EMPyr(FH)_{2.3}F$, was synthesized by the reaction of EMPyrCl (Yoyu Lab.) and anhydrous HF (Daikin Industries, Co. Ltd., > 99%) as described above. Activated carbon sheet electrodes with 0.5 mm thickness, composed of 85 wt% of activated carbon from phenol resin (surface area: 2000 m^2 g^{-1}, mean pore diameter: 2.14 nm, and total pore volume: 1.10 cm^3 g^{-1}), 10 wt% of PTFE, and 5 wt% of carbon black, were dried under vacuum at 453 K overnight. A three-electrode test cell (Figure 2–5) was assembled with a pair of activated carbon sheet electrodes, vitreous carbon current collectors, PTFE separators, and a Ag foil quasi-reference electrode. The Ag foil was inserted between two activated carbon sheet electrodes as a quasi-reference to separately monitor the potentials of the positive and negative electrodes during the charge–discharge test. Before starting electrochemical measurements, the potentials of the electrodes were monitored overnight to confirm their steadiness. The potentials were referenced to the ferrocenium (Fc^+) / ferrocene (Fc) redox couple.

2.4.2 Electrochemical measurements and analysis of the electrodes

Electrochemical measurements were performed under an Ar atmosphere with the aid of a VSP electrochemical measurement system (Bio-Logic). Capacitance of each electrode was calculated by the equation of $C = It/wV$ from the discharge curve where I, t, w, and V denote the current value, discharging time, mass of the electrode, and charging voltage. The detail conditions of electrochemical measurements are described in Chapters 8 and 9.

Analyses of electrodes were performed by X-ray photoelectron spectroscopy (JPC-9010 MC (JEOL)) with Mg Kα radiation as a photoelectron source. The electrodes were washed by acetone under argon atmosphere, followed by drying under vacuum. The residual electrolyte

was not detected because the N1s peak ascribed to the nitrogen in EMPyr$^+$ was not observed for any electrodes. The surfaces of the samples were etched by Ar ion bombardment for 10 s before analysis.

References

[1]   K. Matsumoto, R. Hagiwara, *J. Fluorine Chem.* **2010**, *131*, 805.

[2]   D. Peters, R. Miethchen, *J. Fluorine Chem.* **1996**, *79*, 161.

[3]   R. Hagiwara, T. Hirashige, T. Tsuda, Y. Ito, *J. Fluorine Chem.* **1999**, *99*, 1.

[4]   R. Hagiwara, T. Hirashige, T. Tsuda, Y. Ito, *J. Electrochem. Soc.* **2002**, *149*, D1.

[5]   K. Matsumoto, R. Hagiwara, Y. Ito, *Electrochem. Solid-State Lett.* **2004**, *7*, E41.

[6]   RAPID XRD, version 2.3.3; Rigaku coorporation: Tokyo, Japan, 1999.

Table 2–1 The present halide salts synthesized by reactions of nucleophiles and electrophiles.

| Halide salt	Nucleophile	Electrophile
DMPyrCl: N,N-Dimethylpyrrolidinium chloride	N-methylpyrrolidine	Chloromethane
DEPyrBr: N,N-Diethylpyrrolidinium bromide	N-ethylpyrrolidine	Bromoethane
AS[4.4]Br: 5-Azoniaspiro[4.4]nonane bromide	Pyrrolidine	1,4-Dibromobutane
AS[4.5]Br: 5-Azoniaspiro[4.5]decane bromide	Pyrrolidine	1,5-Dibromopentane
AS[5.5]Br: 6-Azoniaspiro[5.5]undecane bromide	Piperidine	1,5-Dibromopentane
AS[4.2O2]Br: 8-Oxa-5-azoniaspiro[4.5]decane bromide	Morpholine	1,4-Dibromobutane
AS[5.2O2]Br: 9-Oxa-6-azoniaspiro[5.5]undecane bromde	Morpholine	1,5-Dibromopentane
AS[2O2.2O2]Br: 3,9-Dioxa-6-azoniaspiro[5.5]undecane bromide	Morpholine	Bis(2-bromoethy)ether
$S_{112}I$: Dimethylethylsulfonium iodide	Dimethylsulfide	Iodoethane
$S_{122}I$: Diethylmethylsulfonium iodide	Diethylsulfide	Iodomethane
$S_{222}I$: Triethylsulfonium iodide	Diethylsulfide	Iodoethane
$C_{3F3}MImI$: 1-Methyl-3-(3,3,3-trifluoropropyl)imidazolium iodide	1-Methylimidazole	3,3,3-Trifluoropropyl iodide
$C_{4F5}MImI$: 1-Methyl-3-(3,3,4,4,4-pentafluorobutyl)imidazolium iodide	1-Methylimidazole	3,3,4,4,4-Pentafluorobutyl iodide
$C_{6F9}MImI$: 1-Methyl-3-(3,3,4,4,5,5,6,6,6-nonafluorohexyl)imidazolium iodide	1-Methylimidazole	3,3,4,4,5,5,6,6,6-Nonafluorohexyl iodide
$C_{8F13}MImI$: 1-Methyl-3-(3,3,4,4,5,5,6,6,7,7,8,8,8-tridecafluorooctyl)imidazolium iodide	1-Methylimidazole	3,3,4,4,5,5,6,6,7,7,8,8,8-Tridecafluorooctyl iodide
$C_{10F17}MImI$: 1-Methyl-3-(3,3,4,4,5,5,6,6,7,7,8,8,9,9,10,10,10-heptadecafluorodecyl)imidazolium iodide	1-Methylimidazole	3,3,4,4,5,5,6,6,7,7,8,8,9,9,10,10,10-Heptadecafluorodecyl iodide
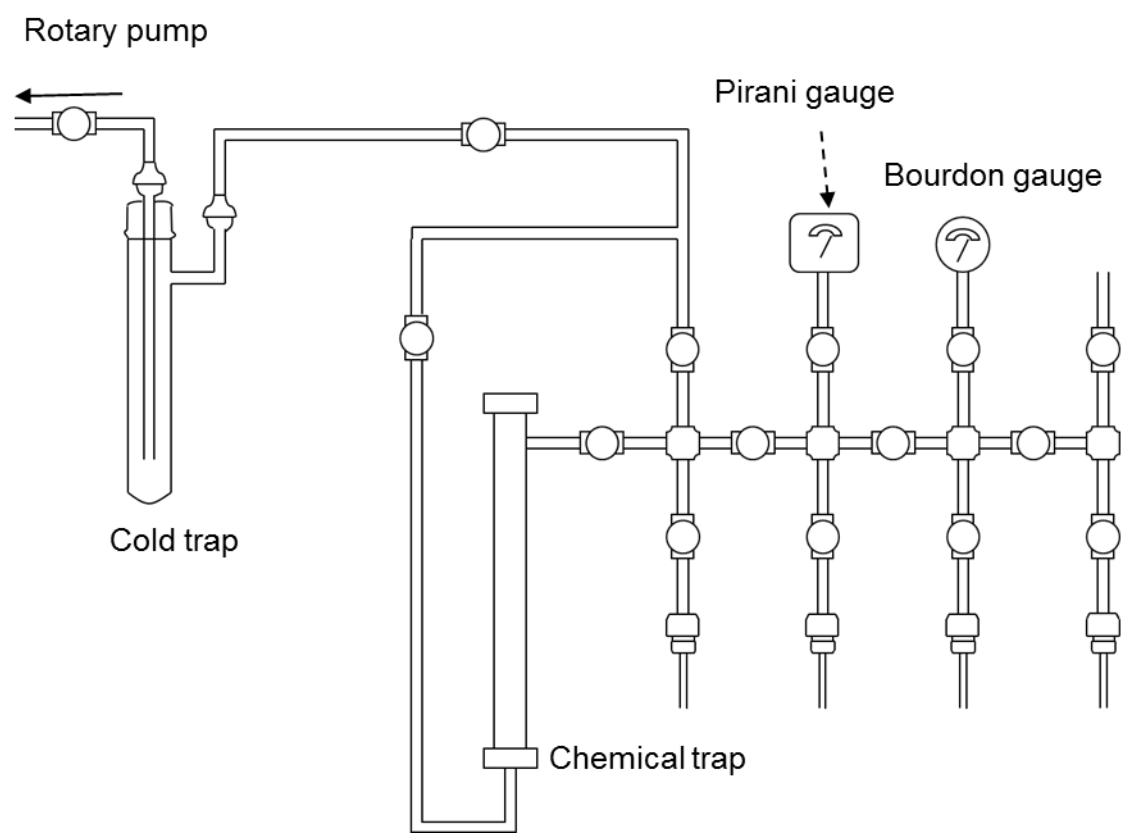
Figure 2–1. A schematic drawing of a vacuum line.
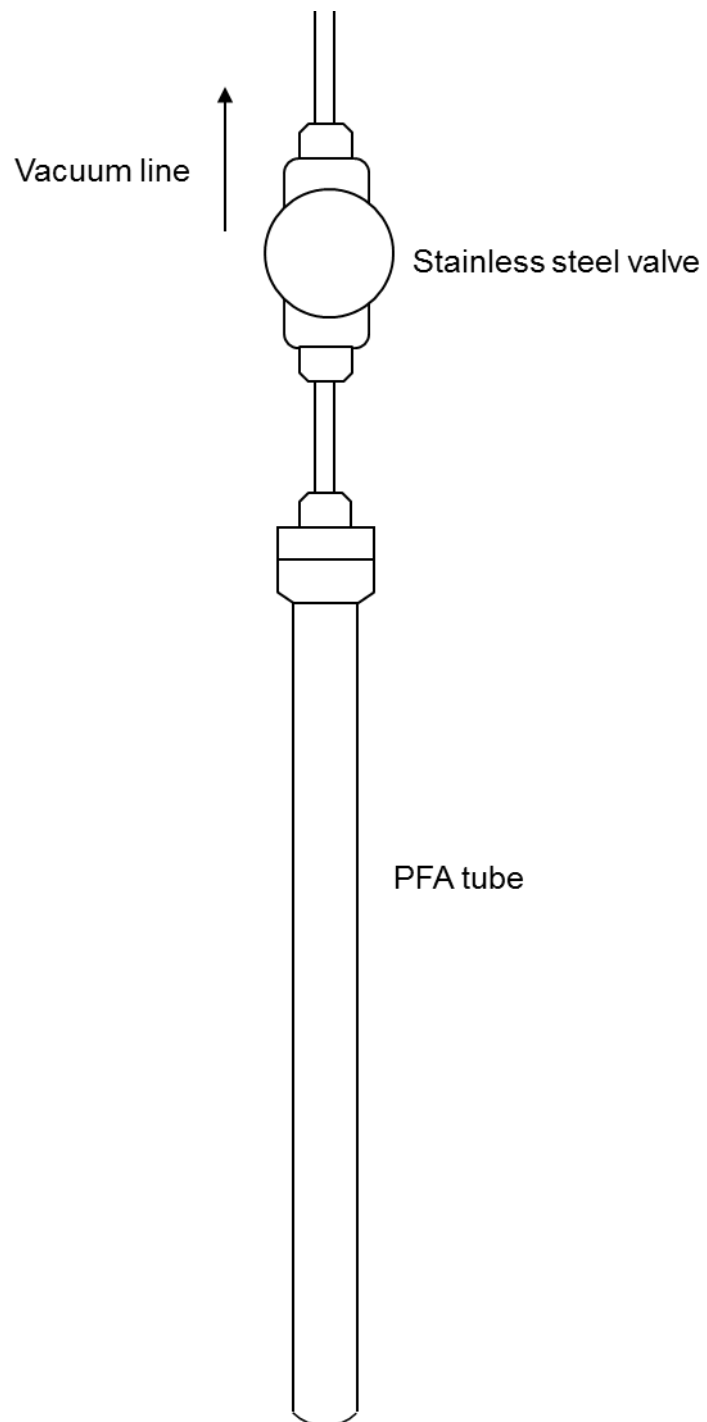
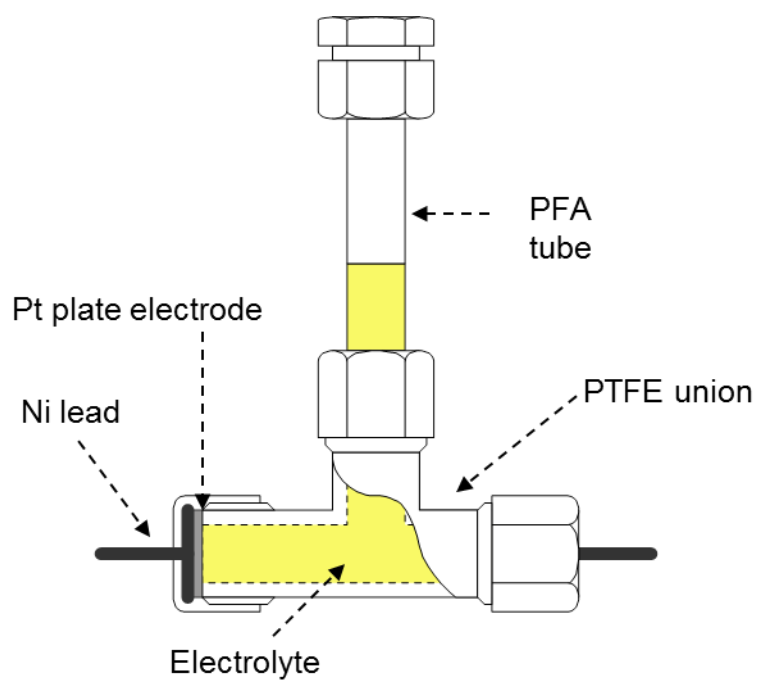Figure 2–2. A schematic drawing of a PFA reactor.

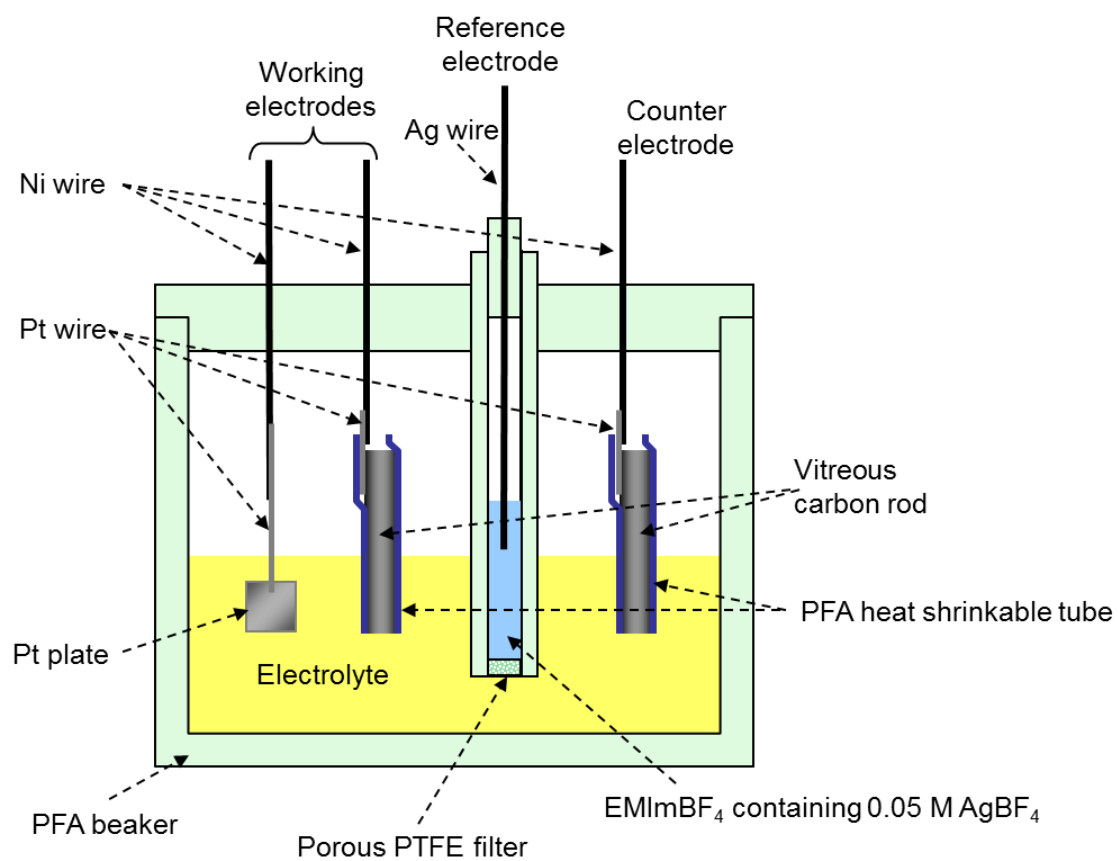Figure 2–3. A schematic drawing of a conductivity measurement cell.

Figure 2–4. Electrolytic cell for three-electrode LSV measurements.
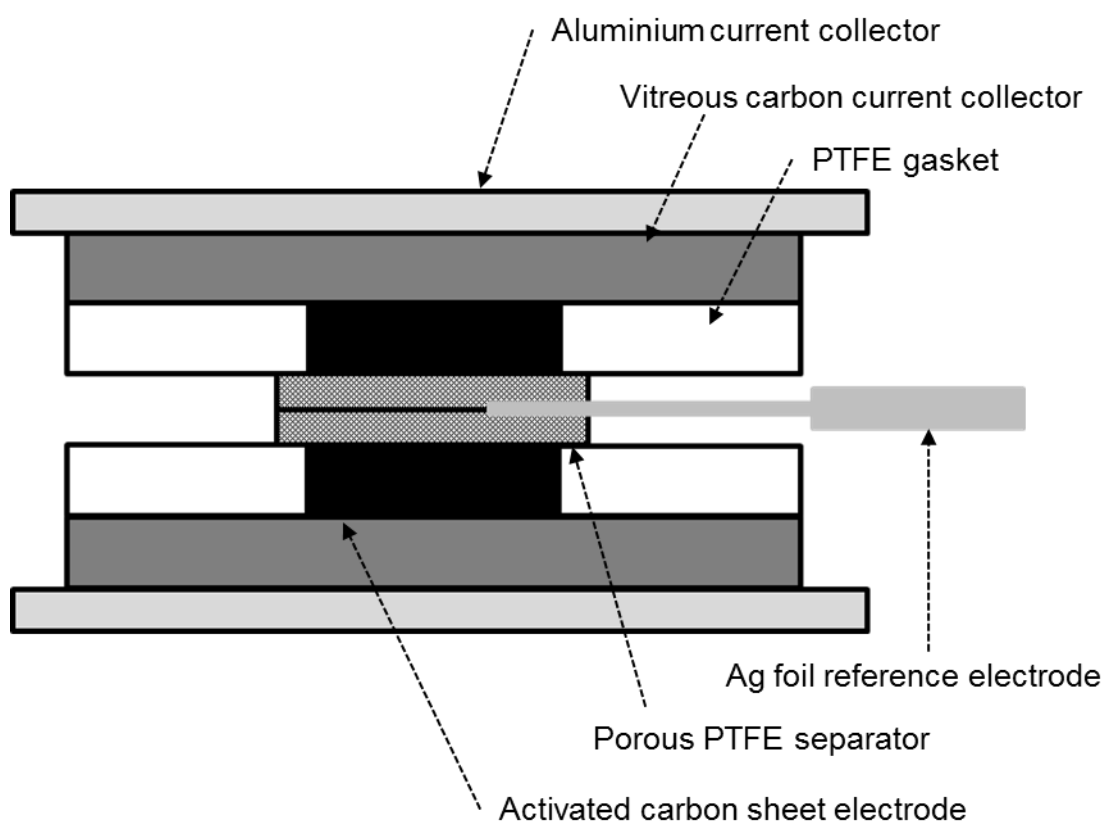
Figure 2–5. A schematic drawing of a three electrode test cell.

Chapter 3

Dialkylpyrrolidinium salts of (FH)₂F⁻ anion

Dialkylpyrrolidinium salts of $(FH)_2F^-$ anion

3.1 Introduction

The study of IPCs has been increasingly extended, with progress in the chemistry of ILs. While organic salts based on pyrrolidinium and tetraalkylammonium cations often form low-melting ILs, those with short alkyl chains sometimes exhibit an IPC phase around room temperature [1,2]. The organic IPCs entirely consist of ions and, thus, have some benefits, such as nonflammability and low vapor pressures, which improve the safety and reliability of electrochemical devices. Although solid-state ionic conductivities of 10^{-3} to 10^0 mS cm^{-1} at room temperature have been achieved for some IPCs with additives, further improvements in ionic conductivity would lead to a lower internal resistance in practical applications [1,3,4]. The previous results about fluorohydrogenate ILs motivated to incorporate fluorohydrogenate anions into IPCs for application as solid-state electrolytes with high ionic conductivities [5]. The combination of the tetraethylphosphonium cation and fluorohydrogenate anion exhibited an IPC phase with an inverse nickel–arsenide-type structure and an ionic conductivity of 5 mS cm^{-1} at 323 K [5]. In the present study, the physicochemical, structural, and electrochemical properties of new IPCs composed of $(FH)_2F^-$ and *N,N*-dimethylpyrrolidinium (DMPyr$^+$) or *N*-ethyl-*N*-methylpyrrolidinium cations (EMPyr$^+$) (see Figure 3–1 for structures) are reported.

3.2 Experimental

The salt, DMPyrCl, was synthesized by the reaction of *N*-methylpyrrolidine and chloromethane as described in the previous work [6]. Acetonitrile and *N*-methylpyrrolidine were mixed in a high-pressure glass container (Ace Glass) under argon atmosphere in a glove

bag. Chloromethane was condensed on the mixture at liquid nitrogen temperature through the vacuum line. The reaction proceeded on warming up to room temperature. The reaction is exothermic and should be carefully performed. The mixture was stirred at 298 K under an airtight condition for one day. The obtained salt was washed by ethyl acetate three times. After removing ethyl acetate by decantation, filtration, and evacuation, DMPyrCl was recrystallized twice from the ethanol solution by adding ethyl acetate. The purified DMPyrCl was dried under vacuum at 393 K for 48 hours. The purchased EMPyrCl was purified by recrystallization from acetonitrile solution by adding ethyl acetate. After recrystallization and washing, the salt was dried under vacuum at 393 K for 48 h.

A large excess of aHF was distilled onto DMPyrCl in a PFA reactor at 77 K, followed by elimination of unreacted HF and byproduct HCl at 298 K. Addition and elimination of aHF were repeated several times for effective elimination of chloride in the form of HCl. Final evacuation at 298 K below 1 Pa for several days gave $DMPyr(FH)_2F$. Testing for the presence of residual Cl^- with aqueous $AgNO_3$ solution gave no silver halide precipitation. The HF composition of 2.0 was confirmed by titration using aqueous NaOH solution. IR (AgCl): $v =$ 2323 (m), 1989 (m), 1811 (s), 1044 (w) cm^{-1} [$(FH)_2F^-$, in Figure 3–2]. See references 7 and 8 for the assignments of the IR bands.

The fluorohydrogenate salt, $EMPyr(FH)_2F$, was prepared by mixing $EMPyr(FH)_{2.3}F$ and $EMPyr(FH)_{1.8}F$ in a molar ratio of 2 to 3. The salt $EMPyr(FH)_{2.3}F$ was prepared as the same manner in $DMPyr(FH)_2F$. Removal of HF from $EMPyr(FH)_{2.3}F$ at 353 K in a PFA reactor gave $EMPyr(FH)_{1.8}F$. The HF composition of 2.0 was confirmed by titration using aqueous NaOH solution. Testing for the presence of residual Cl^- with aqueous $AgNO_3$ solution gave no silver halide precipitation. IR (AgCl): $v =$ 2326 (m), 1992 (m), 1810 (s), 1034 (w) cm^{-1} [$(FH)_2F^-$ in Figure 3–2]. See references 7 and 8 for the assignments of the IR bands.

39

3.3 Results and discussion

3.3.1 Thermal behavior

Figure 3–3 shows the TG curves of DMPyr(FH)$_2$F and EMPyr(FH)$_2$F. The weight losses above 300 K in the TG curves are caused by the reversible elimination of HF from (FH)$_2$F$^-$. Irreversible decomposition of the cation is observed above 500 K. The high nucleophilicity of fluorohydrogenate anions results in lower decomposition temperatures compared to other dialkylpyrrolidinium salts [9]. Figure 3–4 shows DSC thermograms of DMPyr(FH)$_2$F and EMPyr(FH)$_2$F during the heating process. The DMPyr(FH)$_2$F salt exhibits a solid–solid phase transition (258 K) and melting point (325 K) during the heating process, and a corresponding solid–solid phase transition (227 K) and freezing point (322 K) during the cooling process. The EMPyr(FH)$_2$F salt exhibits a solid–solid phase transition (236 K) and melting point (303 K) during the heating process, whereas the cooling process shows two solid–solid phase transitions (210 and 167 K) and a freezing point (296 K).

In the DSC thermogram of EMPyr(FH)$_2$F, a crystal phase below 167 K and another IPC phase (IPC II) between 167 and 210 K are observed separately during the cooling process (Figure 3–5). Figure 3–6 shows a DSC thermogram of EMPyr(FH)$_2$F when the scanning direction was reversed to the heating process at 200 K. A new phase transition is observed at 240 K, which corresponds to the phase transition observed at 210 K in the cooling process (Figure 3–5 (b)). Considering the small entropy change (5 J K^{-1} mol^{-1}) and X-ray diffraction pattern (Figure 3–7 (d)), the phase between 167 and 210 K (cooling process) may be an IPC phase (IPC II), while detailed analysis of this phase is not a target of this chapter.

The ΔS_{fus} values of DMPyr(FH)$_2$F (4.1 J K^{-1} mol^{-1}) and EMPyr(FH)$_2$F (2.0 J K^{-1} mol^{-1}) are smaller than those of other IPCs [cf. 40 J K^{-1} mol^{-1} for EMPyrTFSA, 7.4 J K^{-1} mol^{-1} for N$_{1223}$CF$_3$BF$_3$] [1,4,5,9–12]. Considering the soft textures of DMPyr(FH)$_2$F and EMPyr(FH)$_2$F, in addition to the small ΔS_{fus} values, the IPCs are formed between the solid–solid and solid–

liquid phase transitions (258 – 325 K for DMPyr(FH)$_2$F and 236 – 303 K for EMPyr(FH)$_2$F in the heating process). Both the salts have a small degree of supercooling in the phase transition from IL to IPC, because this phase transition has a small entropy change and solidification easily occurs. Both the crystal–IPC and IPC–IL phase transition temperatures for DMPyr(FH)$_2$F are 22 K higher than those of EMPyr(FH)$_2$F. The difference is considered to be mainly derived from the different electrostatic interactions.

3.3.2 Structures of ionic plastic crystal

Figure 3–7 shows the XRD patterns of the crystal, IPC (II) and IPC phases. Figures 3–8 (a) and (b) show XRD patterns of the IPC phases of DMPyr(FH)$_2$F and EMPyr(FH)$_2$F. In the XRD patterns of the IPC phases, only three diffraction peaks were observed in the low 2θ-angle region (7.11, 8.24, and 11.66° for DMPyr(FH)$_2$F; 6.98, 8.01, and 11.34° for EMPyr(FH)$_2$F). The XRD peaks of the IPCs can be indexed with the indices (111), (200), and (220), as for a NaCl-type lattice, with lattice constants of 9.90 Å for DMPyr(FH)$_2$F and 10.18 Å for EMPyr(FH)$_2$F (Figure 3–8 (c)). The resulting lattice volume of the IPC phase for DMPyr(FH)$_2$F (970 Å^3) is smaller than that for EMPyr(FH)$_2$F (1055 Å^3) as a result of the smaller size of DMPyr$^+$ than that of EMPyr$^+$. The formation of a cubic lattice for the 1:1 IPC phase suggests that the ionic species (Figure 3–1) are rotating freely to form a large globular shape. This rapid rotating motion increases the thermal factors of the atoms in the lattice and prevents diffraction in the high 2θ-angle region. The increase in rotational degrees of freedom by the crystal–IPC phase transition results in more highly symmetric structures in the IPC phase. Similar behavior was observed for 1-ethyl-2-methylpyrrolinium TFSA and trimethylammonium trifluoroacetate by XRD, the IPC phase of the latter being indexed as a CsCl-type cubic structure [13,14]. The differences in the structures of the IPC phases found for the present pyrrolidinium fluorohydrogenate salts (NaCl-type structure with a coordination number of six) and trimethylammonium trifluoroacetate (CsCl-type structure with a

41

coordination number of eight) arise from the ratio of the cation size to the anion size; the trimethylammonium cation and trifluoroacetate anion have similar sizes, but $(FH)_2F^-$ is apparently smaller than $DMPyr^+$ or $EMPyr^+$, occupying the octahedral sites of the cubic-close-packed cations. It is noteworthy that the large tetraethylphosphonium cation forms an IPC phase with the hexagonal unit cell of the inverse nickel–arsenide-type structure when combined with $(FH)_2F^-$ [5].

3.3.3 Ionic conductivity

Figure 3–9 shows Arrhenius plots of ionic conductivity for $DMPyr(FH)_2F$ and $EMPyr(FH)_2F$ (see Table 3–1 for ionic conductivity values). The discontinuous changes in ionic conductivity at the crystal–IPC and IPC–IL phase transitions agree with those observed by DSC. The ionic conductivities of the IPC phases range from 10^0 to 10^1 mS cm^{-1} (e.g., 10.3 mS cm^{-1} at 298 K for $DMPyr(FH)_2F$ and 14.4 mS cm^{-1} at 288 K for $EMPyr(FH)_2F$). These values for $DMPyr(FH)_2F$ and $EMPyr(FH)_2F$ are higher than those for known IPCs in the neat form (e.g., 0.20×10^{-5} mS cm^{-1} at 298 K for DMPyrTFSA, 1.45×10^{-5} mS cm^{-1} at 298 K for EMPyrTFSA, 1.3×10^{-3} mS cm^{-1} at 313 K for *N,N′*-ringed pyrazolium TFSA, 1.9×10^{-3} mS cm^{-1} at 298 K for neat $N_{1223}CF_3BF_3$) and in the salt-doped form (e.g., 2×10^{-1} mS cm^{-1} at 333 K for 5 mol% LiTFSA-doped EMPyrTFSA, 1.0×10^{-1} mS cm^{-1} at 313 K for 5 mol% LiTFSA-doped pyrazolium TFSA, and 3.7×10^{-1} mS cm^{-1} at 298 K for 5 mol% $LiCF_3BF_3$-doped $N_{1223}CF_3BF_3$) [1,15,16]. The activation energies obtained from the Arrhenius plots (4.4 and 7.6 kJ mol^{-1} for the IL and IPC phases for $DMPyr(FH)_2F$; 4.9 and 8.6 kJ mol^{-1} for the IL and IPC phases for $EMPyr(FH)_2F$) indicate that diffusion of the ions in the IPC phase has a larger energetic barrier than that in the IL phase. In the IL phase, $DMPyr(FH)_2F$ exhibits higher ionic conductivities (e.g., 138 mS cm^{-1} at 333 K) than those of $EMPyr(FH)_2F$ (e.g., 128 mS cm^{-1} at 333 K) because the smaller size of the cations results in a larger number of ions per volume, as in the cases of $DMIm(FH)_{2.3}F$ and $EMIm(FH)_{2.3}F$.[24] In the IPC phase,

DMPyr(FH)$_2$F exhibits lower ionic conductivities (e.g., 8.06 mS cm^{-1} at 288 K) than those of EMPyr(FH)$_2$F (e.g., 14.4 mS cm^{-1} at 288 K).

3.3.4 Diffusion behavior

Figure 3–10 shows Arrhenius plots of self-diffusion coefficients for (a) DMPyr(FH)$_2$F and (b) EMPyr(FH)$_2$F obtained by PGSE-NMR (Table 3–2 for the self-diffusion coefficient values). The self-diffusion coefficients for the cation and anion of DMPyr(FH)$_2$F in the IL phase are 1.83×10^{-6} and 4.81×10^{-6} cm^2 s^{-1}, respectively, at 338 K. The self-diffusion coefficient for the anion of DMPyr(FH)$_2$F in the IPC phase is 3.44×10^{-7} cm^2 s^{-1} at 298 K, whereas that for the cation was too small to be measured. These results suggest that the major conductive species in the IPC phase of DMPyr(FH)$_2$F is the anion. The difference between the self-diffusion coefficients of the IL and IPC phases is one order of magnitude that agrees with the difference between the ionic conductivities of these phases. The fact that only the anion is a charge carrier in the IPC phase indicates that the fluorohydrogenate IPC behaves like a superionic material [17–20]. The cation, without diffusion ability, holds the IPC lattice structure and supports the translation of the anion by rotating locally.

On the other hand, the diffusion behavior of the ionic species in the IPC temperature range of EMPyr(FH)$_2$F is different from that of DMPyr(FH)$_2$F; the self-diffusion coefficient of EMPyr$^+$ was measurable even in the IPC phase temperature range. This phenomenon is caused by a small number of mobile cations in the IPC lattice, because the peak intensity of ^{1}H corresponding to EMPyr$^+$ gradually decreases with decreasing temperature (I_{cat}/I_{an} in the IPC phase is less than 10% of that in the IL phase, where I_{cat} and I_{an} at 255 K denote peak intensities of EMPyr$^+$ and (FH)$_2$F$^-$). It is noteworthy that this IL phase is not observed as a non-equilibrated phase, because the result is reproducible with increasing and decreasing temperatures and the time dependence showed the peak intensity reached a steady state.

The different diffusion behaviors of DMPyr(FH)$_2$F and EMPyr(FH)$_2$F may be caused by the difference in the cationic structures. The IPC lattice of EMPyr(FH)$_2$F has a looser packing than that of DMPyr(FH)$_2$F. This is supported by the low enthalpy change of melting and the broad peak for EMPyr(FH)$_2$F in the DSC analysis, because of the lower symmetry of EMPyr(FH)$_2$F than that of DMPyr(FH)$_2$F. As a result, a part of EMPyr$^+$ ions are mobile in the IPC lattice while the other cations are fixed to the framework of the crystal lattice. In other words, in the case of EMPyr(FH)$_2$F, all the cations did not necessarily remain stationary to form the crystal lattice. In the IPC phase temperature range for EMPyr(FH)$_2$F, the self-diffusion coefficient of the cation is higher than that of the anion. Figure 3–10 (c) shows schematic illustration of the diffusion behavior of ions in the IPC temperature range for EMPyr(FH)$_2$F. The self-diffusion coefficient of EMPyr$^+$ ions forming the crystal ($D_{\text{cation(slow)}}$ is not detected in the present NMR measurement because of the low diffusivity, as that for the cations in DMPyr(FH)$_2$F. However, the self-diffusion coefficient of the mobile EMPyr$^+$ ions in the plastic crystal ($D_{\text{cation(fast)}}$) is detectable giving a high self-diffusion coefficient (D_{cation}(measured)) similar to that in the IL phase and $D_{\text{cation(fast)}}$ overlaps D_{cation}(measured) in the IPC temperature range since $D_{\text{cation(slow)}}$ is too small to be detected. The peak intensity of the ^{1}H nuclei corresponding to EMPyr$^+$ in the IPC temperature range decreased as a result of the decrease in the number of mobile EMPyr$^+$ ions. Two kinds of anions are present in the EMPyr(FH)$_2$F IPC phase: those strongly bound to the IPC lattice with a self-diffusion coefficient $D_{\text{anion(slow)}}$ and those not with the self-diffusion coefficient $D_{\text{cation(fast)}}$. The former is dominant in the IPC phase, giving a lower self-diffusion coefficient D_{anion}(measured) as an average value of $D_{\text{anion(slow)}}$ and $D_{\text{anion(fast)}}$.

3.3.5 Ion conduction behavior

It is unlikely that the anion migrates in the NaCl-type lattice in the form of (FH)$_2$F$^-$,

because it is too large to move in the lattice (DMPyrBF$_4$, with a similar anion size, does not show such a high ionic conductivity between 298 and 400 K) [21,22]. As reported previously, the HF unit in $(FH)_nF^-$ exchanges between two anions in the IL state and functions as a dielectric spacer to weaken cation–anion interactions [23]. By analogy with this mechanism in the IL phase, the HF unit in $(FH)_2F^-$ in the IPC phase can act as a dielectric spacer between the cation and anion, and facilitate the diffusion of the anion. Measurement of the diffusion behavior of fluorine nuclei was difficult in our trial because of their long relaxation times. The existence of an isolated proton and the resulting proton hopping are not likely to occur under such basic conditions. Another important function of this HF exchange is the reduction of the effective anionic size [23]. In a very short period, $(FH)_2F^-$ in one site separates into two species, $(FH)_1F^-$ and the HF unit, and $(FH)_1F^-$ migrates in the shape of a rod through a narrow space to a neighboring site in the IPC (Figure 3–11). In the neighboring site, this $(FH)_1F^-$ catches the HF unit given by another $(FH)_2F^-$ to form a new $(FH)_2F^-$. These continuous phenomena (release of HF, migration of $(FH)_1F^-$, and capture of HF) may transfer the charge in the IPC (Figure 3–11), leading to the high ionic conductivity. The [111] direction is the most widely opened diffusion path for the anion, whereas the path directed to [110] is narrow but the shortest to the neighboring anion site.

3.3.6 Electrochemical behavior

A linear sweep voltammogram of a vitreous carbon electrode in the IPC phase of DMPyr(FH)$_2$F at 298 K (Figure 3–12) revealed that the anodic and cathodic currents are observed from +2.0 and −1.9 V (vs. Fc$^+$/Fc), respectively. The electrochemical stability of the DMPyr(FH)$_2$F IPC is similar to those observed for *N*-alkyl-*N*-methylpyrrolidinium fluorohydrogenate ionic liquids [6]. As mentioned in the previous study, the cathodic limit reaction probably includes the reduction of both the cation and anion [24]. The reaction at the anode limit is probably decomposition of the IPC, including fluorination of the cation.

45

References

[1] Z. Zhou, H. Matsumoto, *Electrochem. Commun*. **2007**, *9*, 1017.

[2] D. R. MacFarlane, P. Meakin, J. Sun, N. Amini, M. Forsyth, *J. Phys. Chem. B* **1999**, *103*, 4164.

[3] P.-J. Alarco, Y. Abu-Lebdeh, A. Abouimrane, M. Armand, *Nat. Mater*. **2004**, *3*, 4761.

[4] D. R. MacFarlane, P. Meakin, J. Sun, N. Amini, M. Forsyth, *J. Phys. Chem. B* **1999**, *103*, 4164.

[5] T. Enomoto, S. Kanematsu, K. Tsunashima, K. Matsumoto, R. Hagiwara, *Phys. Chem. Chem. Phys.* **2011**, *13*, 12536.

[6] K. Matsumoto, R. Hagiwara, Y. Ito, *Electrochem. Solid-State Lett*. **2004**, *7*, E41.

[7] I. Gennick, K. M. Harmon, M. M. Potvin, *Inorg. Chem.* **1977**, *16*, 2033.

[8] R. Hagiwara, K. Matsumoto, Y. Nakamori, T. Tsuda, Y. ito, H. Matsumoto, K. Momota, *J. Electrochem. Soc.* **2003**, *150*, D195.

[9] S. Forsyth, S. R. Batten, Q. Dai, D. R. MacFarlane, *Aust. J. Chem.* **2004**, *57*, 121.

[10] J. Timmermans, *J. Phys. Chem. Solids* **1961**, *18*, 1.

[11] D. R. MacFarlane, J. Huang, M. Forsyth, *Nature* **1999**, *402*, 792.

[12] G. Annat, J. Adebahr, I. R. McKinnon, D. R. MacFarlane, M. Forsyth, *Solid State Ionics* **2007**, *178*, 1065.

[13] J. Sun, D. R. MacFarlane, M. Forsyth, *Solid State Ionics* **2002**, *148*, 145.

[14] K. Kuchitsu, H. Ono, S. Ishimaru, R. Ikeda, H. Ishida, *Phys. Chem. Chem. Phys*. **2000**, *2*, 3883.

[15] A. J. Hill, J. Huang, J. Efthimiadis, P. Meakin, M. Forsyth, D. R. MacFarlane, *Solid State Ionics* **2002**, *154–155*, 119.

[16] P.-J. Alarco. Y. Abu-Lebdeh, N. Ravet, M. Armand, *Solid State Ionics* **2004**, *172*, 53.

[17] K. R. Harris, *J. Phys. Chem. B* **2010**, *114*, 957.

[18] Ç. Tasseven, J. Trullàs, O. Alcaraz, M. Silbert, A. Giró, *J. Chem. Phys.* **1997**, *106*, 7286.

[19] S. Hull, In *Solid State Electrochemistry I.* V. V. Kharton, Ed.; Wiley-VCH Verlag: Weinheim, Germany, **2009**.

[20] M. Anouti, M. Caillon-Caravaner, Y. Dridi, H. Galiano, D. Lemordant, *J. Phys. Chem. B* **2008**, *112*, 13335.

[21] J. Efthimiadis, M. Forsyth, D. R. MacFarlane, *J. Mater. Sci.* **2003**, *38*, 3293.

[22] J. Efthimiadis, S. J. Pas, M. Forsyth, D. R. MacFarlane, *Solid State Ionics* **2002**, *154–155*, 279.

[23] T. Enomono, Y. Nakamori, K. Matsumono, R. Hagiwara, *J. Phys. Chem. C* **2011**, *115*, 4324.

[24] R. Hagiwara, Y. Nakamori, K. Matsumoto, Y. Ito, *J. Phys. Chem. B* **2005**, *109, * 5445.

Table 3–1. Ionic conductivities (σ) for DMPyr(FH)$_2$F and EMPyr(FH)$_2$F at different temperatures.

DMPyr(FH)$_2$F		EMPyr(FH)$_2$F	
T / K	σ / mS cm^{-1}	T / K	σ / mS cm^{-1}
353	170	343	142
343	154	333	128
333	139	323	113
313	14.3	308	91.1
298	10.3	288	14.4
288	8.06	278	9.38
283	7.12	268	6.87
268	4.70	258	4.98
256	4.09	243	2.46
253	2.89	223	0.034
243	0.034	218	0.018
238	0.007	213	0.011
233	0.002	203	0.004

Table 3–2. Diffusion coefficients of cation (D_{cation}) and anion (D_{anion}) for DMPyr(FH)$_2$F and EMPyr(FH)$_2$F at different temperatures.

T	DMPyr(FH)$_2$F		EMPyr(FH)$_2$F	
	D_{cation}	D_{anion}	D_{cation}	D_{anion}
/ K	/ 10^{-6} cm^2 s^{-1}		/ 10^{-6} cm^2 s^{-1}	
248			0.189	0.118
258			0.279	0.163
268			0.386	0.200
278			0.482	0.265
288			0.639	1.14
298		0.344	0.870	2.15
308		0.361	1.02	2.94
318	1.10	0.482	1.30	3.26
328	1.46	3.60	1.54	4.02
338	1.83	4.81	1.87	4.53
348	2.12	5.71		
358	2.37	6.68		
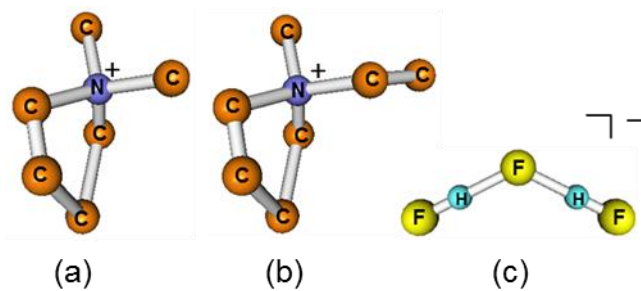
Figure 3–1. Structures of (a) DMPyr$^+$, (b) EMPyr$^+$, and (c) (FH)$_2$F$^-$. The hydrogen atoms in the cations are omitted for clarity.
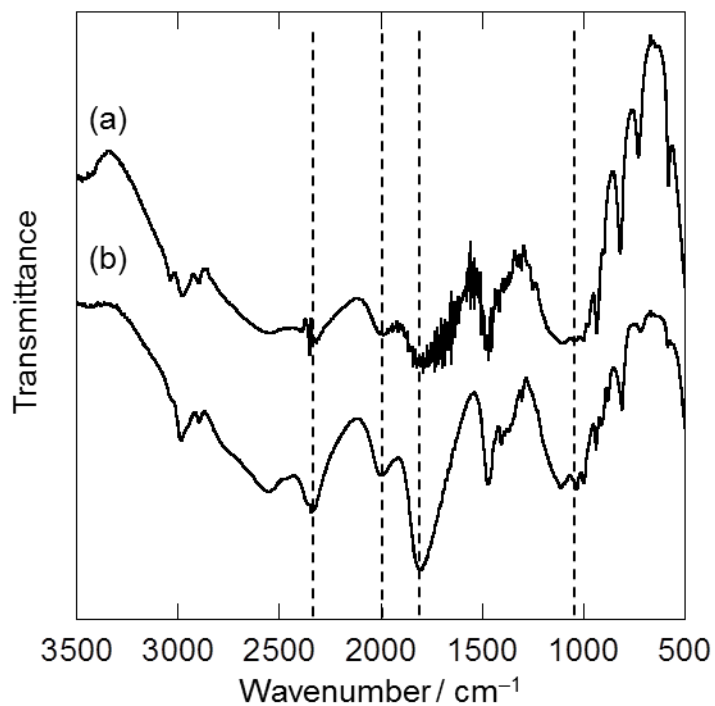
Figure 3–2. The IR spectra for (a) DMPyr(FH)$_2$F and (b) EMPyr(FH)$_2$F. The dashed lines denote the positions of (FH)$_2$F$^-$ found in the solid state such as potassium salts.
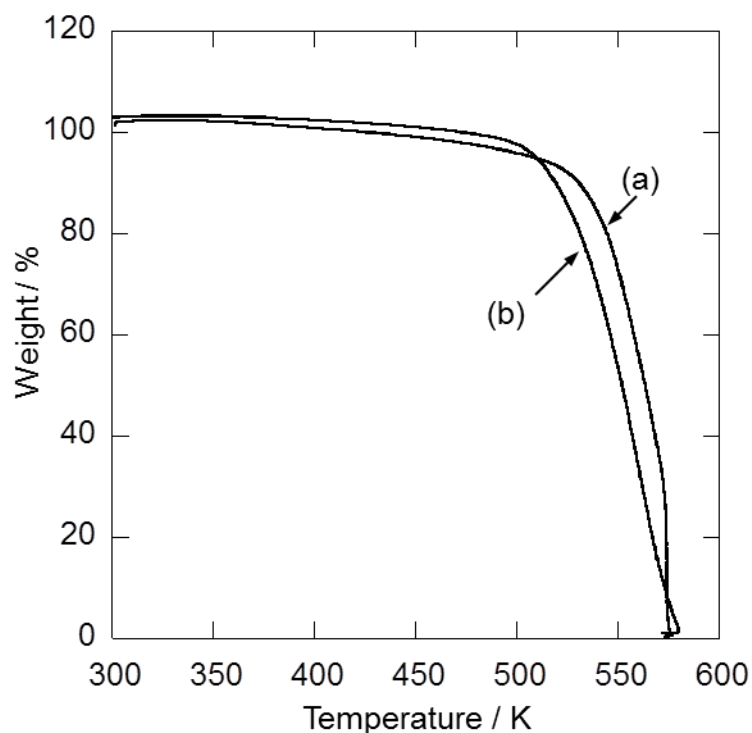
Figure 3–3. Thermogravimetric curves for (a) DMPyr(FH)$_2$F and (b) EMPyr(FH)$_2$F. Scan rate: 10 K min^{-1}.
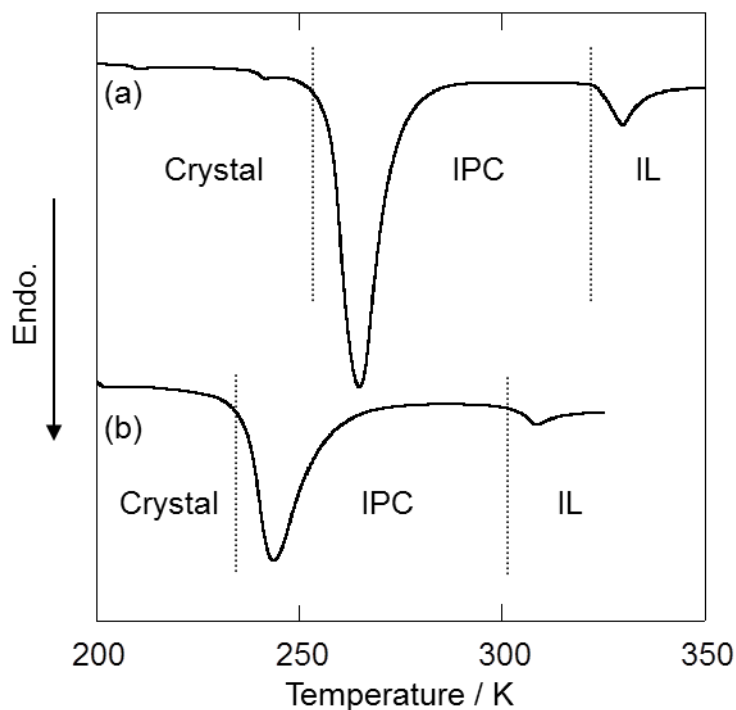
Figure 3–4. Differential scanning calorimetric curves for (a) DMPyr(FH)$_2$F and (b) EMPyr(FH)$_2$F. $\Delta H = 14.7$ kJ mol^{-1} at 258 K (crystal to IPC) and 1.3 kJ mol^{-1} at 325 K (IPC to IL) for DMPyr(FH)$_2$F. $\Delta H = 9.9$ kJ mol^{-1} at 236 K (crystal to IPC) and 0.6 kJ mol^{-1} at 303 K (IPC to IL) for EMPyr(FH)$_2$F.
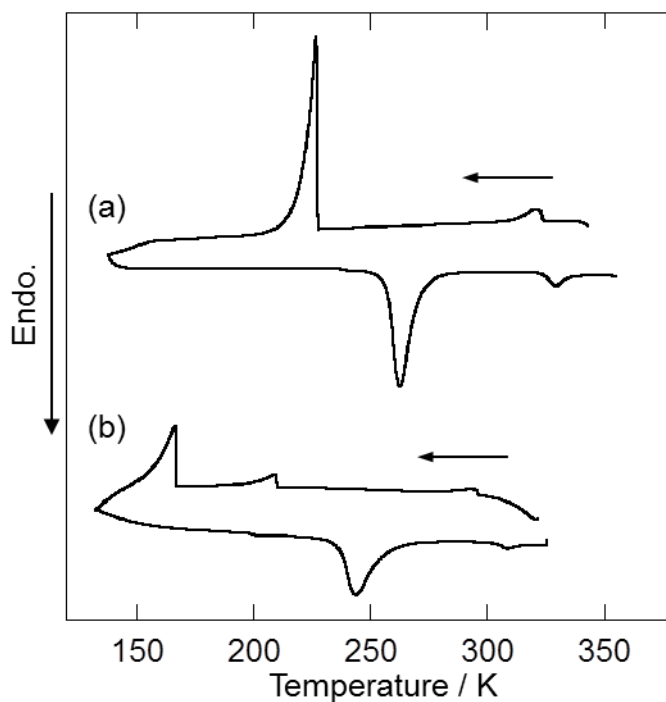
Figure 3–5. Entire DSC curves for (a) DMPyr(FH)$_2$F and (b) EMPyr(FH)$_2$F.

51
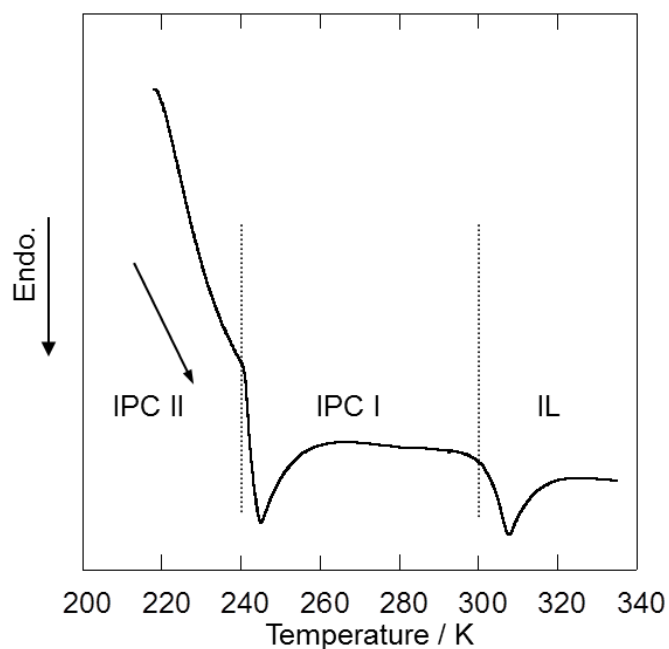
Figure 3–6. Different scanning calorimetric curve for EMPyr(FH)$_2$F when the scanning direction was reversed at 200 K.
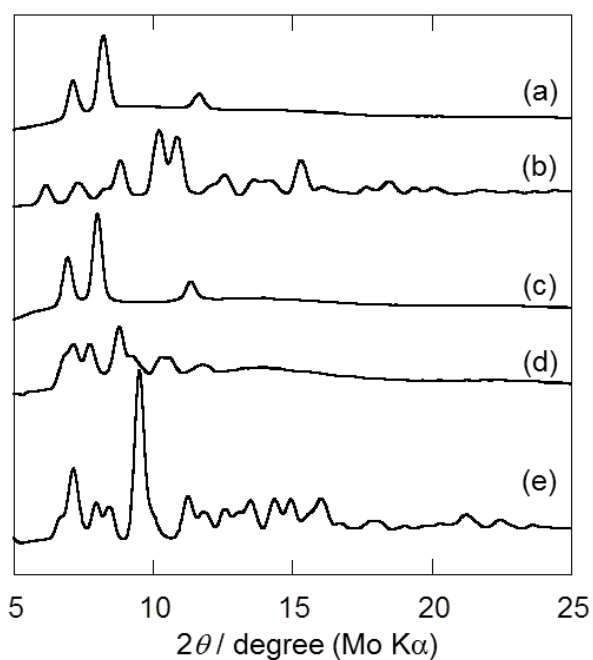
Figure 3–7. X-ray diffraction patterns of (a) the IPC phase of DMPyr(FH)$_2$F at 298 K, (b) the crystal phase of DMPyr(FH)$_2$F at 203 K, (c) the IPC phase of EMPyr(FH)$_2$F at 263 K, and (d) the crystal phase of EMPyr(FH)$_2$F at 183 K. All XRD patterns were obtained in the heating process.
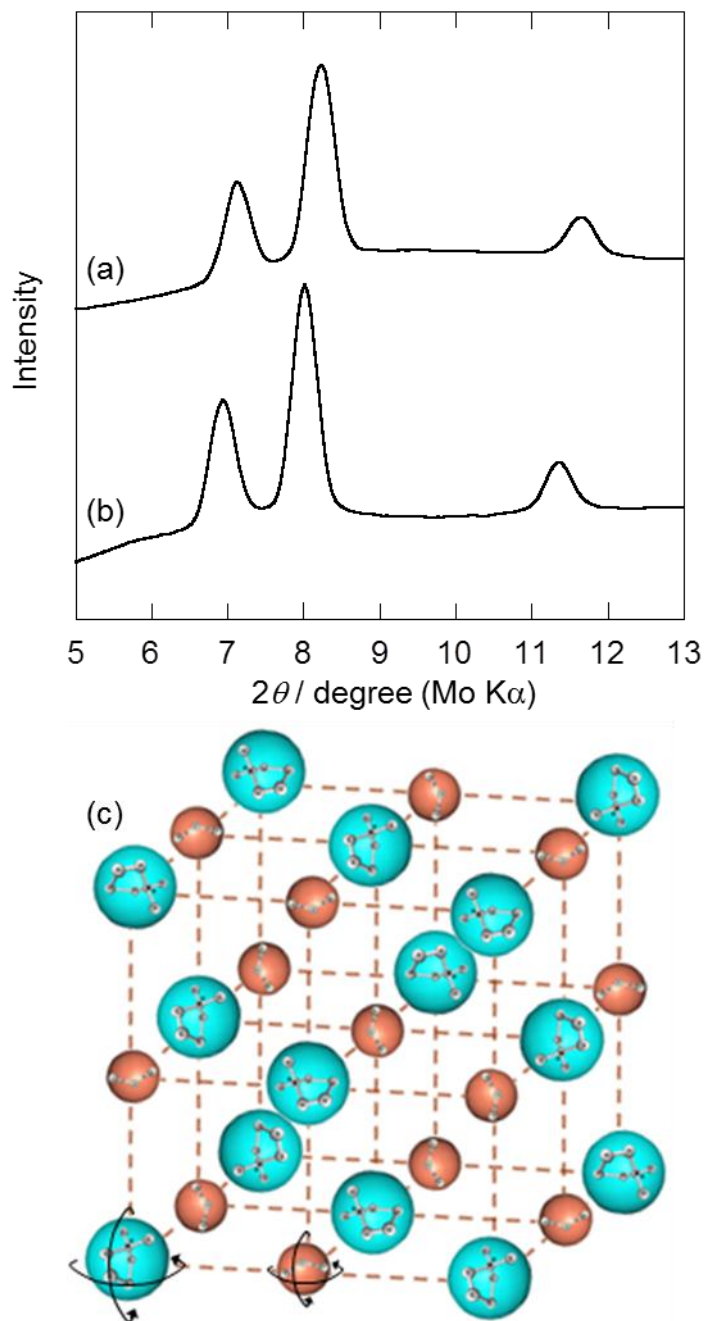
Figure 3–8. X-ray diffraction patterns of the IPC phases of (a) DMPyr(FH)$_2$F and (b) EMPyr(FH)$_2$F, and (c) a schematic model of the IPC phase.
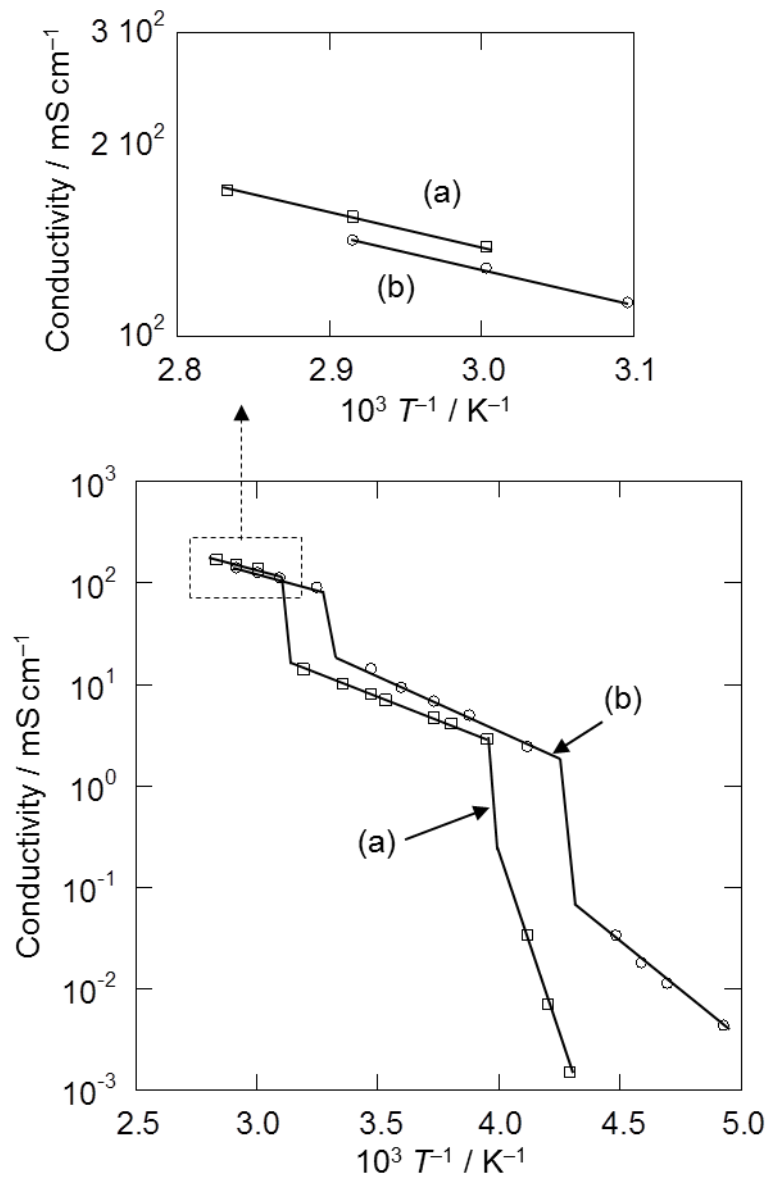
Figure 3–9. Arrhenius plots of ionic conductivity for (a) DMPyr(FH)$_2$F and (b) EMPyr(FH)$_2$F.
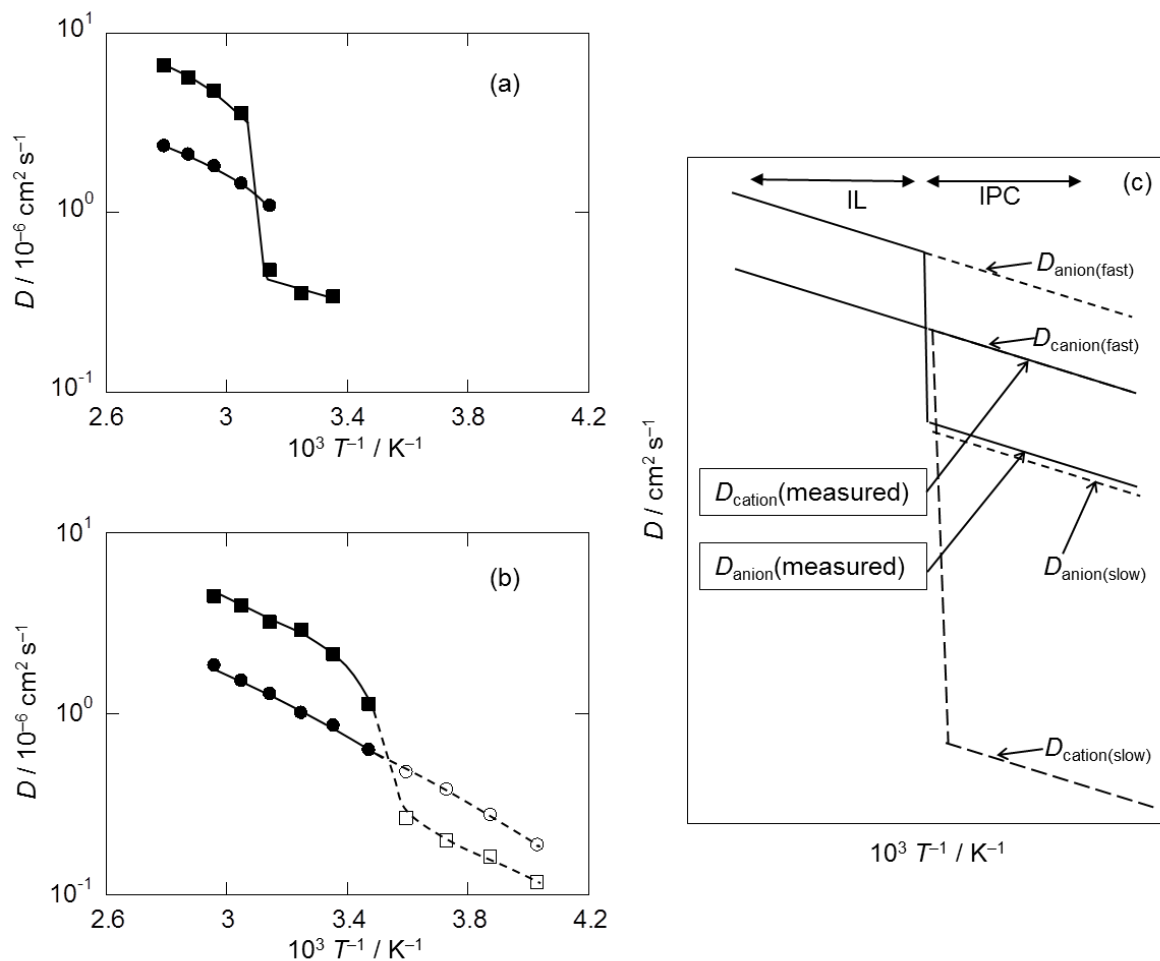
Figure 3–10. Arrhenius plots of self-diffusion coefficients for (a) DMPyr(FH)$_2$F, (b) EMPyr(FH)$_2$F, and (c) schematic illustration of the diffusion behavior of ions in the IPC temperature range for EMPyr(FH)$_2$F. The symbols ● and ■ denote self-diffusion coefficients of the cation and anion, respectively, in the IL temperature range. The symbols ○ and □ mean diffusion coefficients of the cation and anion, respectively, in the IPC temperature range.
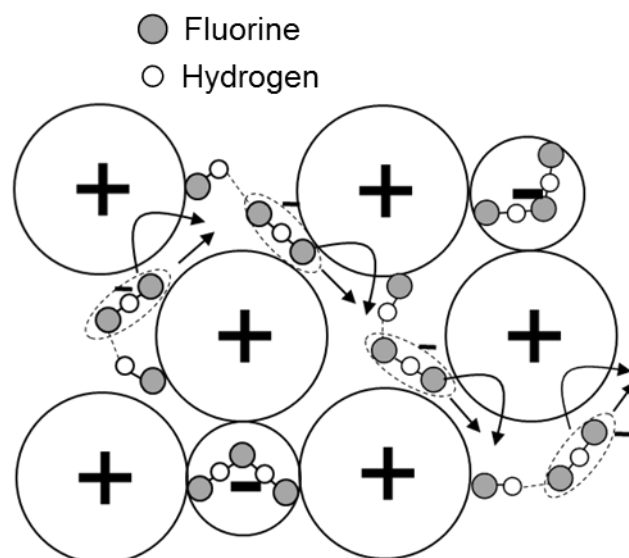
Figure 3–11. Possible ion conduction mechanism in the IPC phase of DMPyr(FH)$_2$F. The bent and straight arrows denote the diffusion paths of the anion along the [111] and [110] directions, respectively.
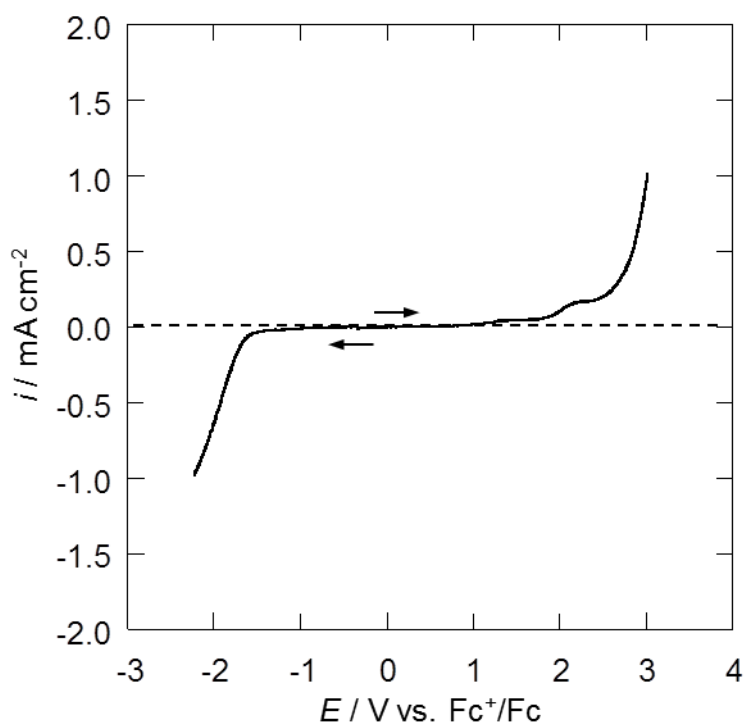
Figure 3–12. Linear sweep voltammogram of a vitreous carbon electrode in the IPC phase of DMPyr(FH)$_2$F at 298 K.

Chapter 4

Pyrrolidinium cation based fluorohydrogenate salts with different HF contents in the anions

4.1 Introduction

As described in Chapter 3, $DMPyr(FH)_{2.0}F$ and $EMPyr(FH)_{2.0}F$ have the highly conductive IPC phase around room temperature, which gives the potential use as electrolytes in all solid-state electrochemical devices. The low- and high-temperature limits of the IPC phase are determined by a phase transition temperature from crystal to IPC and melting point; 258 and 325 K for $DMPyr(FH)_{2.0}F$ and 236 and 303 K for $EMPyr(FH)_{2.0}F$, respectively. Operation of electrochemical devices at high temperature (e.g., 373 K) cannot be achieved in these salts due to the narrow IPC temperature regions, in particular, the high-temperature limit. In some cases, the high-temperature limit of the IPC phase can be increased by designing the structure of anions and organic cations without the low-temperature limit increasing [1–9]. In the cases of fluorohydrogenate salts, the melting point depends on the HF content in fluorohydrogenate anions [10–12]. The HF content (n) of the vacuum stable salt is controlled by elimination of HF at elevated temperature, where anionic species in fluorohydrogenate salts for $1.0 \leq n \leq 2.0$ are FHF^- and $(FH)_2F^-$ and those for $2.0 \leq n \leq 3.0$ are $(FH)_2F^-$ and $(FH)_3F^-$ and the decrease in n in the $EMIm(FH)_nF$ and $C_{12}MIm(FH)_nF$ ($C_{12}MIm$; 1-dodecyl-3-methylimidazolium) increases the melting point [11,12]. The same trend was observed in the cases of alkali metal fluoride-HF system; the liquidus line increases overall with decrease in n, through several troughs around the eutectic points [13–15]. In this chapter, effects of n in $DMPyr(FH)_nF$ ($1.0 \leq n \leq 2.0$) and $EMPyr(FH)_nF$ ($1.0 \leq n \leq 2.3$) on the thermal and structural properties are discussed.

4.2 Experimental

The fluorohydrogenate salt, EMPyr(FH)$_n$F, was prepared in the same manner for the EMPyr(FH)$_{2.0}$F in Chapter 3. Pumping of EMPyr(FH)$_n$F at 298 and 393 K resulted in EMPyr(FH)$_{2.3}$F and EMPyr(FH)$_{1.2}$F, respectively. The bifluoride salt, EMPyr(FH)$_{1.0}$F, was prepared by neutralization of EMPyrOH by hydrofluoric acid. The EMPyrOH was prepared by anion exchange, passing aqueous EMPyrCl solution through the column filled with anion exchange resin (OH$^-$ type, Dowex Monosphere 550A, Aldrich). The concentration of hydrofluoric acid was controlled into around 1 M HF (aq) by diluting a commercial aqueous HF (Wako Pure Chemical Industries, 46%) with distilled water. The HF content in EMPyr(FH)$_n$F (1.0 < n < 2.3) was controlled by mixing EMPyr(FH)$_{2.3}$F with EMPyr(FH)$_{1.2}$F or EMPyr(FH)$_{1.0}$F. The anionic species of FHF$^-$, (FH)$_2$F$^-$, and (FH)$_3$F$^-$ in EMPyr(FH)$_n$F were identified by IR spectroscopy as shown in Figure 4–1, where the absorption band is ~1250 cm^{-1} for FHF$^-$, ~1800, ~1990 and ~2330 cm^{-1} for (FH)$_2$F$^-$, and 950 cm^{-1} for (FH)$_3$F$^-$ [11,16,17].

The fluorohydrogenate salt, DMPyr(FH)$_n$F, was also prepared in the same manner for DMPyr(FH)$_{2.0}$F in Chapter 3. Pumping of DMPyr(FH)$_n$F at 298 and 393 K resulted in DMPyr(FH)$_{2.0}$F and EMPyr(FH)$_{1.0}$F, respectively. The HF content in DMPyr(FH)$_n$F (1.0 < n < 2.0) was controlled by mixing DMPyr(FH)$_{1.0}$F with DMPyr(FH)$_{2.0}$F. The anionic species of FHF$^-$, (FH)$_2$F$^-$, and (FH)$_3$F$^-$ in EMPyr(FH)$_n$F were identified by IR spectroscopy as shown in Figure 4–2, where the absorption band is ~1240 cm^{-1} for FHF$^-$ and ~1790, ~1980, and ~2330 cm^{-1} for (FH)$_2$F$^-$ [11,16,17].

4.3 Results and discussion

4.3.1 Thermal and structural behavior of EMPyr(FH)$_n$F

Figure 4–3 shows the DSC curves of EMPyr(FH)$_n$F ($1.0 \leq n \leq 2.3$) in the heating process and Figure 4–4 shows the melting behavior of EMPyr(FH)$_n$F ($1.8 \leq n \leq 2.3$) in the heating process. Table 4–1 summarizes the DSC data of transition temperature, enthalpy change, and entropy change for EMPyr(FH)$_n$F ($1.0 \leq n \leq 2.3$). Figure 4–5 shows that the plot of DSC transitions for the EMPyr(FH)$_n$F system according to Figures 4–3 and 4–4, while each phase was identified with the aid of XRD analysis as described below. The IPC (I) and (II) phases in Figure 4–5 appear as a mesophase between crystal and liquid phases and the phase transitions from and to these phases in this plot do not satisfy the phase rule. This can be accepted by introducing another undetectable phase between the two phases (e.g., between IPC (I) and IL). This kind of the two-phase region was observed in previously known cases for organic plastic crystals [18–20].

Figure 4–6 shows the XRD patterns of the IPC (I) phase for EMPyr(FH)$_n$F in the HF content ranges of $1.0 \leq n \leq 1.2$ and $1.8 \leq n \leq 2.3$. Only three XRD diffraction peaks are observed in the low 2θ-angle region, as in the cases of the IPC phases with a NaCl-type lattice for EMPyr(FH)$_{2.0}$F in Chapter 3. Figure 4–7 shows the lattice constants of the NaCl-type IPC (I) phase of EMPyr(FH)$_n$F as a function of n. The difference in lattice constant between the two HF content ranges of $1.0 \leq n \leq 1.2$ and $1.8 \leq n \leq 2.3$ is due to the different size of FHF$^-$ and (FH)$_2$F$^-$ species (calculated volume at MP2/aug-cc-pVTZ: 47 Å^3 for FHF$^-$, 63 Å^3 for (FH)$_2$F$^-$, and for 84 Å^3 for (FH)$_3$F$^-$ [21]). In both the HF content ranges of $1.0 \leq n \leq 1.2$ and $1.8 \leq n \leq 2.3$, a slight increase in lattice constant was observed with increase in n. This behavior indicates that the IPC (I) forms a mixed crystal system with a NaCl-type structure over a wide range of n and the (FH)$_n$F$^-$ anions are randomly distributed in this lattice.

Figure 4–8 shows the enthalpy changes of phase transitions from the region B to the

59

region A and from the region A to IPC (I) for EMPyr(FH)$_n$F (2.0 ≤ n ≤ 2.3) (see Figure 4–5 for the definition of regions A and B). When n becomes close to 2.0, the enthalpy change of phase transitions from the region B to the region A decreases and that from the region A to IPC (I) increases. The intensity of these endothermic peaks was affected by the abundance ratio of (FH)$_2$F$^-$ and (FH)$_3$F$^-$. Figure 4–9 shows the XRD patterns of regions A, B, and C in EMPyr(FH)$_n$F (1.9 ≤ n ≤ 2.3). The XRD patterns of regions A and C are similar and are ascribed to the crystal phase of EMPyr(FH)$_2$F. The XRD patterns of the region B contain some peaks in addition to those of the crystal phase of EMPyr(FH)$_2$F (e.g., the peak at 7.6°). The results of DSC and XRD analysis suggest that these additional peaks in the region B are assigned to another phase with a larger n value, probably the crystal phase of EMPyr(FH)$_3$F. In the XRD pattern of EMPyr(FH)$_n$F (n < 1.8), the crystal phase of EMPyr(FH)$_2$F was not observed (Figure 4–10). The phase transition from the region B to the region A corresponds to transformation from EMPyr(FH)$_3$F crystal to IPC (II) and that from the region A to IPC (I) corresponds to transformations from EMPyr(FH)$_2$F crystal and from IPC (II) to IPC (I) (these transitions will be discussed below).

Figure 4–10 shows the XRD patterns of the phase around 243 K in EMPyr(FH)$_n$F (1.3 ≤ n ≤ 1.9). This region below 261 K is the IPC (II) phase. The XRD pattern of IPC (II) is different from that of the IPC (I) and the entropy of fusion for the IPC (II) phase (8 − 10 J K^{-1} mol^{-1}) is larger than those of the IPC (I) phase (1 − 3 J K^{-1} mol^{-1}) although both of them are small enough to be regarded as IPCs. Although the crystal structure of the IPC (II) was not determined in detail, the XRD patterns show that the IPC (II) lattice seems to belong to a less symmetric crystal system than that of the IPC (I) which belongs to a cubic system. As in the case of IPC (I), the XRD patterns of the IPC (II) shift gradually to the higher angle with decrease in n, indicating the IPC (II) also forms an IPC with randomly located anions over the wide composition of HF in (FH)$_n$F$^-$.

Figure 4–11 shows the DSC curves in the cooling process for EMPyr(FH)$_n$F ($1.9 \leq n \leq$ 2.3). In the cooling process, several solid phases were observed separately in EMPyr(FH)$_n$F ($1.9 \leq n \leq 2.3$); IPC (II) phase (described below) between IPC (I) and regions A or C. In the heating process, this IPC (II) phase is passed through the phase transition from region A to IPC (I) because the reports described in Chapter 3 showed that the small endothermic peak corresponding to the phase transition from IPC (II) to IPC (I) in the heating process overlaps with the large one from crystal EMPyr(FH)$_2$F to IPC (I). Figure 4–12 shows the XRD patterns of EMPyr(FH)$_{1.9}$F at 213 K, EMPyr(FH)$_{2.0}$F at 183 K, and EMPyr(FH)$_{2.1}$F at 183 K. The samples for this XRD measurement were cooled from room temperature to the target temperature as performed in DSC analysis in Figure 4–11. The XRD patterns in Figure 4–12 are coincident with those of the IPC (II) in Figure 4–10, indicating that the IPC (II) phase appears in the supercooled states for EMPyr(FH)$_{2.0}$F, EMPyr(FH)$_{2.1}$F, and EMPyr(FH)$_{2.2}$F. These behaviors suggest that in the heating process, EMPyr(FH)$_n$F ($2.1 \leq n \leq 2.3$) transforms from the crystal phase (EMPyr(FH)$_3$F and EMPyr(FH)$_2$F) to IPC (I) via the crystal phase (EMPyr(FH)$_2$F) and IPC (II), followed by melting.

Figure 4–13 shows the XRD patterns of the region D around 243 K in EMPyr(FH)$_n$F ($1.0 \leq n \leq 1.2$). The XRD patterns are different from those observed in this study (IPC (I), IPC (II), and regions A, B, and C). The major peaks in these XRD patterns are most probably attributed to the crystal phase of EMPyr(FH)$_1$F. The enthalpy change of phase transition in the range $n \leq$ 1.2 increases with decrease in n.

In the regions A, C, and D, the crystal phases of EMPyr(FH)$_2$F and EMPyr(FH)$_1$F are observed in the XRD patterns in Figures 4–9 and 4–13, respectively, however, these phases are not only the phases present in the regions since the n values are not integers. Considering the IPC (II) with the wide composition range of HF in fluorohydrogenate anions, the IPC (II) may coexist with crystal phases of EMPyr(FH)$_2$F and EMPyr(FH)$_1$F in the regions A, C, and

D although the XRD patterns of IPC (II) were not observed due to their relatively small amount.

4.3.2 Thermal and structural behavior of DMPyr(FH)$_n$F

Figure 4–14 shows the DSC curves of DMPyr(FH)$_n$F ($1.0 \leq n \leq 2.0$) in the heating process and Figure 4–15 shows the plot of DSC transitions for the DMPyr(FH)$_n$F system observed in Figures 4–14. Table 4–2 summarizes the DSC data of the transition temperature, enthalpy change, and entropy change for DMPyr(FH)$_n$F ($1.0 \leq n \leq 2.0$). The melting point in the DMPyr(FH)$_n$F system increases with decrease in n and is not observed in the range of $n \leq$ 1.5 because the thermal decomposition starts below the melting point (see Figure 4–16 for TG analysis).

Figure 4–17 shows that the XRD patterns of the IPC (I') phase for DMPyr(FH)$_n$F ($1.0 \leq n \leq 2.0$). The crystal structure is the NaCl-type whole in this range as in the case for DMPyr(FH)$_{2.0}$F in Chapter 3. Differently from the XRD patterns of the IPC (I) for EMPyr(FH)$_n$F (Figure 4–6), DMPyr(FH)$_n$F in the low HF content give small diffraction peaks with the indices of (311), (222), and (400) in addition to (111), (200), and (220). This probably results from the better crystal packing and lower thermal factor for each atom in the lattice of DMPyr(FH)$_n$F than those in the lattice of EMPyr(FH)$_n$F. A total of 6 Miller indices, (111), (200), (220), (311), (222), and (400), were observed even at higher temperature of 373 and 443 K as shown in Figure 4–18. Figure 4–19 shows the lattice constant as a function of n. The lattice constant of the IPC (I') decreases with decrease in n as in the cases of EMPyr(FH)$_n$F because of the smaller size of FHF$^-$ than that of (FH)$_2$F$^-$ [21].

Figure 4–20 shows the XRD patterns of the phase observed at 203 K for DMPyr(FH)$_n$F ($1.0 \leq n \leq 2.0$). The DMPyr(FH)$_1$F (n = 1.0) and DMPyr(FH)$_2$F (n = 2.0) salts have different XRD patterns and the XRD patterns of DMPyr(FH)$_n$F between 1.0 and 2.0 are composed of

those of DMPyr(FH)$_1$F (n = 1.0) and DMPyr(FH)$_2$F (n = 2.0), suggesting that DMPyr(FH)$_n$F (1.0 < n < 2.0) in the low temperature region is the mixture of these two crystal phases.

4.3.3 Differences in thermal properties between EMPyr(FH)$_n$F and DMPyr(FH)$_n$F

The phase diagram of the EMPyr(FH)$_n$F system is more complicated than that of DMPyr(FH)$_n$F. As described in Chapter 3, all the DMPyr$^+$ cations are immobilized in the framework of the crystal lattice. On the other hand, a part of EMPyr$^+$ cations is mobile in the IPC (I) of EMPyr(FH)$_{2.0}$F and the remaining EMPyr$^+$ cations are fixed to the framework of the crystal lattice. The IPC (I) lattice of EMPyr(FH)$_{2.0}$F has a looser packing than that of DMPyr(FH)$_{2.0}$F because of the lower symmetry of EMPyr$^+$ than that of DMPyr$^+$.

In the case of EMPyr(FH)$_n$F, the melting point becomes maximal at n = 2.0. When n varies from 2.0, the gap from 2.0 results in the existence of FHF$^-$ (n < 2.0) or (FH)$_3$F$^-$ (n > 2.0) in the IPC (I) of EMPyr(FH)$_{2.0}$F, which destabilizes the framework of the IPC (I) lattice. This increases the number of mobile EMPyr$^+$ cations, which leads to further instability of the lattice. In the HF content range of 1.3 ≤ n ≤ 1.7, the IPC (I) becomes less stable than the IPC (II) due to this further instabilizing effect on IPC (I). The IPC (I') of DMPyr(FH)$_n$F is also instabilized by the shift of n from 2.0, but the absence of mobile DMPyr$^+$ cations prevents this lattice from melting.

References

[1] G. Zabinska, P. Ferloni, M. Sanesi, *Thermochim. Acta* **1987**, *122*, 87.

[2] V. Armel, D. Velayutham, J. Sun, P. C. Howlett, M. Forsyth, D. R. MacFarlane, J. M. Pringle, *J. Mater. Chem.* **2011**, *21*, 7640.

[3] D. R. MacFarlane, P. Meakin, J. Sun, N. Amini, M. Forsyth, *J. Phys. Chem. B* **1999**, *103*, 4164.

[4] M. Moriya, D. Kato, W. Sakamoto, T. Yogo, *Chem. Commun.* **2011**, *47*, 6311.

[5] H.-B. Han, J. Nie, K. Liu, W.-K. Li, W.-F. Feng, M. Armand, H. Matsumoto, Z.-B. Zhou, *Electrochim. Acta* **2010**, *55*, 1221.

[6] P.-J. Alarco, Y. Abu-Lebdeh, M. Armand, *Solid States Ionics* **2004**, *175*, 717.

[7] Z.-B. Zhou, H. Matsumoto, *Electrochem. Commun.* **2007**, *9*, 1017.

[8] Z.-B. Zhou, H. Matsumoto, K. Tatsumi, *Chem. Eur. J.* **2005**, *11*, 752.

[9] D. R. MacFarlane, P. Meakin, N. Amini, M. Forsyth, *J. Phys.: Condens. Matter* **2001**, *13*, 8257.

[10] K. Matsumoto, J. Ohtsuki, R. Hagiwara, S. Matsubara, *J. Fluorine Chem.* **2006**, *127*, 1339.

[11] R. Hagiwara, Y. Nakamori, K. Matsumoto, Y. Ito, *J. Phys. Chem. B* **2005**, *109*, 5445.

[12] F. Xu, K. Matsumoto, R. Hagiwara, *J. Phys. Chem. B* **2012**, *116*, 10106.

[13] G. H. Cady, *J. Am. Chem. Soc.* **1934**, *56*, 1431.

[14] B. Boinon, A. Marchand, R. Cohen-Adad, *J. Therm. Anal.* **1976**, *10*, 411.

[15] R. V. Winsor, G. H. Cady, *J. Am. Chem. Soc.* **1948**, *70*, 1500.

[16] I. Gennick, K. M. Harmon, M. M. Potvin, *Inorg. Chem.* **1977**, *16*, 2033.

[17] R. Hagiwara, K. Matsumoto, Y. Nakamori, T. Tsuda, Y. ito, H. Matsumoto, K. Momota, *J. Electrochem. Soc.* **2003**, *150*, D195.

[18] D. Chandra, W. Ding, R. A. Lynch, J. J. Tomilinson, *J. Less–Common Met.* **1991**, *168*,

159.

[19] J. Salud, D. O. López, M. Barrio, J. L. Tamarit, H. A. J. Oonk, P. Negrier, Y. Haget, *J. Solid State Chem.* **1997**, *133*, 536.

[20] R. Russell, R. Chellappa, D. Chandra, *CALPHAD: Comput. Coupling Phase Diagrams Thermochem.* **2004**, *28*, 41.

[21] T. Enomoto, Y. Nakamori, K. Matsumoto, R. Hagiwara, *J. Phys. Chem. C* **2011**, *115*, 4324.

Table 4–1. Summary of the DSC analysis for EMPyr(FH)$_n$F ($1.0 \le n \le 2.3$).

n	$T_{s-s}{}^{a}$ / K	ΔH / kJ mol^{-1}	ΔS / J mol^{-1} K^{-1}	$T_{m}{}^{b}$ / K	ΔH / kJ mol^{-1}	ΔS / J mol^{-1} K^{-1}
1.0	279, 288	4.4, 4.1	16, 14	–	–	–
1.1	276	8.5	31	–	–	–
1.2	268	3.4	13	372	0.5	1.2
1.3	–	–	–	269	2.4	8.9
1.4	–	–	–	268	2.7	9.9
1.5	–	–	–	261	2.2	8.4
1.6	–	–	–	262	2.5	9.6
1.7	–	–	–	259	2.3	8.8
1.8	261	2.2	8.3	274	0.41	1.5
1.9	232, 253	7.0, 2.0	30, 7.8	298	0.79	2.7
2.0^{c}	236	9.9	42	303	0.64	2.0
2.1	197, 227	1.9, 5.5	9.7, 24	281	0.86	3.1
2.2	198, 218	3.1, 4.8	15, 22	249	0.64	2.6
2.3	196, 210	4.6, 3.6	24, 17	236	0.54	2.3

^{a}Solid–solid phase transition temperature. ^{b}Melting point. ^{c}R. Taniki, *Chapter 3 of this PhD thesis*, 2013.

Table 4–2. Summary of the DSC analysis for DMPyr(FH)$_n$F ($1.0 \le n \le 2.0$).

n	$T_{s-s}{}^{a}$ / K	ΔH / kJ mol^{-1}	ΔS / J mol^{-1} K^{-1}	$T_{m}{}^{b}$ / K	ΔH / kJ mol^{-1}	ΔS / J mol^{-1} K^{-1}
1.0	246	8.1	33			
1.1	243	8.8	36			
1.2	234	7.4	31			
1.3	235	7.7	33			
1.4	235	7.6	32			
1.5	230, 235	1.3, 5.2	5.4, 22			
1.6	241	7.4	31	422		
1.7	242	11	47	364	1.9	5.2
1.8	233, 245	0.68, 12	2.9, 51	351	1.5	4.3
1.9	251	14	58	338	1.6	4.6
2.0^{c}	258	15	57	325	1.3	4.1

^{a}Solid–solid phase transition temperature. ^{b}Melting point. ^{c}R. Taniki, *Chapter 3 of this PhD thesis*, 2013.
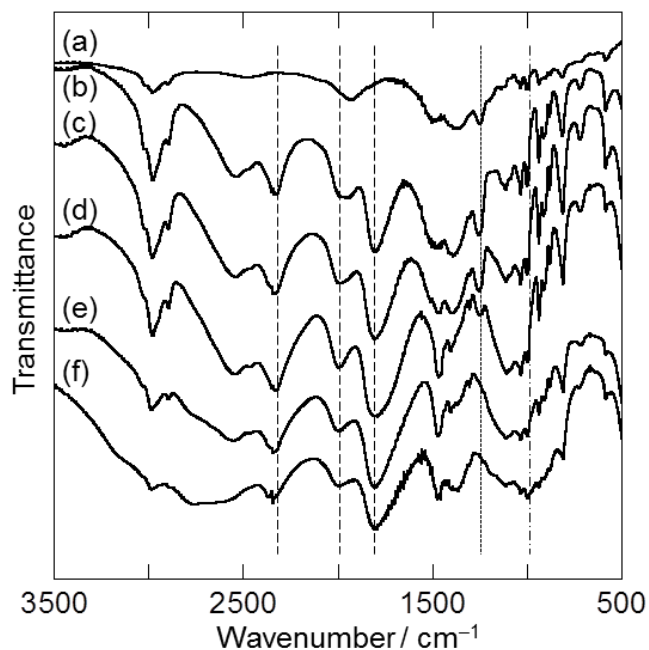
Figure 4–1. Infrared spectra for EMPyr(FH)$_n$F; n = (a) 1.0, (b) 1.3, (c) 1.5, (d) 1.8, (e) 2.0, and (f) 2.3. The dotted line (⋯⋯), dashed lines (– – –), and long dashed dotted line (· – · –) denote the positions of $(FH)_1F^-$, $(FH)_2F^-$, and $(FH)_3F^-$, respectively [11,16,17].
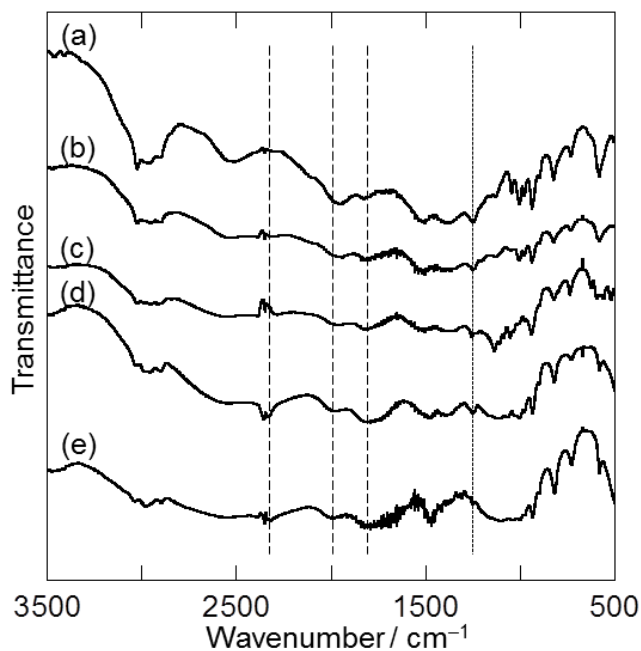
Figure 4–2. Infrared spectra for DMPyr(FH)$_n$F; n = (a) 1.0, (b) 1.3, (c) 1.5, (d) 1.8, and (e) 2.0. The dotted line (⋯⋯) and dashed lines (– – –) denote the positions of $(FH)_1F^-$ and $(FH)_2F^-$, respectively [11,16,17].
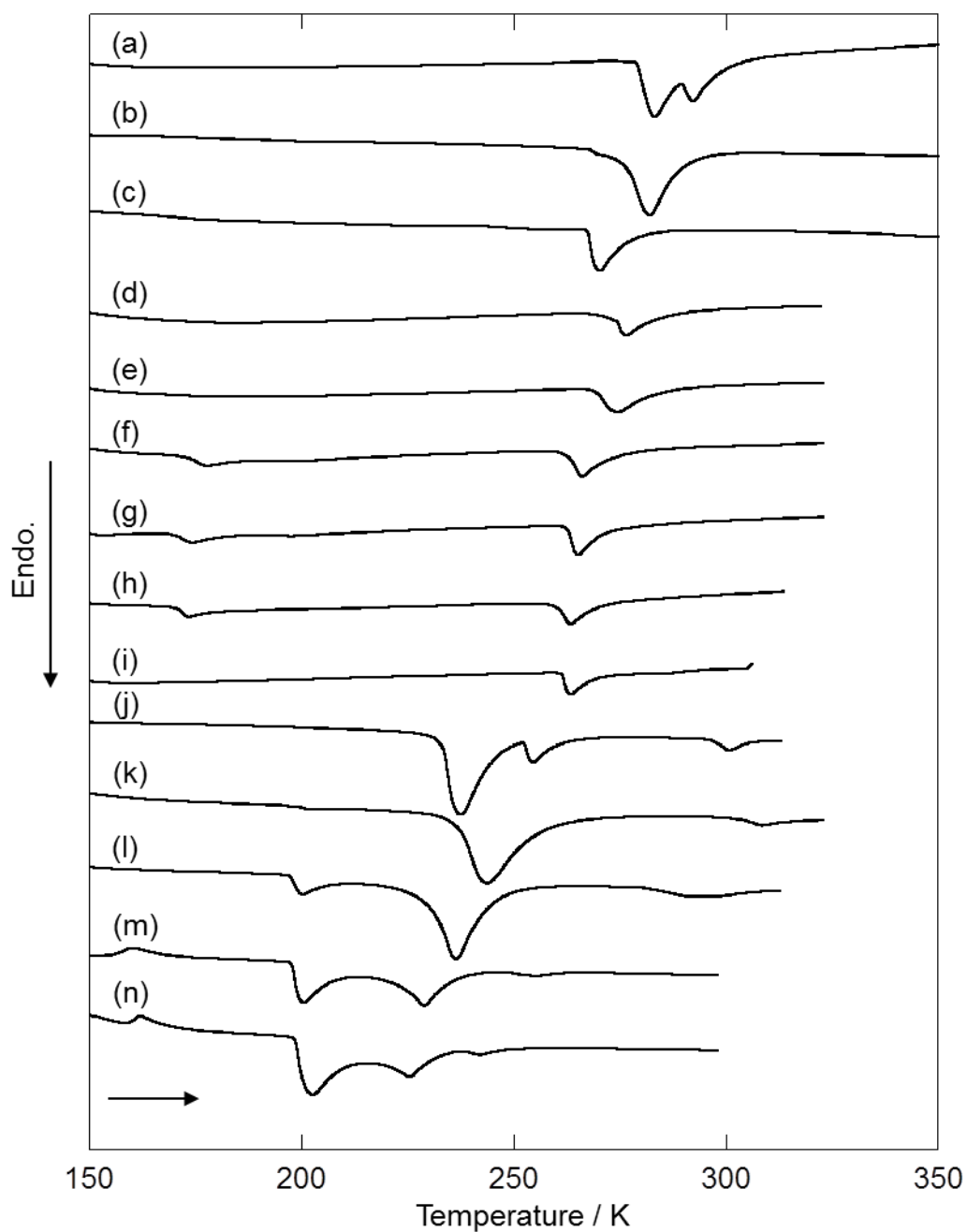
Figure 4–3. Differential scanning calorimetric curves for EMPyr(FH)$_n$F in the range of $1.0 \leq n$ ≤ 2.3; (a) 1.0, (b)1.1, (c) 1.2, (d) 1.3, (e) 1.4, (f) 1.5, (g) 1.6, (h) 1.7, (i) 1.8, (j) 1.9, (k) 2.0, (l) 2.1, (m) 2.2, and (n) 2.3.
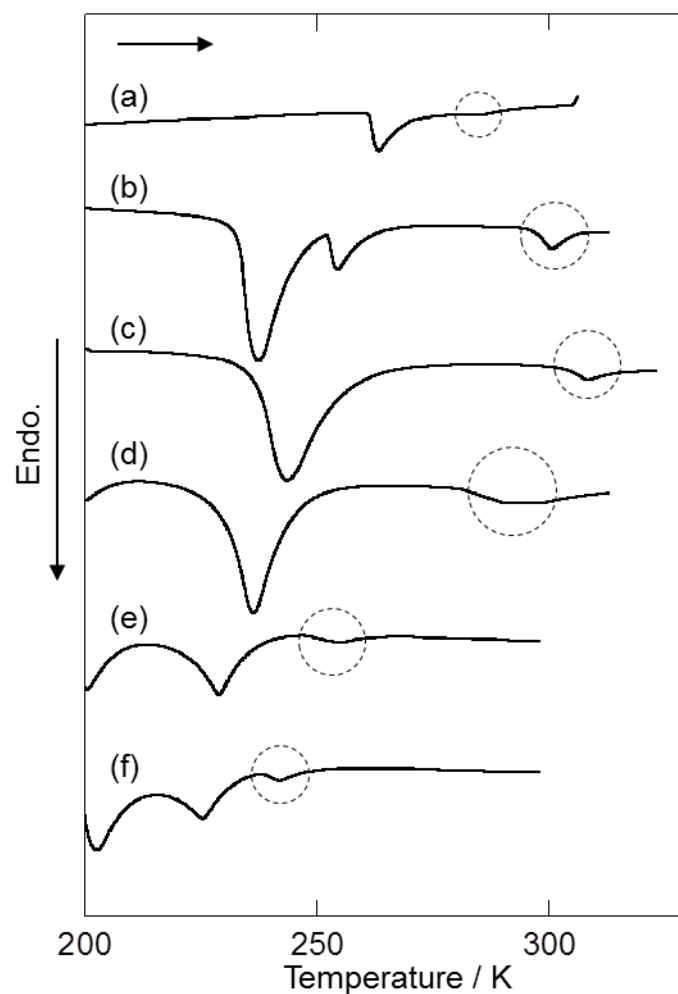
Figure 4–4. The magnification of DSC curves (Figure 4–3) for EMPyr(FH)$_n$F in the range of 1.8 ≤ n ≤ 2.3; (a) 1.8, (b)1.9, (c) 2.0, (d) 2.1, (e) 2.2, and (f) 2.3. The dotted circles denote melting.
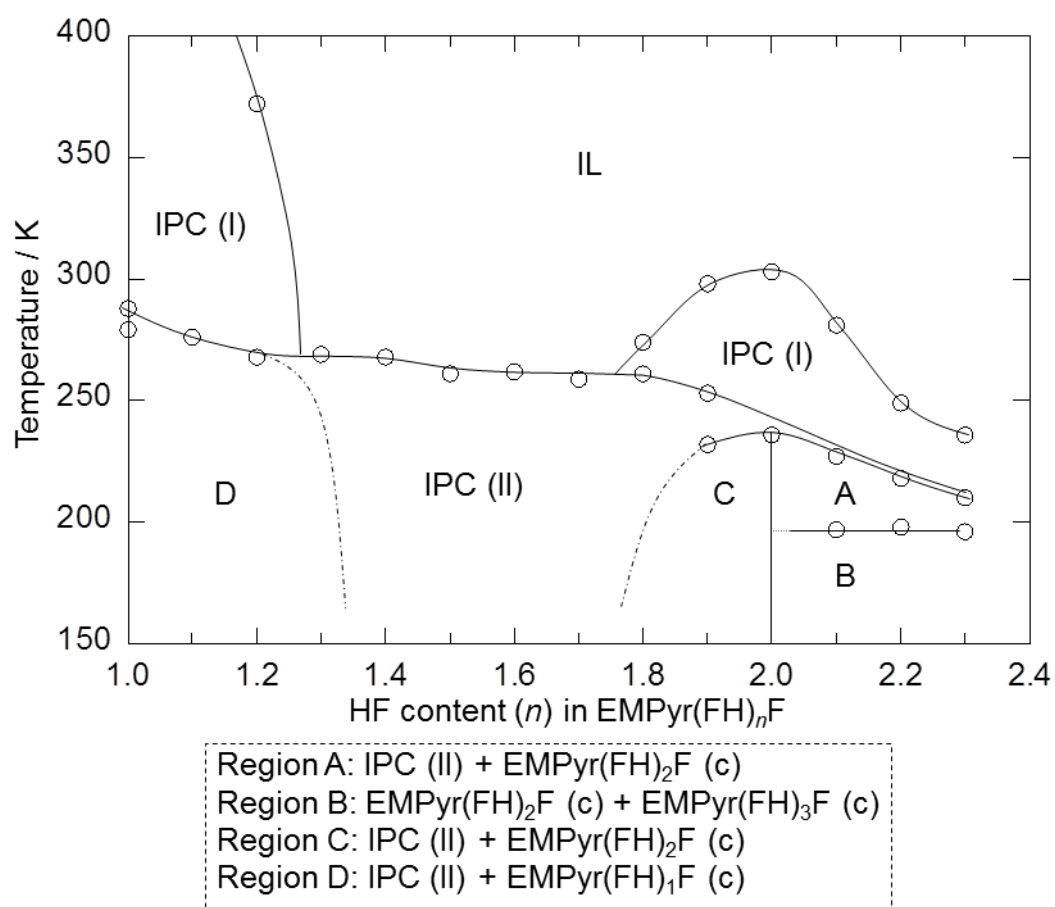
Figure 4–5. Plot of DSC transitions for the EMPyr(FH)$_n$F system. IL, ionic liquid phase; IPC (I), ionic plastic crystal phase (I); IPC (II), ionic plastic crystal phase (II); EMPyr(FH)$_1$F (c), crystal phase of EMPyr(FH)$_1$F; EMPyr(FH)$_2$F (c), crystal phase of EMPyr(FH)$_2$F; EMPyr(FH)$_3$F (c), crystal phase of EMPyr(FH)$_3$F.
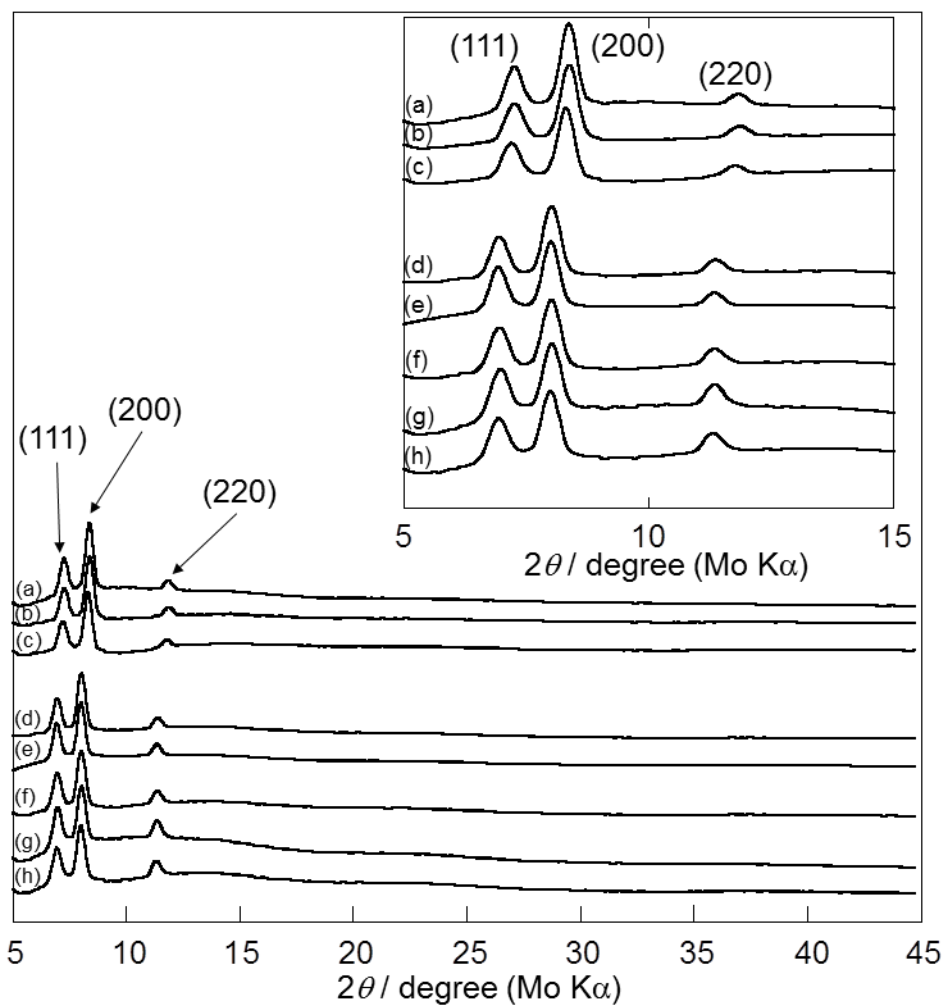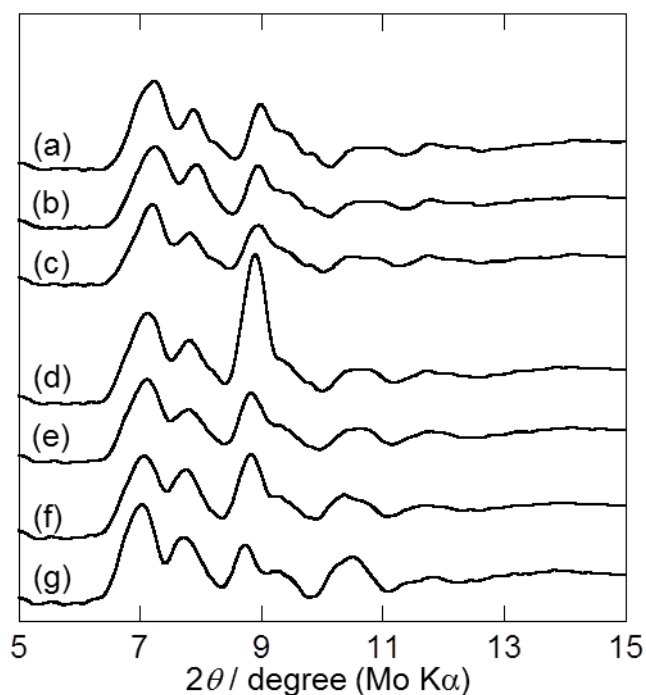
Figure 4–6. X-ray diffraction patterns of EMPyr(FH)$_n$F; (a) $n = 1.0$ at 298 K, (b) $n = 1.1$ at 298 K, (c) $n = 1.2$ at 298 K, (d) $n = 1.9$ at 273 K, (e) $n = 2.0$ at 263 K, (f) $n = 2.1$ at 243 K, (g) $n = 2.2$ at 243 K, and (h) $n = 2.3$ at 213 K.
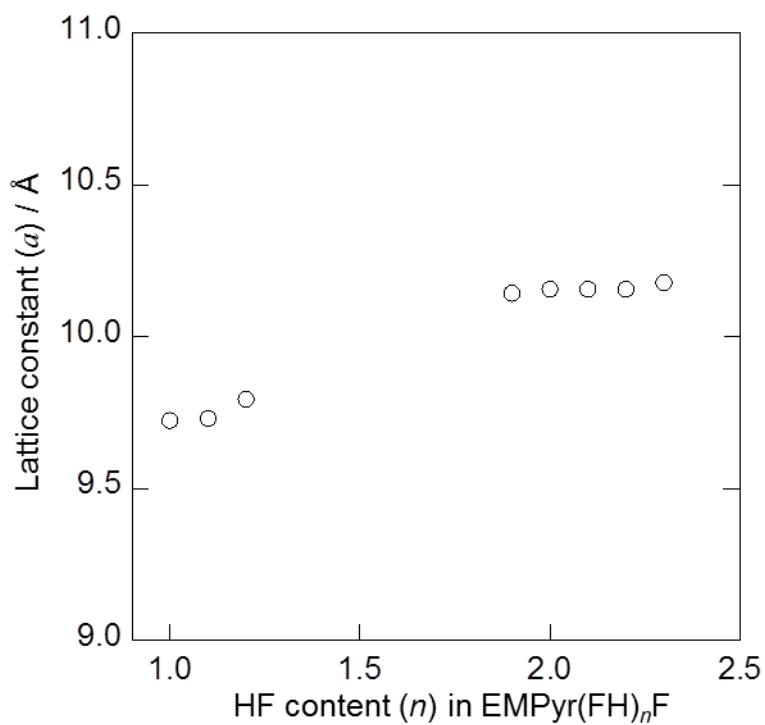
Figure 4–7. The lattice constant (a) of the IPC (I) of EMPyr(FH)$_n$F. Measuring temperature is written in Figure 4–6.
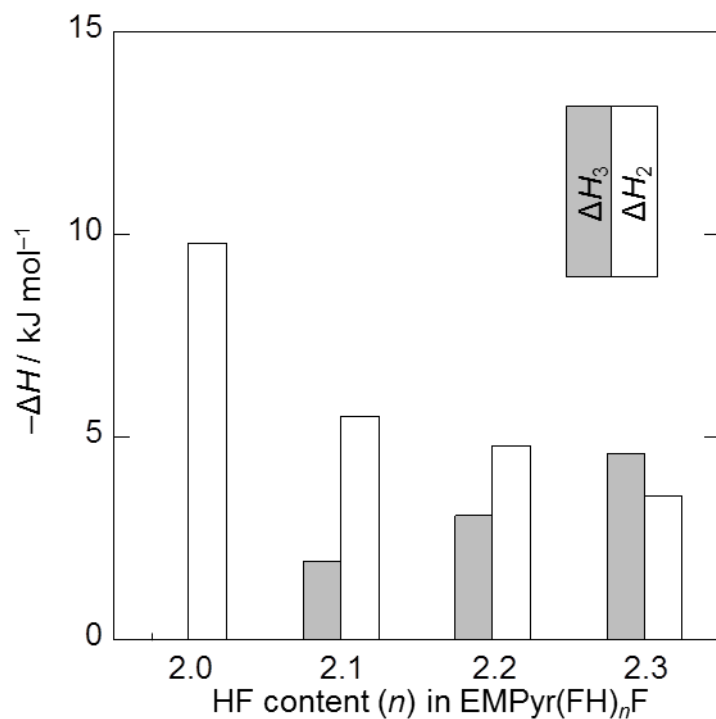
Figure 4–8. Enthalpy changes of phase transitions corresponding to crystal EMPyr(FH)$_3$F (ΔH_3) and to crystal EMPyr(FH)$_2$F (ΔH_2) in EMPyr(FH)$_n$F ($2.0 \leq n \leq 2.3$).
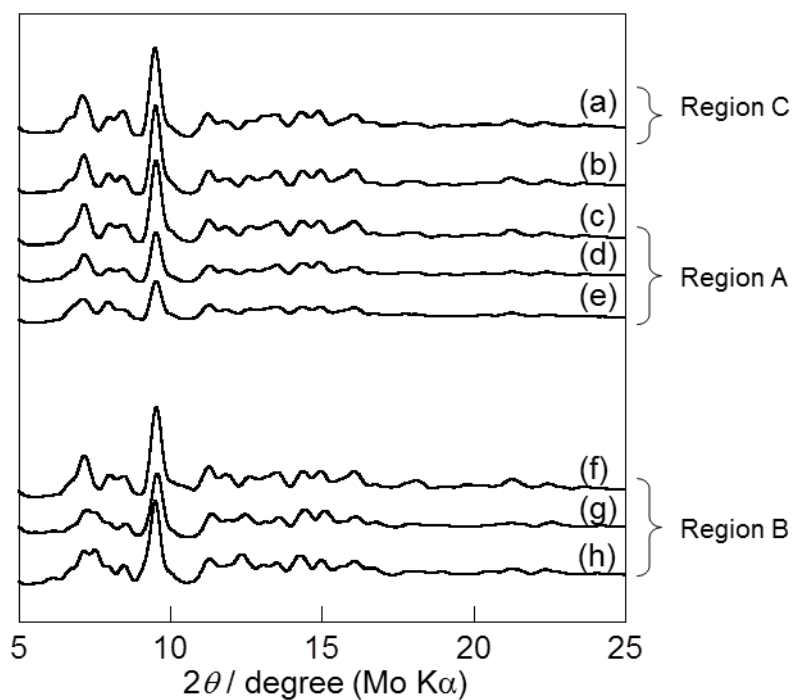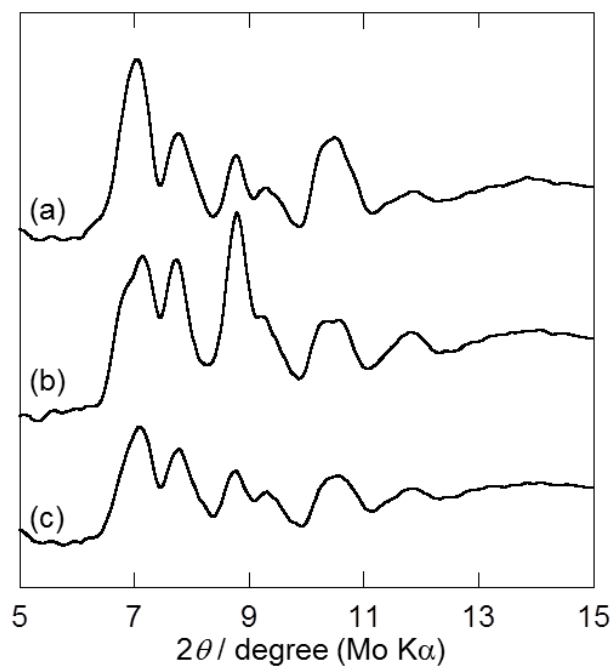
Figure 4–9. X-ray diffraction patterns of EMPyr(FH)$_n$F; (a) $n = 1.9$ at 213 K, (b) $n = 2.0$ at 183 K, (c) $n = 2.1$ at 203 K, (d) $n = 2.2$ at 203 K, (e) $n = 2.3$ at 203 K, (f) $n = 2.1$ at 183 K, (g) $n = 2.2$ at 183 K, and (h) $n = 2.3$ at 183 K.

Figure 4–10. X-ray diffraction patterns of EMPyr(FH)$_n$F; (a) $n = 1.3$ at 243 K, (b) $n = 1.4$ at 243 K, (c) $n = 1.5$ at 243 K, (d) $n = 1.6$ at 243 K, (e) $n = 1.7$ at 243 K, (f) $n = 1.8$ at 243 K, and (g) $n = 1.9$ at 238 K.
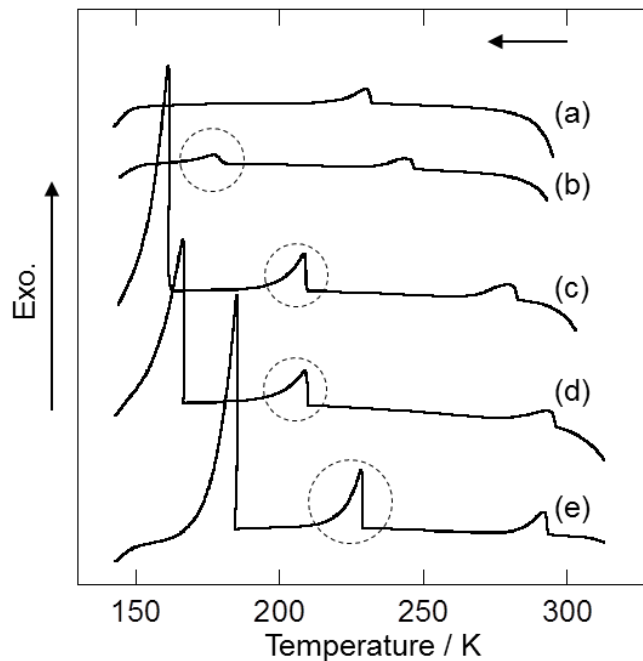
Figure 4–11. Differential scanning calorimetric curves in the cooling process for EMPyr(FH)$_n$F in the range of $1.9 \leq n \leq 2.3$; (a) 2.3, (b) 2.2, (c) 2.1, (d) 2.0, and (e) 1.9. The dotted circles denote the exothermic peaks of the phase transition from IPC (I) to IPC (II).

Figure 4–12. X-ray diffraction patterns of EMPyr(FH)$_n$F; (a) $n = 1.9$ at 213 K, (b) $n = 2.0$ at 183 K, and (c) $n = 2.1$ at 183 K. The sample was cooled from room temperature to the target temperature as in the case of DSC in Figure 4–11.
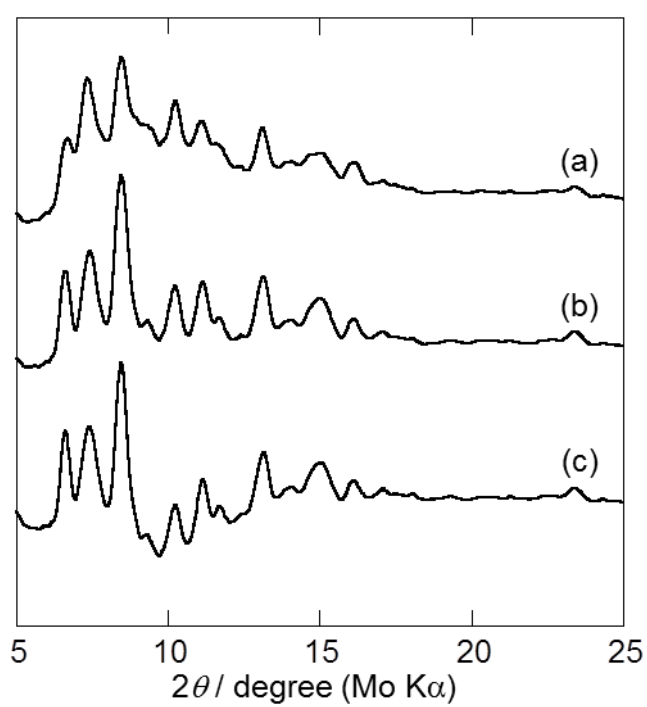
Figure 4–13. X-ray diffraction patterns of EMPyr(FH)$_n$F in the range of $1.0 \leq n \leq 1.2$ at 243 K; (a) 1.0, (b) 1.1, and (c) 1.2.
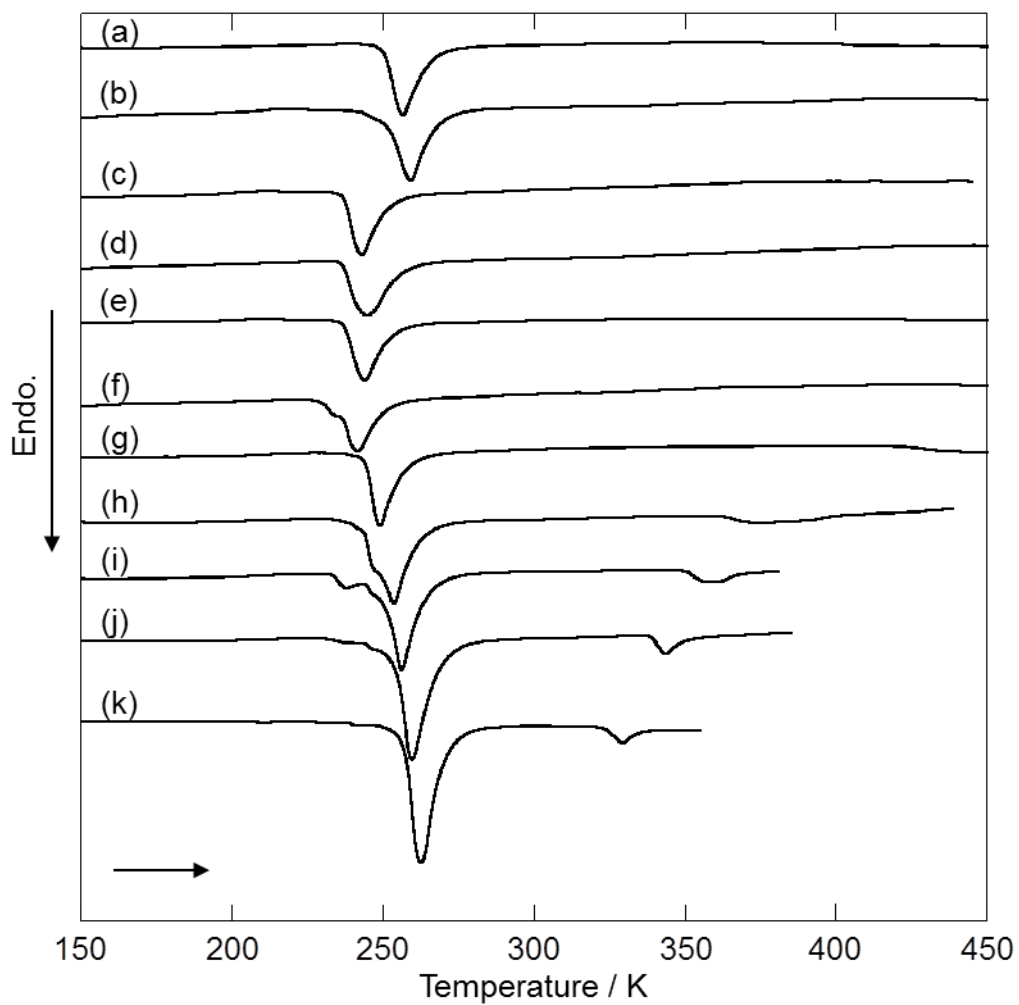
Figure 4–14. Differential scanning calorimetric curves for DMPyr(FH)$_n$F in the range of $1.0 \leq n \leq 2.0$; (a) 1.0, (b)1.1, (c) 1.2, (d) 1.3, (e) 1.4, (f) 1.5, (g) 1.6, (h) 1.7, (i) 1.8, (j) 1.9, and (k) 2.0.
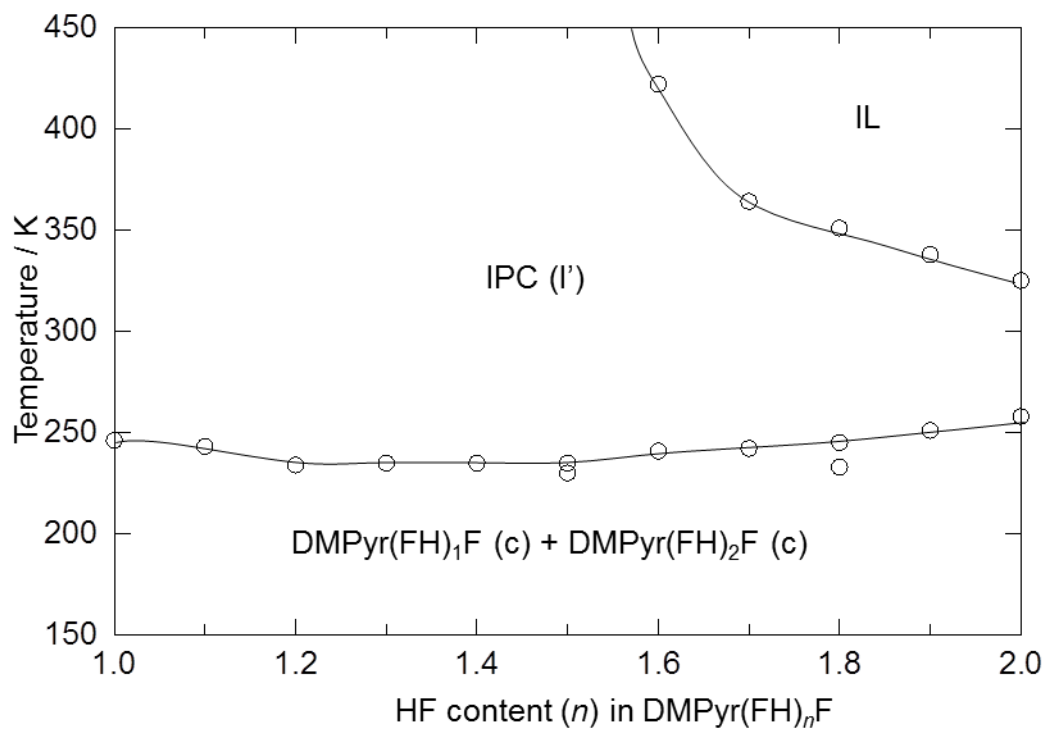
Figure 4–15. Plot of the DSC transitions for the $DMPyr(FH)_nF$ system. IL, ionic liquid phase; IPC (I'), ionic plastic crystal phase (I'); $DMPyr(FH)_1F$ (c), crystal phase of $DMPyr(FH)_1F$; $DMPyr(FH)_2F$ (c), crystal phase of $DMPyr(FH)_2F$.
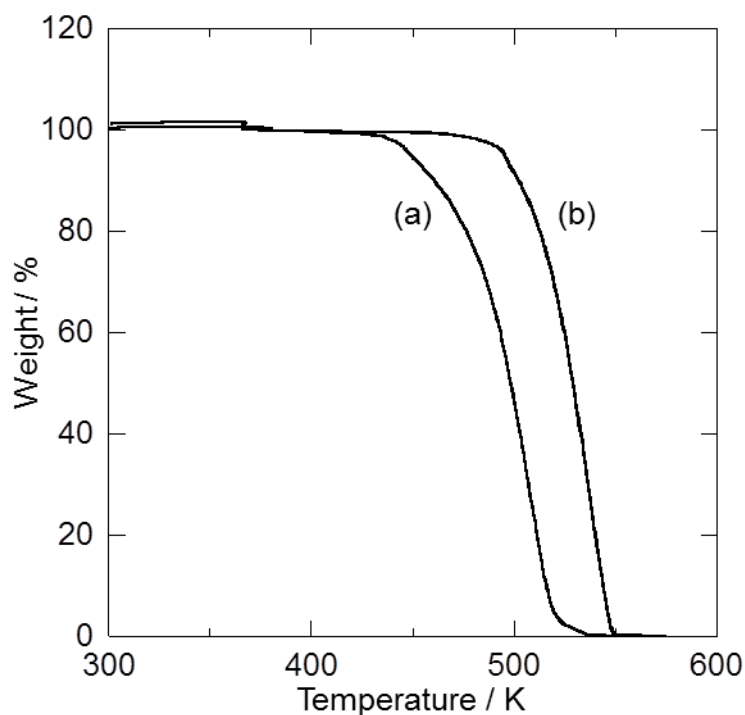

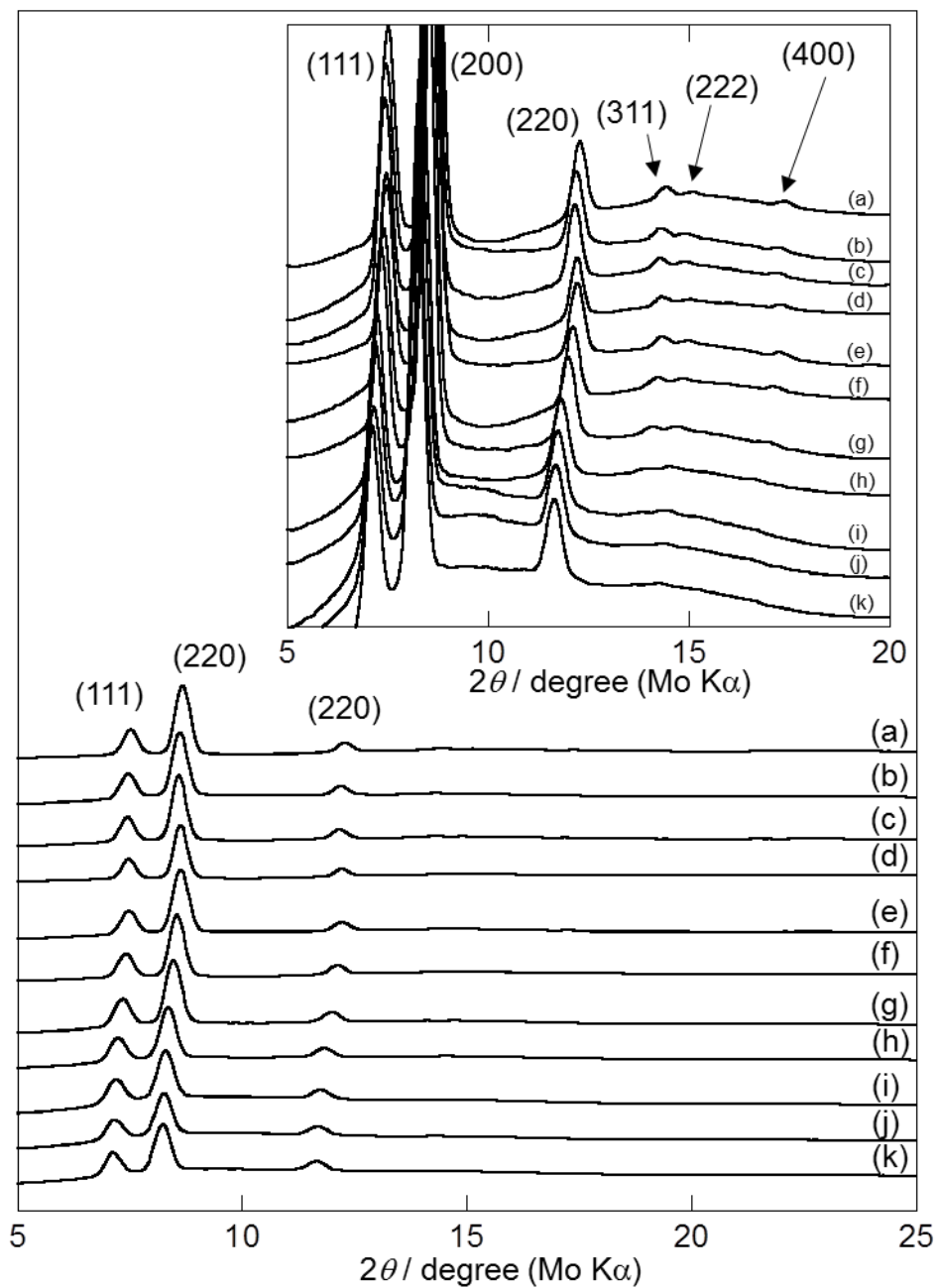Figure 4–16. Thermogravimetric curves of (a) $EMPyr(FH)_{1.0}F$ and (b) $DMPyr(FH)_{1.0}F$.

Figure 4–17. X-ray diffraction patterns of DMPyr(FH)$_n$F in the range of $1.0 \leq n \leq 2.0$ at 298 K; (a) 1.0, (b)1.1, (c) 1.2, (d) 1.3, (e) 1.4, (f) 1.5, (g) 1.6, (h) 1.7, (i) 1.8, (j) 1.9, and (k) 2.0.
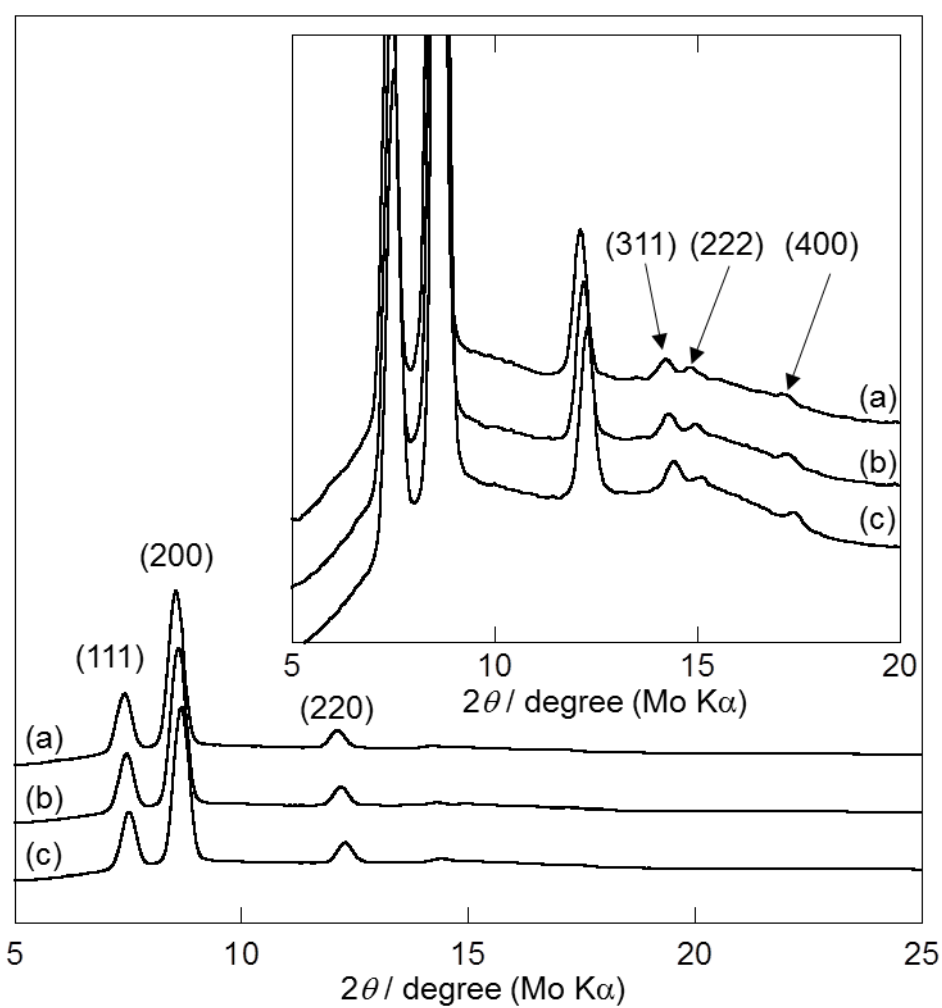
Figure 4–18. X-ray diffraction patterns of DMPyr(FH)$_{1.0}$F at (a) 443 K, (b) 373 K, and (c) 298 K.
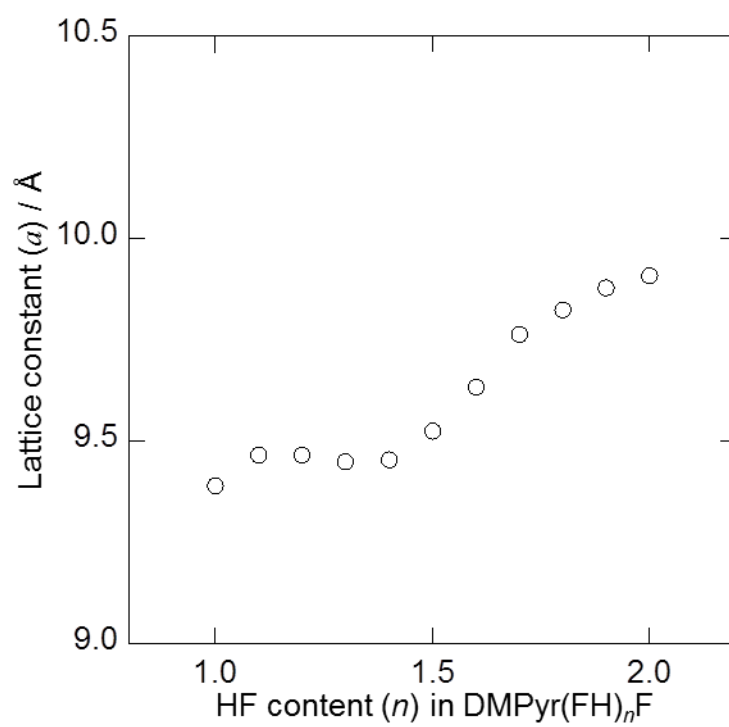
Figure 4–19. The lattice constant (*a*) of the IPC (I') of DMPyr(FH)$_n$F ($1.0 \leq n \leq 2.0$) at 298 K.
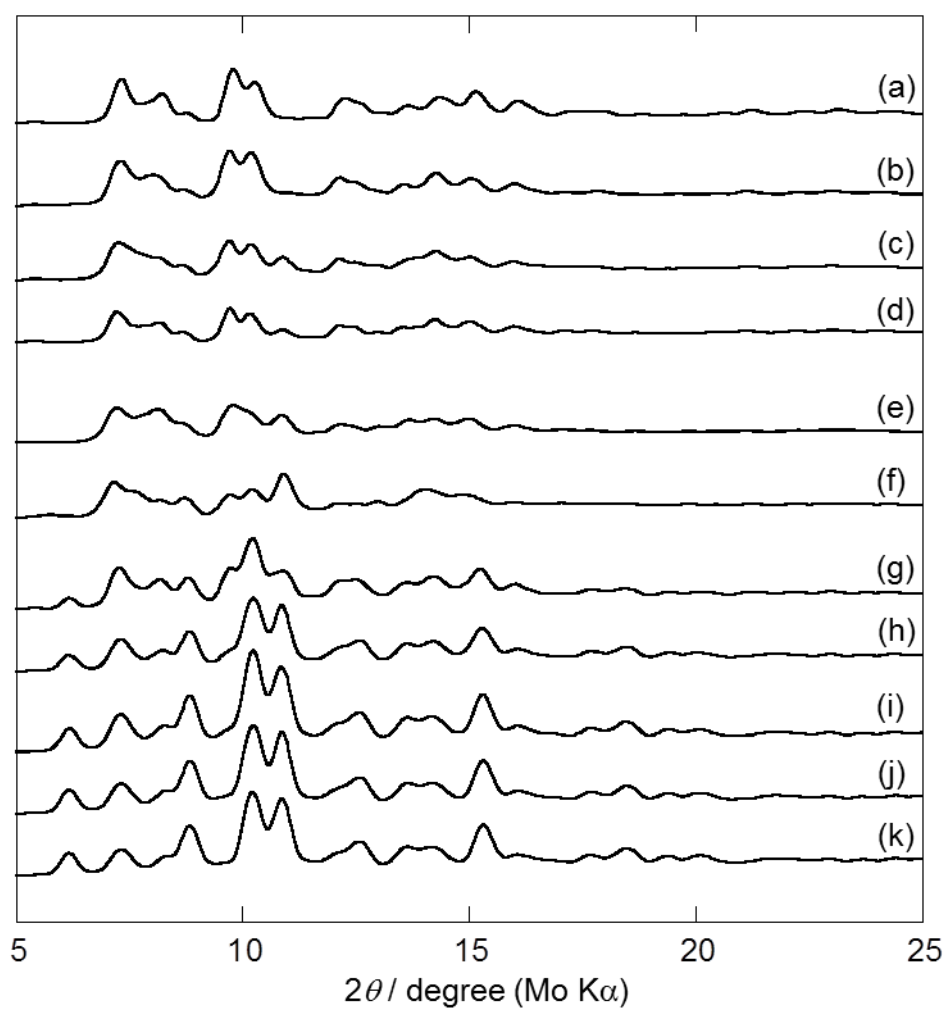
Figure 4–20. X-ray diffraction patterns of DMPyr(FH)$_n$F in the range of $1.0 \leq n \leq 2.0$ at 203 K; (a) 1.0, (b)1.1, (c) 1.2, (d) 1.3, (e) 1.4, (f) 1.5, (g) 1.6, (h) 1.7, (i) 1.8, (j) 1.9, and (k) 2.0.

Chapter 5

Fluorohydrogenate salts based on azoniaspiro-type cations

5.1 Introduction

The AS[*x,y*]$^+$ cations (AS[*x,y*]$^+$, *x* and *y* denote the number of carbon atoms in each cyclic group in the azoniaspiro-type cation) are aliphatic and have no terminal alkyl group in contrast to tetraalkylammonium cation, dialkylpyrrolidinium cation, and dialkylpiperidinium cation. A series of derivatives were synthesized as the heterocyclic azoniaspiro ring systems [1–3]. The difference in flexibility between non-cyclic alkyl side-chains and cyclic methylene groups gives some effects on their solution properties [4–8]. The two closed rings in AS[*x,y*]$^+$ cations alter their thermodynamic properties and weaken their hydrophobic interactions with water, where the shapes of AS[*x,y*]$^+$ cations have a substantial effect to decrease the dielectric relaxation time of water surrounding the cations [4–7]. The methylene groups in the rings are tightly connected together to restrict their movement and the charged nitrogen atom in AS[*x,y*]$^+$ cations is more exposed to the solvent than that of ammonium cations with the terminal methyl group [4–7].

The AS[*x,y*]$^+$ salts have attracted attentions as favorable electrolytes for electric double-layer capacitors (EDLC) [9–12]. The organic solution of AS[4.4]$^+$ (5-azoniaspiro[4.4]nonane cation) salt exhibits a higher conductivity than those of ammonium salts with terminal alkyl group [10–12]. Another notable characteristic of AS[4.4]$^+$ cation is its large solubility into organic solvents. The respective solubilities of AS[4.4]BF$_4$, methyltriethylammonium tetrafluoroborate (N$_{1222}$BF$_4$), and tetraethylammonium tetrafluoroborate (N$_{2222}$BF$_4$) at 303 K are 3.55, 2.21, and 1.10 mol dm^{-3} to propylenecarbonate (PC), and are 2.13, 0.04, < 0.01 mol dm^{-3} to dimethylcarbonate (DMC) [10,11]. The AS[4.4]$^+$

based electrolytes exhibit low viscosity and high capacitance, especially at low temperature [10,11]. At room temperature, there is no difference in viscosity for 1.0 mol dm^{-3} AS[4.4]BF$_4$/PC, N$_{1222}$BF$_4$/PC, and N$_{2222}$BF$_4$/PC, whereas the capacitance of EDLC utilizing AS[4.4]BF$_4$/PC at high discharging rates is higher than those of N$_{1222}$BF$_4$/PC and N$_{2222}$BF$_4$/PC. This behavior indicates the mobility of AS[4.4]$^+$ cation in the electrolyte in the pores of activated carbon is higher than those due to the small size and rigidity of the structure as in the case of the water solution of AS[4.4]$^+$ salts.

The AS[4.4]$^+$ cation adopts two conformations for the ring composed of one nitrogen and four carbons, envelope and twist as shown in Figure 5–1. The quantum chemical calculations of AS[4.4]$^+$ cation showed that an envelope–envelope (C_2-symmetry) conformation is more stable than a twist–twist (D_2-symmetry) conformation in vacuum by 13 kJ mol^{-1} [13]. Combination of the Raman spectroscopic study and density functional theory calculations for AS[4.4]BF$_4$ in DMC suggested that two rings of AS[4.4]$^+$ in DMC are in the N-flapped envelope (i.e., the four carbon atoms are on the same plane) conformation and that the C-flapped envelope (i.e., the nitrogen and three of the four carbon atoms are on the same plane) conformation has slightly lower stability about 2 kJ mol^{-1} [14].

Most of the AS[4.4]$^+$ salts have high melting points (T_m); 387 K for AS[4.4]N(SO$_2$CF$_3$)$_2$, 468 K for AS[4.4]N(SO$_2$F)$_2$, and 462 K for AS[4.4]BF$_4$ [15,16]. Only the RTIL based on AS[4.4]$^+$ known today is AS[4.4]N(SO$_2$CF$_3$)(SO$_2$F) (T_m: 294 K) [15]. Decrease in melting point was realized by two methods; substitution of carbon atom with oxygen atom in the ring without lowering the electrochemical stability, and introduction of alkyl groups in the ring leading to incorporation of asymmetry, although their thermal stability is lowered [16]. Development of low melting salts without sacrificing other preferable properties is required and the use of fluorohydrogenate anions as counterion is an interesting method to lower melting point. Chapter 5 reports synthesis and characterization of new FHILs based on

AS[x,y]$^+$ cations such as AS[4.4]$^+$, 5-azoniaspiro[4.5]decane cation (AS[4.5]$^+$), 6-azoniaspiro[5.5]undecane cation (AS[5.5]$^+$), 8-oxa-5-azoniaspiro[4.5]decane cation (AS[4.2O2]$^+$), 9-oxa-6-azoniaspiro[5.5]undecane cation (AS[5.2O2]$^+$), and 3,9-dioxa-6-azoniaspiro[5.5]undecane cation (AS[2O2.2O2]$^+$). In order to compare the effects of the cyclic structure with linear alkyl side-chain, fluorohydrogenate salts with N$_{2222}$$^+$ and diethylpyrrolidinium cation (DEPyr$^+$) were synthesized and characterized. Effects of the number of carbon atoms and introduction of oxygen atom in the azoniaspiro-type cations on their physicochemical properties are discussed.

5.2 Experimental

Bromide salts of AS[x,y]$^+$ cations, summarized in Table 2–1, were synthesized by the reaction of the corresponding amine and dihaloalkane. The following is the typical procedure for AS[4.4]Br (Scheme 5–1). Pyrrolidine and K$_2$CO$_3$ were mixed in acetonitrile in a glass flask under the argon atmosphere in a glove bag. After 1,4-dibromobutane was added to the flask in drop at 273 K, the flask was connected to a reflux apparatus and stirred at 333 K for 6 hours. First filtration of the contents in the flask removed K$_2$CO$_3$ mostly. Addition of ethyl acetate to the filtrate resulted in recrystallization of AS[4.4]Br, followed by drying under vacuum at 333 K for 1 day. The remaining K$_2$CO$_3$ was completely removed by passing the acetonitrile solution of AS[4.4]Br through an activated alumina column (mean diameter of the activated alumina: 75 μm). The above-mentioned recrystallization and washing procedure was repeated several times, followed by drying under vacuum at 353 K. In the case of AS[5.2O2]Br, ethanol was used instead of acetonitrile for column chromatography and purification. The DEPyrBr salt was synthesized by the reaction of *N*-ethylpyrrolidine and bromoethane in the following procedure. Bromoethane was dropped onto the acetonitrile solution of *N*-methylpyrrolidine at 273 K under argon atmosphere in a glove bag. The mixture

was stirred at 298 K under an airtight condition for two days. The purification of DEPyrBr was performed as the same manner for EMPyrCl in Chapter 3. All the bromides were obtained as white powdery samples. The results of elemental analysis for the obtained bromides are summarized below. AS[4.4]Br; Anal. Calcd. for C8H16N1Br1: C, 46.62; H, 7.77; N, 6.80; Br, 38.81. Found: C, 46.43; H, 7.71; N, 6.76; Br, 38.73. AS[4.5]Br; Anal. Calcd. for C9H18N1Br1: C, 49.11; H, 8.19; N, 6.37; Br, 36.33. Found: C, 48.96; H, 8.29; N, 6.42; Br, 36.45. AS[5.5]Br; Anal. Calcd. for C10H20N1Br1: C, 51.30; H, 8.55; N, 5.99; Br, 34.16. Found: C, 56.08; H, 8.56; N, 6.12; Br, 33.99. AS[4.2O2]Br; Anal. Calcd. for C8H16N1O1Br1: C, 43.26; H, 7.21; N, 6.31; O, 7.21; Br, 36.01. Found: C, 43.05; H, 7.20; N, 6.42; O, 7.31; Br, 35.88. AS[5.2O2]Br; Anal. Calcd. for C9H18N1O1Br1: C, 45.78; H, 7.63; N, 5.93; O, 6.78; Br, 33.87. Found: C, 45.72; H, 7.79; N, 5.90; O, 6.94; Br, 33.95. AS[2O2.2O2]Br; Anal. Calcd. for C8H16N1O2Br1: C, 40.35; H, 6.73; N, 5.88; O, 13.45; Br, 33.59. Found: C, 39.99; H, 6.80; N, 5.85; O, 13.67; Br, 33.57. DEPyrBr; Anal. Calcd. for C8H18N1Br1: C, 46.18; H, 8.66; N, 6.73; Br, 38.43. Found: C, 46.01; H, 8.71; N, 6.80; Br, 38.26.
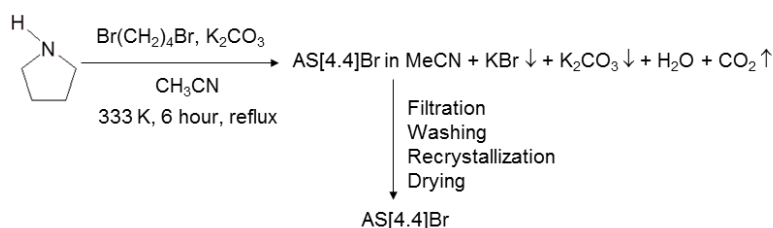
Scheme 5–1

Fluorohydrogenate salts based on azoniaspiro-type cations, $AS[x,y](FH)_nF$, $DEPyr(FH)_{2.0}F$, and $N_{2222}(FH)_{2.3}F$, were prepared by the reaction of a large excess of aHF and corresponding bromides or $N_{2222}Cl$ at 298 K as described in Chapter 2. The $N_{2222}(FH)_{2.3}F$ salt was heated at 323 K under vacuum to adjust the HF content to 2.0. The HF contents in the present fluorohydrogenate salts, $AS[4.4](FH)_{2.0}F$, $AS[4.5](FH)_{2.0}F$, $AS[5.5](FH)_{2.0}F$, $AS[4.2O2](FH)_{1.9}F$, $AS[5.2O2](FH)_{2.0}F$, $AS[2O2.2O2](FH)_{2.0}F$, $DEPyr(FH)_{2.0}F$, and

$N_{2222}(FH)_{2.0}F$, were checked by weight change and neutralization titration using an aqueous NaOH solution. Testing for the presence of residual Cl^- or Br^- with a 1M aqueous $AgNO_3$ solution gave no precipitation of silver halides. The $(FH)_2F^-$ anion were identified by IR spectroscopy (Figure 5–2). $AS[4.4](FH)_{2.0}F$; IR (AgCl): ν = 2332 (m), 1993 (m), 1800 (s), 1026 (w) cm^{-1}, $AS[4.5](FH)_{2.0}F$; IR (AgCl): ν = 2329 (m), 1993 (m), 1804 (s), 1026 (w) cm^{-1}, $AS[5.5](FH)_{2.0}F$; IR (AgCl): ν = 2329 (m), 1991 (m), 1806 (s), 1026 (w) cm^{-1}, $AS[4.2O2](FH)_{1.9}F$; IR (AgCl): ν = 2332 (m), 1989 (m), 1804 (s), 1021 (w) cm^{-1}, $AS[5.2O2](FH)_{2.0}F$; IR (AgCl): ν = 2329 (m), 1956 (m), 1773 (s), 1026(w) cm^{-1}, $AS[2O2.2O2](FH)_{2.0}F$; IR (AgCl): ν = 2338 (m), 1983 (m), 1807 (s), 1017 (w) cm^{-1}, $DEPyr(FH)_{2.0}F$; IR (AgCl): ν = 2329 (m), 2004 (m), 1796 (s), 1019 (w) cm^{-1}, and $N_{2222}(FH)_{2.0}F$; IR (AgCl): ν = 2329 (m), 2018 (m), 1815 (s), 1000 (w) cm^{-1}.

5.3 Results and discussion

5.3.1 Thermal stability

Figure 5–3 shows the TG curves of $AS[4.4](FH)_{2.0}F$, $DEPyr(FH)_{2.0}F$, and $N_{2222}(FH)_{2.0}F$. Thermal stability increases in the order of $AS[4.4](FH)_{2.0}F > DEPyr(FH)_{2.0}F > N_{2222}(FH)_{2.0}F$ as shown in Figure 5–4 (a). The increase in the number of the ring structure in cations raises the thermal stability. Figure 5–5 shows the TG curves of $AS[4.4](FH)_{2.0}F$, $AS[4.5](FH)_{2.0}F$, $AS[5.5](FH)_{2.0}F$, $AS[4.2O2](FH)_{1.9}F$, $AS[5.2O2](FH)_{2.0}F$, and $AS[2O2.2O2](FH)_{2.0}F$. The order of the thermal stability for these fluorohydrogenate salts is summarized in Figure 5–4 (b). The increase in the number of carbon atoms in the ring from 4 to 5 slightly lowers the thermal stability; $AS[4.4](FH)_{2.0}F > AS[4.5](FH)_{2.0}F \approx AS[5.5](FH)_{2.0}F$. The similar thermal stabilities of $AS[4.5](FH)_{2.0}F$ and $AS[5.5](FH)_{2.0}F$ show that the asymmetric structure does not affect the pyrolysis. The $AS[x.y](FH)_nF$ salts without oxygen atom in the ring have higher thermal stability than those with oxygen atom, indicating the introduction of oxygen in the

ring reduces thermal stability.

5.3.2 Phase behavior

Figure 5–6 shows the DSC curves of AS[4.4](FH)$_{2.0}$F, DEPyr(FH)$_{2.0}$F, and N$_{2222}$(FH)$_{2.0}$F. Melting point decreases in the order of N$_{2222}$(FH)$_{2.0}$F (413 K) > DEPyr(FH)$_{2.0}$F (358 K) > AS[4.4](FH)$_{2.0}$F (271 K), and in particular AS[4.4](FH)$_{2.0}$F has the lowest melting point in FHILs composed of (FH)$_{2.0}$F$^-$ and aliphatic cations [DMPyr(FH)$_{2.0}$F (323 K) and EMPyr(FH)$_{2.0}$F (303 K)], as shown in Figure 5–7. The existence of the ring structure lowers melting point in the case of fluorohydrogenate salts as known for tetrafluoroborate salts (N$_{2222}$BF$_4$ (642 K) and AS[4.4]BF$_4$ (387 K)) [15,17]. This trend is in contrast to sulfonylamide salts, N$_{2222}$N(SO$_2$CF$_3$)$_2$ (369 K), AS[4.4]N(SO$_2$CF$_3$)$_2$ (387 K), N$_{2222}$N(SO$_2$F)$_2$ (313 K), AS[4.4]N(SO$_2$F)$_2$ (468 K), N$_{2222}$N(SO$_2$CF$_3$)SO$_2$F (281 K), and AS[4.4]N(SO$_2$CF$_3$)SO$_2$F (294 K) [15].

Figure 5–8 shows XRD patterns of the solid phases below melting point for AS[4.4](FH)$_{2.0}$F, DEPyr(FH)$_{2.0}$F, and N$_{2222}$(FH)$_{2.0}$F. Only three diffraction peaks were observed in the low 2θ-angle region and can be indexed with the indices (111), (200), and (220). This structural behavior indicates these salts form IPC phases at the highest temperature region in the solid phase (248 – 271 K, 233 – 358 K, and 308 – 413 K for AS[4.4](FH)$_{2.0}$F, DEPyr(FH)$_{2.0}$F, and N$_{2222}$(FH)$_{2.0}$F, respectively) with the NaCl-type lattice as in the cases of DMPyr(FH)$_{2.0}$F and EMPyr(FH)$_{2.0}$F in Chapter 3. The lattice constant a for the cubic structure reflects the size of the cation; 10.18 Å for AS[4.4](FH)$_{2.0}$F, 10.53 Å DEPyr(FH)$_{2.0}$F, and 10.72 Å N$_{2222}$(FH)$_{2.0}$F.

Figure 5–9 shows the DSC curves of AS[4.4](FH)$_{2.0}$F, AS[4.5](FH)$_{2.0}$F, AS[5.5](FH)$_{2.0}$F, AS[4.2O2](FH)$_{1.9}$F, AS[5.2O2](FH)$_{2.0}$F, and AS[2O2.2O2](FH)$_{2.0}$F. The asymmetric effect of AS[4.5]$^+$ on lowering melting point is not observed and the decrease in the number of carbon

atoms decreases melting point (Figure 5−10); AS[4.4](FH)$_{2.0}$F (271 K) < AS[4.5](FH)$_{2.0}$F (329 K) < AS[5.5](FH)$_{2.0}$F (385 K). Introduction of oxygen atom to azoniaspiro cations lowers the melting point (Figure 5−10); AS[4.2O2](FH)$_{1.9}$F (256 K) < AS[4.5](FH)$_{2.0}$F and AS[5.2O2](FH)$_{2.0}$F (313 K) < AS[2O2.2O2](FH)$_{2.0}$F (358 K) < AS[5.5](FH)$_{2.0}$F. In the present series of fluorohydrogenate salts, only two salts (AS[4.4](FH)$_{2.0}$F and AS[4.2O2](FH)$_{1.9}$F) exhibit melting points below room temperature, although all the salts have the lowest among the known salts with the same cations.

5.3.3 Physicochemical properties

Table 5−1 summarizes physicochemical properties of the present salts. For two RTILs (AS[4.4](FH)$_{2.0}$F and AS[4.2O2](FH)$_{1.9}$F), density at 298 K, viscosity, ionic conductivity, and electrochemical stability on a vitreous carbon electrode were measured. Figure 5−11 show Arrhenius plots of viscosity and ionic conductivity for AS[4.4](FH)$_{2.0}$F and AS[4.2O2](FH)$_{1.9}$F. The activation energies of viscosity and ionic conductivity are 18.5 and 11.3 kJ mol^{-1} for AS[4.4](FH)$_{2.0}$F, respectively, and 28.3 and 21.9 kJ mol^{-1} for AS[4.2O2](FH)$_{1.9}$F, respectively. The higher activation energies of AS[4.2O2](FH)$_{1.9}$F than those of AS[4.4](FH)$_{2.0}$F may be caused by the large number of ring number and the existence of oxygen atom. Figure 5−12 shows linear sweep voltammograms of AS[4.4](FH)$_{2.0}$F and AS[4.2O2](FH)$_{1.9}$F when a vitreous carbon electrode was used as a working electrode. The anode and cathode limit potentials are determined when the absolute value of the current density exceeds 0.5 mA cm^{-2} at a scan rate of 10 mV s^{-1}. Electrochemical windows of AS[4.4](FH)$_{2.0}$F and AS[4.2O2](FH)$_{1.9}$F range between −2.59 and +2.92 V vs. Fc$^+$/Fc and between −2.71 and +2.71 V vs. Fc$^+$/Fc. Compared to other FHILs based on aliphatic cations [21,22], FHILs based on azoniaspiro-type cations exhibit wider electrochemical windows on a vitreous carbon electrode and higher ionic conductivity as summarized in Table 5−1.

References

[1] F. F.Blicke, E. B. Hotelling, *J. Am. Chem. Soc*. **1954**, *76*, 5099.

[2] B. C. Cossar, D.D. Reynolds, *J. Heterocycl. Chem.* **1965**, *2*, 430.

[3] A. Siggel, F. Nerenz, T. Palanisamy, A. Poss, S. Demel, U. S. Patent **2007**, 0049750 A1.

[4] D. P. Wilson, W.-Y. Wen, *J. Phys. Chem.* **1975**, *79*, 1527.

[5] W.-Y. Wen, A. LoSurdo, C. Jolicoeur, J. Boileau, *J. Phys. Chem*. **1976**, *80*, 466.

[6] W.-Y. Wen, U. Kaatze, *J. Phys. Chem*. **1977**, *81*, 177.

[7] A. LoSurdo, W.-Y. Wen, C. Jolicoeur, J.-L. Fortier, *J. Phys. Chem.* **1977**, *81*, 1813.

[8] G. Somsen, *Pure Appl. Chem.* **1993**, *65*, 983.

[9] M. Ue, K. Ida, S. Mori, *J. Electrochem. Soc.* **1994**, *141*, 2989.

[10] K. Chiba, T. Ueda, H. Yamamoto, *Electrochemistry* **2007**, *75*, 664.

[11] K. Chiba, T. Ueda, H. Yamamoto, *Electrochemistry* **2007**, *75*, 668.

[12] T. Devarajan, S. Higashiya, C. Dangler, M. Rane-Fondacaro, J. Snyder, P. Haldar, *Electrochem. Commun.* **2009**, *11*, 680.

[13] U. Monkowius, S. Nogai, H. Schmidbaur, *Z. Naturforsh., B: Chem. Sci*. **2004**, *59*, 259.

[14] T. Sukizaki, S. Fukuda, T. Yamaguchi, K. Fujii, R. Kanzaki, K. Chiba, H. Yamamoto, Y. Umebayashi, S. Ishiguro, *Electrochemistry* **2007**, *75*, 628.

[15] H. Matsumoto, N. Terasawa, H. Sakaebe, S. Tsuzuki, U. S. Patent **2011**, 0070486 A1.

[16] S. Higashiya, T. S. Devarajan, M. V. Rane-Fondacaro, C. Dangler, J. Snyder, P. Haldar, *Helv. Chim. Acta* **2009**, *92*, 1600.

[17] G. Zabinska, P. Ferloni, M. Sanesi, *Thermochim. Acta* **1987**, *122*, 87.

[18] R. Hagiwara, K. Matsumoto, Y. Nakamori, T. Tsuda, Y. Ito, H. Matsumoto, K. Momota, *J. Electrochem. Soc.* **2003**, *150*, D195.

[19] K. Matsumoto, R. Hagiwara, Y. Ito, *Electrochem. Solid-State Lett*. **2004**, *7*, E41.

Table 5–1. Physicochemical properties of present and selected fluorohydrogenate salts.

	FW	T_m / K	ρ / g cm^{-3}	η / cP	σ / mS cm^{-1}	E_{ca} / V	E_{an} / V	Ref.
N$_{2222}$(FH)$_{2.0}$F	189	413	–	–	–	–	–	This work
DEPyr(FH)$_{2.0}$F	187	358	–	–	–	–	–	This work
AS[4.4](FH)$_{2.0}$F	185	271	1.13	16.2	82.1	–2.59	+2.92	This work
AS[4.5](FH)$_{2.0}$F	199	320	–	–	–	–	–	This work
AS[5.5](FH)$_{2.0}$F	213	385	–	–	–	–	–	This work
AS[4.2O2](FH)$_{1.9}$F	199	256	1.21	63.6	24.6	–2.71	+2.71	This work
AS[5.2O2](FH)$_{2.0}$F	215	313	–	–	–	–	–	This work
AS[2O2.2O2](FH)$_{2.0}$F	217	358	–	–	–	–	–	This work
EMIm(FH)$_{2.3}$F	176	208	1.13	4.9	100	–1.83	+1.26	[18]
EMPyr(FH)$_{2.3}$F	179	239	1.07	11.5	74.6	–1.99	+2.67	[19]
PMPyr(FH)$_{2.3}$F	193	–	1.05	13.0	58.1	–2.56	+2.78	[19]
BMPyr(FH)$_{2.3}$F	207	–	1.04	6	35.9	–2.33	+2.38	[19]
EMPip(FH)$_{2.3}$F	193	237	1.07	21.9	37.2	–2.33	+2.81	[19]
PMPip(FH)$_{2.3}$F	207	–	1.06	27.4	23.9	–2.35	+2.87	[19]
BMPip(FH)$_{2.3}$F	221	–	1.04	34.4	12.3	–2.81	+2.52	[19]

Fw: formula weight, T_m: melting point, ρ: density at 298 K, η: viscosity at 298 K, σ: conductivity at 298 K, E_{ca} and E_{an}: cathode and anode limit potentials (V vs. Fc$^+$/Fc) on a vitreous carbon electrode.
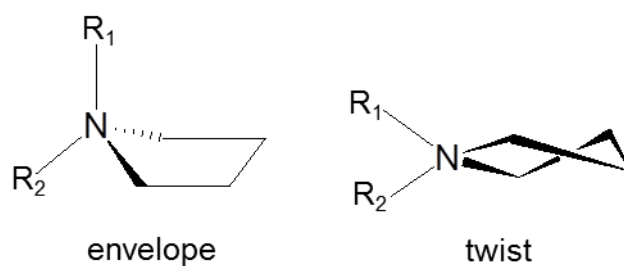
Figure 5–1. Schematic illustration of the envelope and twist conformers of pyrrolidinium ring.
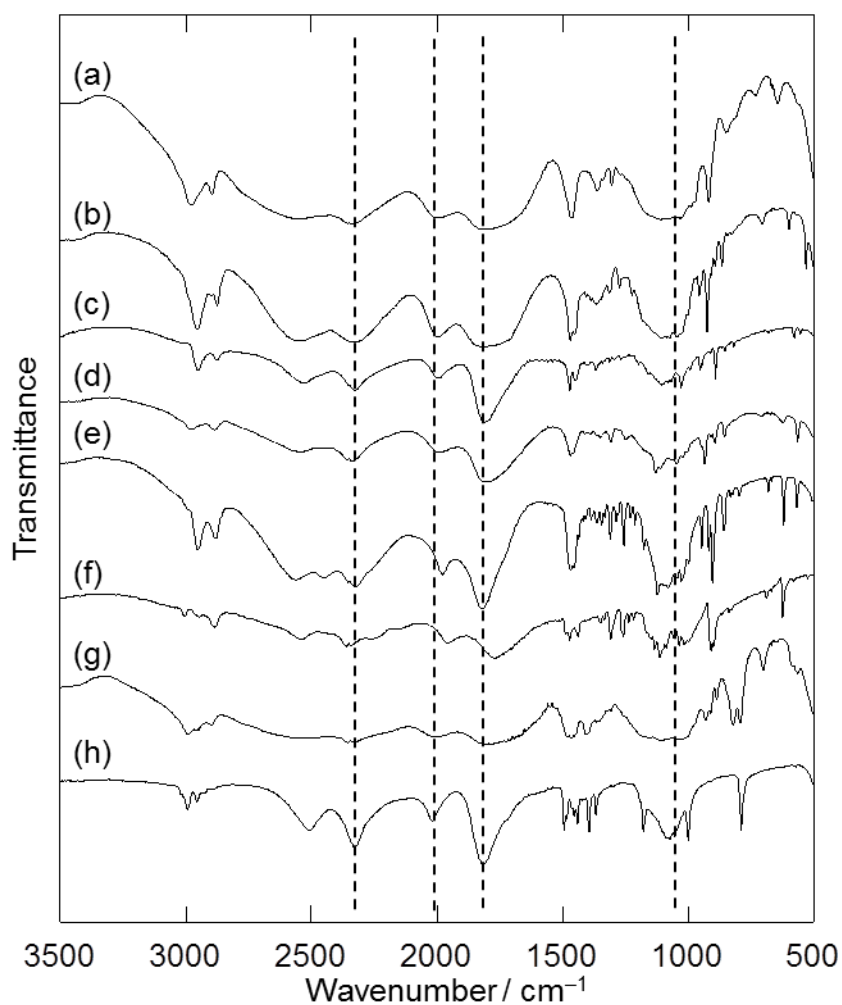

Figure 5–2. Infrared spectra for (a) AS[4.4](FH)$_{2.0}$F, (b) AS[4.5](FH)$_{2.0}$F, (c) AS[5.5](FH)$_{2.0}$F, (d) AS[4.2O2](FH)$_{1.9}$F, (e) AS[5.2O2](FH)$_{2.0}$F, (f) AS[2O2.2O2](FH)$_{2.0}$F, (g) DEPyr(FH)$_{2.0}$F, and (h) N$_{2222}$(FH)$_{2.0}$F. The dotted lines denote the positions where the absorption bands of (FH)$_2$F$^-$ are observed.
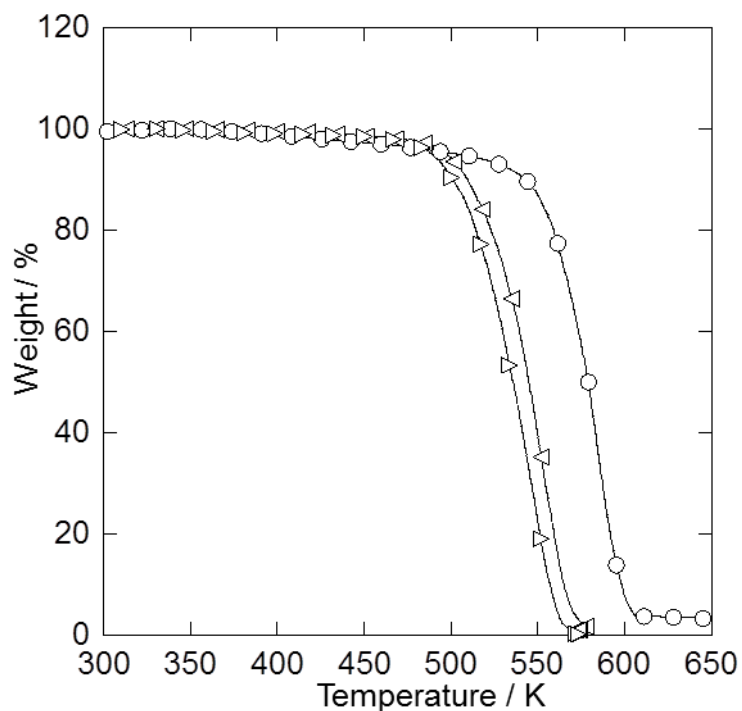
Figure 5–3. Thermogravimetric curves for (○) AS[4.4](FH)$_{2.0}$F, (◁) DEPyr(FH)$_{2.0}$F, and (▷) N$_{2222}$(FH)$_{2.0}$F. Scan rate: 10 K min^{-1}.
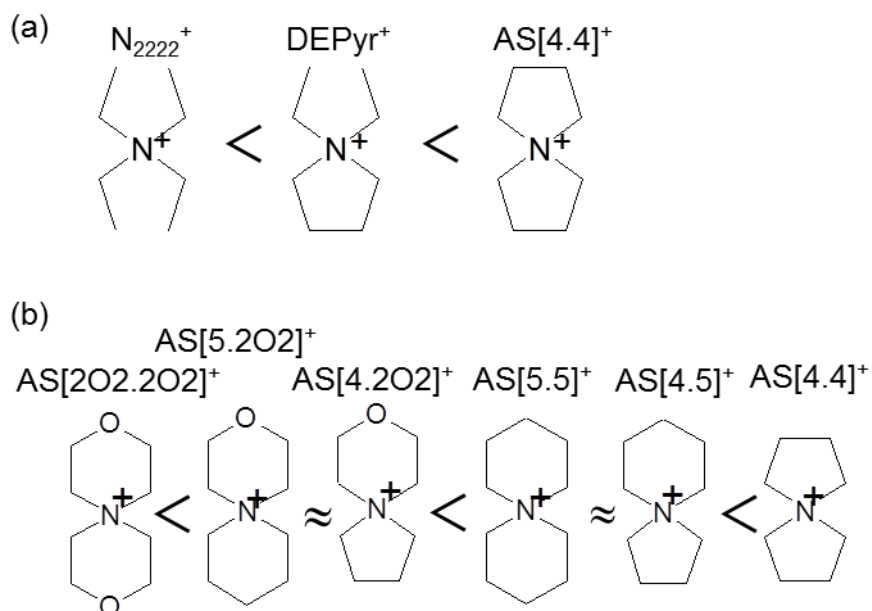
Figure 5–4. The order of thermal stability for fluorohydrogenate salts based on aliphatic cations, showing the effects of (a) the ring structure and (b) the number of carbon and oxygen atoms.
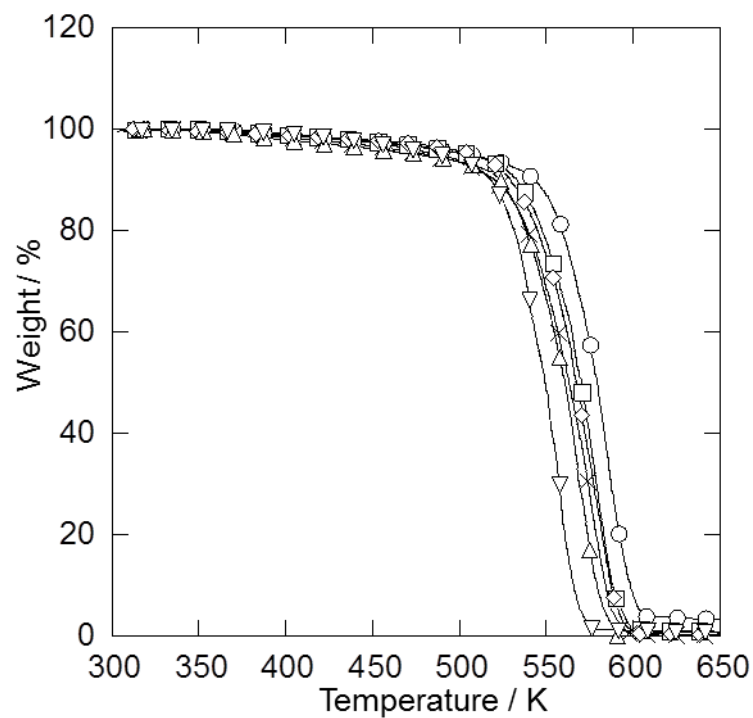
Figure 5–5. Thermogravimetric curves for ($\circ$) AS[4.4](FH)$_{2.0}$F, ($\square$) AS[4.5](FH)$_{2.0}$F, ($\diamond$) AS[5.5](FH)$_{2.0}$F, ($\times$) AS[4.2O2](FH)$_{1.9}$F, ($\triangle$) AS[5.2O2](FH)$_{2.0}$F, and ($\triangledown$) AS[2O2.2O2](FH)$_{2.0}$F. Scan rate: 10 K min^{-1}.
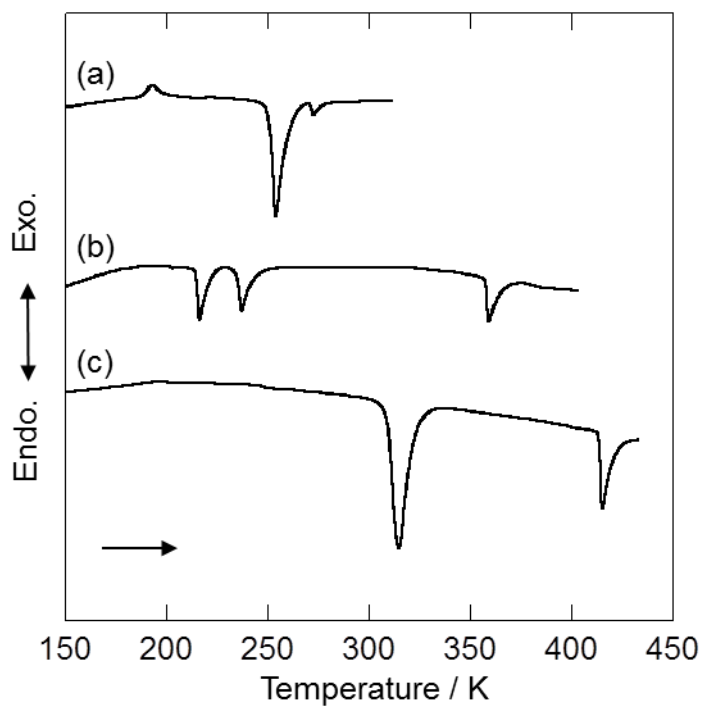
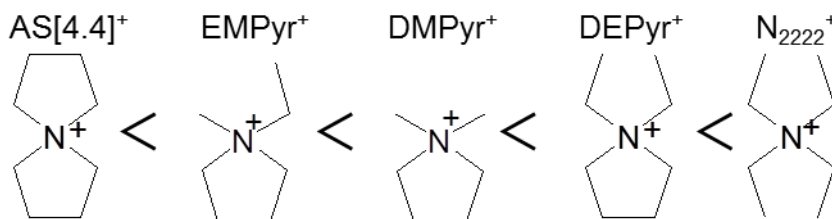Figure 5–6. Differential scanning calorimetric curves (a) AS[4.4](FH)$_{2.0}$F, (b) DEPyr(FH)$_{2.0}$F, and (c) N$_{2222}$(FH)$_{2.0}$F.

Figure 5–7. The order of melting point for fluorohydrogenate salts based on aliphatic cations, showing the effect of the side-chain.
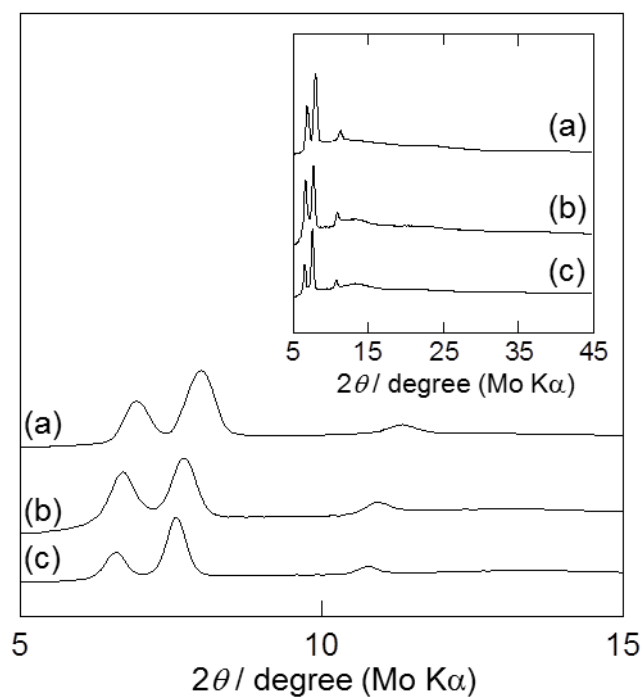

Figure 5–8. X-ray diffraction patterns of the IPC phase for (a) AS[4.4](FH)$_{2.0}$F at 253 K, (b) DEPyr(FH)$_{2.0}$F at 313 K, and (c) N$_{2222}$(FH)$_{2.0}$F at 313 K.
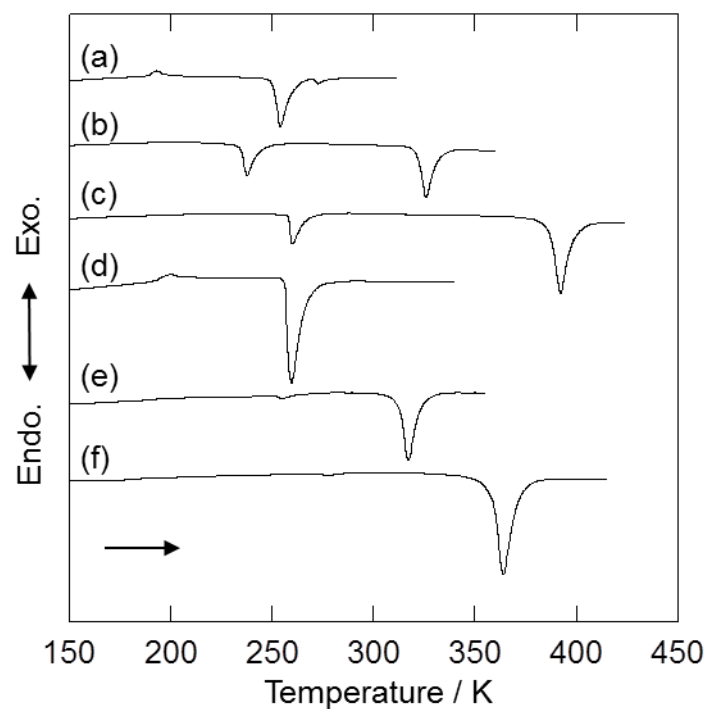
Figure 5–9. Differential scanning calorimetric curves (a) AS[4.4](FH)$_{2.0}$F, (b) AS[4.5](FH)$_{2.0}$F, (c) AS[5.5](FH)$_{2.0}$F, (d) AS[4.2O2](FH)$_{1.9}$F, (e) AS[5.2O2](FH)$_{2.0}$F, and (f) AS[2O2.2O2](FH)$_{2.0}$F.
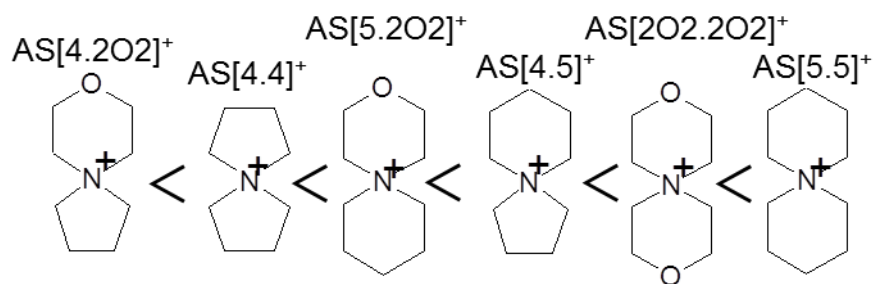

Figure 5–10. The order of melting point for fluorohydrogenate salts based on azoniaspiro-type cations, showing the effect of the number of carbon and oxygen atoms.
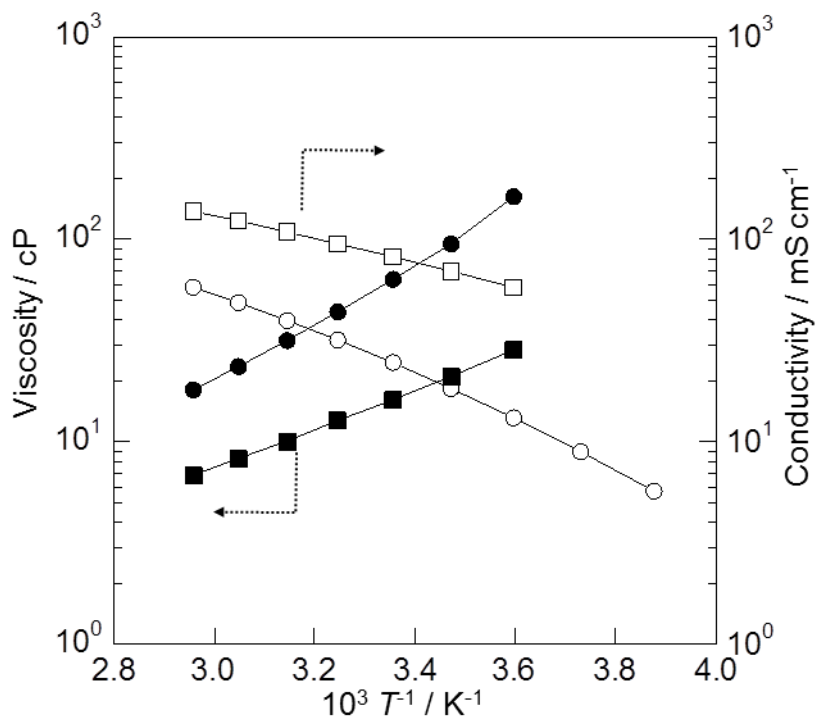
Figure 5–11. Arrhenius plots of viscosity for (■) AS[4.4](FH)$_{2.0}$F and (●) AS[4.2O2](FH)$_{1.9}$F and ionic conductivity for (□) AS[4.4](FH)$_{2.0}$F and (○) AS[4.2O2](FH)$_{1.9}$F.
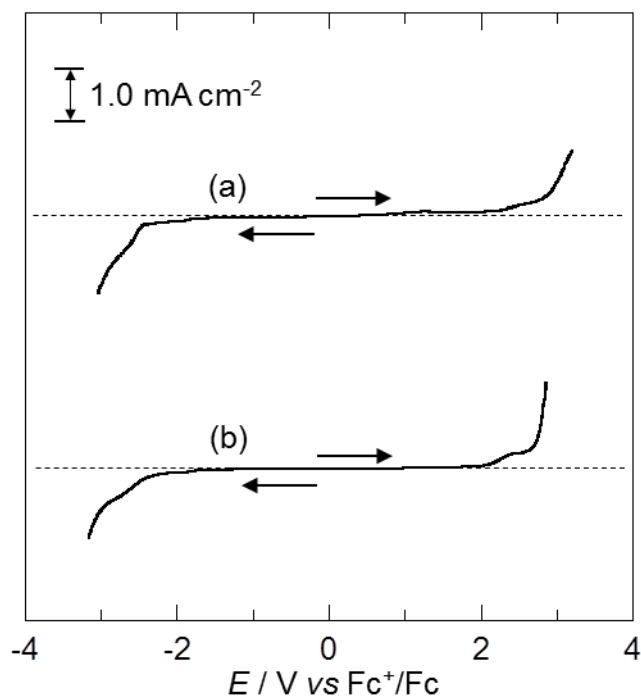

Figure 5–12. Linear sweep voltammograms of a vitreous carbon electrode in (a) AS[4.4](FH)$_{2.0}$F and (b) AS[4.2O2](FH)$_{1.9}$F.

Chapter 6

Sulfonium cation based fluorohydrogenate salts

6.1 Introduction

According to previous reports, small aliphatic trialkylsulfonium–based ILs have relatively low melting points and high ionic conductivity comparable to imidazolium–based ILs, (cf. T_m = 218 K and σ = 15.7 mS cm^{-1} at 298 K for $S_{122}N(SO_2F)_2$, T_m = 250 K and σ = 5.8 mS cm^{-1} at 298 K for $S_{122}N(SO_2CF_3)_2$, no melting point and σ = 26.8 mS cm^{-1} at 298 K for $S_{122}N(CN)_2$, T_m = 260 K and σ = 16.5 mS cm^{-1} at 298 K for EMImN(SO$_2$F)$_2$, T_m = 257 K and σ = 8.4 mS cm^{-1} at 298 K for EMImN(SO$_2$CF$_3$)$_2$, and T_m = 261 K and 27 mS cm^{-1} at 293 K for EMImN(CN)$_2$, where EMIm, T_m and σ denote 1-ethyl-3-methylimidazolium, melting point, and ionic conductivity, respectively) [1–5].

Considering the properties of the previously reported ILs of fluorohydrogenate anion and trialkylsulfonium cation, combination of these two species is interesting to obtain low melting point and high ionic conductivity. This chapter describes synthesis and properties of ILs composed of fluorohydrogenate anion and a trialkylsulfonium (S_{111}, S_{112}, S_{122}, or S_{222}) cation. Effects of cationic structure and alkyl chain length on physicochemical properties of the ILs are discussed

6.2 Experimental

The S_{111}Br was recrystallized from acetonitrile by adding ethyl acetate and dried at 353 K under vacuum for one day. The three iodide salts, S_{112}I, S_{122}I, and S_{222}I, were synthesized in the same manner as previously reported and washed several times with ethyl acetate [6]. The S_{112}I was synthesized by the reaction of dimethylsulfide and iodoethane in acetone at 298 K

for two days, and washed by ethyl acetate several times. The $S_{122}I$ was synthesized by the reaction of diethylsulfide and iodomethane in acetone at 298 K for two days, and washed by ethyl acetate several times. The $S_{222}I$ was synthesized by the reaction of diethylsulfide and iodoethane in acetone at 298 K for two days, and washed with ethyl acetate several times. Purification of $S_{112}I$ and $S_{222}I$ were performed by recrystallization from acetonitrile, adding ethyl acetate. Recovered iodides were dried at 353 K. The salt, $S_{122}I$, was washed with ethyl acetate after removal of acetonitrile under vacuum, followed by drying at 298 K. All the trialkylsulfonium halides were obtained as white powders. $S_{112}I$; Anal. Calcd for C4H11SI: C, 22.0; H, 5.0; S, 14.7; I, 58.3. Found: C, 21.5; H, 5.0; S, 14.3; I, 57.3. $S_{122}I$; Anal. Calcd for C5H13SI: C, 25.9; H, 5.6; S, 13.8; I, 54.7. Found: C, 25.4; H, 5.5; S, 13.6; I, 54.5. $S_{222}I$; Anal. Calcd for C6H15SI: C, 29.3; H, 6.1; S, 13.0; I, 51.6. Found: C, 29.2; H, 6.2; S, 12.9; I, 51.6.

Trialkylsulfonium FHILs were prepared by the reaction of large excess of aHF and trialkylsulfonium halides as described in Chapter 2. The HF contents in the four ILs were checked by weight change and neutralization titration using an aqueous NaOH solution. Testing for the presence of residual Br^- or I^- with an aqueous $AgNO_3$ solution gave no precipitation of silver halides. Infrared spectroscopy identified fluorohydrogenate anions for $S_{111}(FH)_{1.9}F$, $S_{112}(FH)_{2.0}F$, $S_{122}(FH)_{2.0}F$ and $S_{222}(FH)_{2.0}F$ (Figure 6–1). $S_{111}(FH)_{1.9}F$; IR (AgCl): $\nu = 2340$ (m), 1976 (m), 1802 (s), 1051 (w) cm^{-1}, $S_{112}(FH)_{2.0}F$; IR (AgCl): $\nu = 2340$ (m), 1978 (m), 1802 (s), 1051 (w) cm^{-1}, $S_{122}(FH)_{2.0}F$; IR (AgCl): $\nu = 2340$ (m), 1982 (m), 1806 (s), 1043 (w) cm^{-1}, and $S_{222}(FH)_{2.0}F$; IR (AgCl): $\nu = 2340$ (m), 1989 (m), 1804 (s), 1043 (w) cm^{-1}. Karl–Fischer measurements showed water contents of around 100 ppm for the present FHILs.

6.3 Results and discussion

6.3.1 HF content

When the sample was evacuated at room temperature, the vacuum-stable HF content in FHILs was 2.3 for most alkylammonium and phosphonium cations according to the previous studies [7–10]. There are some exceptions such as the salts of 1-alkyl-3-methylimidazolium cations with a long alkyl chain [11]. The present study showed that the n value for trialkylsulfonium FHILs is below 2.3 ($S_{111}(FH)_{1.9}F$, $S_{112}(FH)_{2.0}F$, $S_{122}(FH)_{2.0}F$, and $S_{222}(FH)_{2.0}F$). These results show fluorohydrogenate anions which work as a Lewis base decrease their vacuum-stable HF composition to become a smaller anion with stronger hydrogen bonds between the fluoride ion and HF so that the small sulfonium countercation is stabilized. Alkyl chain length also seems to influence the n value since the decrease in alkyl chain length slightly decreases the HF content (compare the case of $S_{111}(FH)_{1.9}F$ to the other cases).

6.3.2 Thermal behavior

Physicochemical properties of $S_{111}(FH)_{1.9}F$, $S_{112}(FH)_{2.0}F$, $S_{122}(FH)_{2.0}F$, and $S_{222}(FH)_{2.0}F$ are summarized in Table 6–1. Thermogravimetric curves of trialkylsulfonium FHILs are shown in Figure 6–2. Thermal decomposition temperatures based on the onset of large weight loss for $S_{111}(FH)_{1.9}F$, $S_{112}(FH)_{2.0}F$, $S_{122}(FH)_{2.0}F$, and $S_{222}(FH)_{2.0}F$ are 447, 437, 431, and 420 K, respectively. Gradual weight loss below the decomposition temperature is caused by reversible HF dissociation from $(FH)_nF^-$. Decomposition products are considered to be fluoroalkane and dialkylsulfide. This decomposition reaction results from the attack of $(FH)_nF^-$ as an nucleophile to the α–carbon in trialkylsulfonium cations, leaving dialkylsulfide as an elimination group [12]. Decomposition temperature of trialkylsulfonium FHILs tends to increase with decrease in alkyl chain length and are still lower than those for previously

99

reported alkylammonium FHILs, (e.g. around 540 K for EMIm(FH)$_{2.3}$F and 500 K for EMPyr(FH)$_{2.3}$F) because of the weaker C–S bond than C–N bond [7,8,13,14]. Differential scanning calorimetry showed melting points of S$_{111}$(FH)$_{1.9}$F, S$_{112}$(FH)$_{2.0}$F, and S$_{222}$(FH)$_{2.0}$F are 242, 227, and 217 K, respectively, whereas S$_{122}$(FH)$_{2.0}$F does not show a melting point above 140 K (Figure 6–3).

6.3.3 Viscosity and ionic conductivity

Arrhenius plots of viscosity and ionic conductivity for S$_{111}$(FH)$_{1.9}$F, S$_{112}$(FH)$_{2.0}$F, S$_{122}$(FH)$_{2.0}$F, and S$_{222}$(FH)$_{2.0}$F are shown in Figures 6–4 and 6–5, respectively. The detailed values of viscosity and ionic conductivity for S$_{111}$(FH)$_{1.9}$F, S$_{112}$(FH)$_{2.0}$F, S$_{122}$(FH)$_{2.0}$F, and S$_{222}$(FH)$_{2.0}$F are summarized in Tables 6–2 and 6–3. Viscosity at 298 K increases in the order of S$_{111}$(FH)$_{1.9}$F (7.8 cP) < S$_{112}$(FH)$_{2.0}$F (8.2 cP) < S$_{222}$(FH)$_{2.0}$F (8.3 cP) < S$_{122}$(FH)$_{2.0}$F (8.9 cP). There are two factors that can influence viscosity of ILs besides the columbic interactions; van der Waals interactions and conformational degrees of freedom [1]. Increase of the former increases viscosity, whereas increase of the latter decreases viscosity. In the present cases, the viscosity of S$_{222}$(FH)$_2$F is lower than that of S$_{122}$(FH)$_2$F. Similar behavior was reported in the cases of S$_{222}$N(SO$_2$F)$_2$ (20 cP) and S$_{122}$N(SO$_2$F)$_2$ (24 cP) [1]. Such behavior arises from the larger effect of conformational degrees of freedom than that of van der Waals interaction. When compared to previously known FHILs, viscosities of trialkylsulfonium FHILs are higher than those of EMIm(FH)$_{2.3}$F (4.9 cP) and lower than those of EMPyr(FH)$_{2.3}$F (11.5 cP) [8,13].

The highest ionic conductivity in the presently known ILs is observed for S$_{111}$(FH)$_{1.9}$F (131 mS cm^{-1}). The ionic conductivity at 298 K decreases in the order of S$_{111}$(FH)$_{1.9}$F > S$_{112}$(FH)$_{2.0}$F (111 mS cm^{-1}) > S$_{122}$(FH)$_{2.0}$F (91 mS cm^{-1}) > S$_{222}$(FH)$_{2.0}$F (83 mS cm^{-1}) with increase in the size of cation. Although the high ionic conductivity of FHILs is derived from

the exchanging HF unit working as a dielectric spacer, the values for the present trialkylsulfonium FHILs are particularly high [15]. Since the viscosities of trialkylsulfonium FHILs are not the lowest in the known FHILs, their high ionic conductivities arise from the large number of ions per volume because of the small size of the cations.

6.3.4 Electrochemical stability

Linear sweep voltammograms of a vitreous carbon electrode in trialkylsulfonium FHILs are shown in Figure 6–6. The anode and cathode limit potentials are determined when the absolute value of the current density exceeds 0.5 mA cm^{-2} at a scan rate of 10 mV s^{-1}. The cathode limit potentials range between -1.64 and -2.10 V and the anode limit potentials between $+2.45$ and $+2.83$ V. Electrochemical windows of $S_{111}(FH)_{1.9}F$, $S_{112}(FH)_{2.0}F$, $S_{122}(FH)_{2.0}F$, and $S_{222}(FH)_{2.0}F$ are 4.09, 4.20, 4.37, and 4.93 V, respectively. Replacement of methyl group with ethyl group slightly increases the electrochemical window as shown for other FHILs in the previous reports [7]. Trialkylsulfonium cations in $S_{122}N(SO_2F)_2$ and $S_{222}N(SO_2F)_2$ are reduced around -2.18 V vs. Fc$^+$/Fc, whereas $(FH)_nF^-$ in FHILs are reduced at -1.0 to -2.9 V vs. Fc$^+$/Fc on a vitreous carbon electrode [1,6,8–10,13]. Consequently, the cathode reaction of trialkylsulfonium FHILs probably involves reduction of both or either the cation and anion [8,9,13]. The reaction at the anode limit is considered to be a decomposition of the cation including its fluorination by the anion [8,9,13]. Electrochemical windows of trialkylsulfonium FHILs are larger than alkylimidazolium FHILs (about 3 V) and smaller than alkylpyrrolidinium or alkylphosphonium FHILs (4.6 – 6.0 V) [8,9,13].

References

[1] H.-B. Han, J. Nie, K. Liu, W.-K. Li, W.-F. Feng, M. Armand, H. Matsumoto, Z.-B. Zhou, *Electrochim. Acta*. **2010**, *55*, 1221.

[2] S. Fang, L. Yang, C. Wei, C. Peng, K. Tachibana, K. Kamijima, *Electrochem. Commun.* **2007**, *9*, 2696.

[3] D. Gerhard, S. C. Alpaslan, H. J. Gores, M. Uerdingen, P. Wasserscheid, *Chem. Commun.* **2005**, *9*, 5080.

[4] M. Ishikawa, T. Sugimoto, M. Kikuta, E. Ishiko, M. Kono, *J. Power Sources* **2006**, *162*, 658.

[5] Y. Yoshida, K. Muroi, A. Otsuka, G. Saito, M. Takahashi, T. Yoko, *Inorg. Chem.* **2004**, *43*, 1458.

[6] H. Paulsson, A. Hagfeldt, L. Kloo, *J. Phys. Chem. B* **2003**, *107*, 13665.

[7] R. Hagiwara, K. Matsumoto, Y. Nakamori, T. Tsuda, Y. Ito, H. Matsumoto, K. Momota, *J. Electrochem. Soc.* **2003**, *150*, D195.

[8] K. Matsumoto, R. Hagiwara, Y. Ito, *Electrochem. Solid-State Lett.* **2004**, *7*, E41.

[9] S. Kanematsu, K. Matsumoto, R. Hagiwara, *Electrochem. Commun.* **2009**, *11*, 1312.

[10] M. Yamagata, S. Konno, K. Matsumoto, R. Hagiwara, *Electrochem. Solid-State Lett.* **2009**, *12*, F9.

[11] F. Xu, K. Matsumoto, R. Hagiwara, *Chem. Eur. J.* **2010**, *16*, 12970.

[12] Y. Pocker, A. J. Parker, *J. Org. Chem.* **1966**, *31*, 1526.

[13] R. Hagiwara, T. Hirashige, T. Tsuda, Y. Ito, *J. Electrochem. Soc.* **2002**, *149*, D1.

[14] D. F. Shriver, P. W. Atkins, *Inorganic Chemistry third ed.*, Oxford University Press, **1999**.

[15] T. Enomoto, Y. Nakamori, K. Matsumoto, R. Hagiwara, *J. Phys. Chem. C* **2011**, *115*, 4324.

Table 6–1. Physicochemical properties of $S_{111}(FH)_{1.9}F$, $S_{112}(FH)_{2.0}F$, $S_{122}(FH)_{2.0}F$, and $S_{222}(FH)_{2.0}F$.

	Fw	T_m / K	T_d / K	ρ / g cm^{-3}	η / cP	σ / mS cm^{-1}	λ / S cm^2 mol^{-1}	E_{ca} / V vs Fc$^+$/Fc	E_{an} / V vs Fc$^+$/Fc
$S_{111}(FH)_{1.9}F$	134	242	447	1.18	7.8	131	14.9	−1.64	2.45
$S_{112}(FH)_{2.0}F$	150	227	437	1.14	8.2	111	14.6	−1.73	2.47
$S_{122}(FH)_{2.0}F$	164	−	431	1.11	8.9	91	13.4	−1.86	2.51
$S_{222}(FH)_{2.0}F$	178	217	420	1.09	8.3	83	13.6	−2.10	2.83

Fw: Formula weight, T_m: melting point, T_d: decomposition temperature (onset), ρ: density, η: viscosity, σ: conductivity, λ: molar conductivity, E_{ca}: cathode limit potential, E_{an}: anode limit potential.

Table 6–2. Viscosities (η) for $S_{111}(FH)_{1.9}F$, $S_{112}(FH)_{2.0}F$, $S_{122}(FH)_{2.0}F$, and $S_{222}(FH)_{2.0}F$.

T / K	$S_{111}(FH)_{1.9}F$	$S_{112}(FH)_{2.0}F$	$S_{122}(FH)_{2.0}F$	$S_{222}(FH)_{2.0}F$
		η / cP		
328	4.3	4.5	4.7	4.3
318	5.2	5.4	5.7	5.3
308	6.3	6.6	7.1	6.6
298	7.8	8.2	8.9	8.3
288	9.8	10.5	11.4	10.8
278	13.4	14.5	15.2	14.4

Table 6–3. Ionic conductivities (σ) for $S_{111}(FH)_{1.9}F$, $S_{112}(FH)_{2.0}F$, $S_{122}(FH)_{2.0}F$, and $S_{222}(FH)_{2.0}F$.

T / K	$S_{111}(FH)_{1.9}F$	$S_{112}(FH)_{2.0}F$	$S_{122}(FH)_{2.0}F$	$S_{222}(FH)_{2.0}F$
		σ / mS cm^{-1}		
323	185	158	132	128
313	164	140	115	107
298	131	111	91.1	83.3
283	97.1	85.7	68.4	62.5
268	66.3	61.4	48.0	43.5
258	49.1	47.9	36.3	32.5
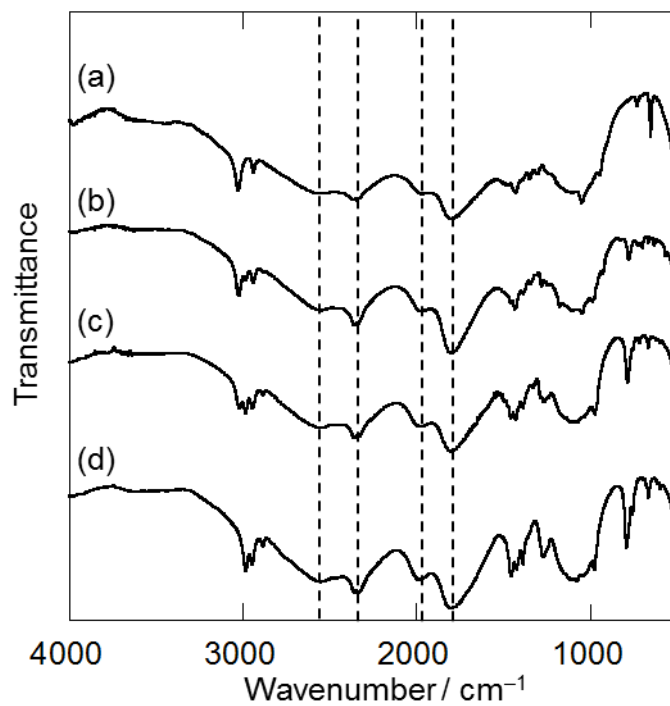
Figure 6–1. Infrared spectra of (a) $S_{111}(FH)_{1.9}F$, (b) $S_{112}(FH)_{2.0}F$, (c) $S_{122}(FH)_{2.0}F$, and $S_{222}(FH)_{2.0}F$.
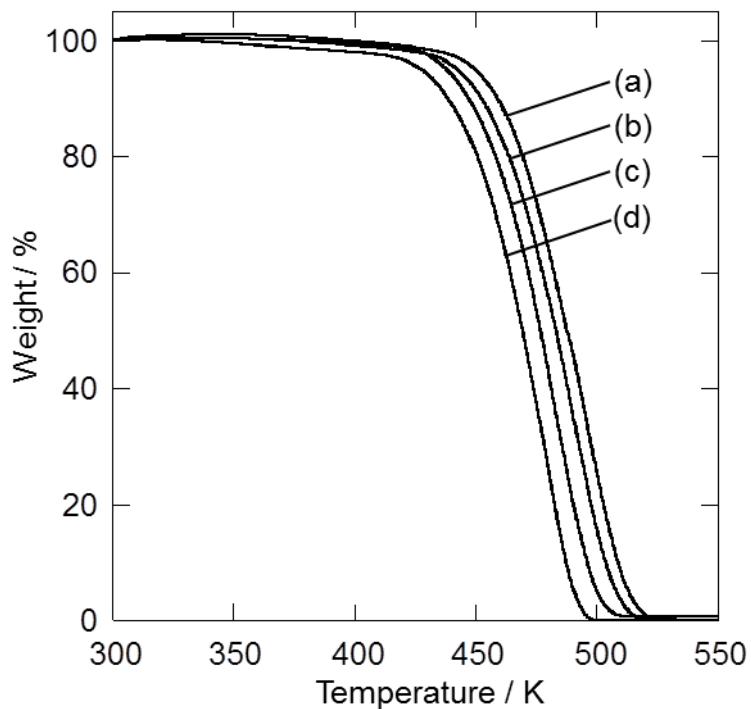

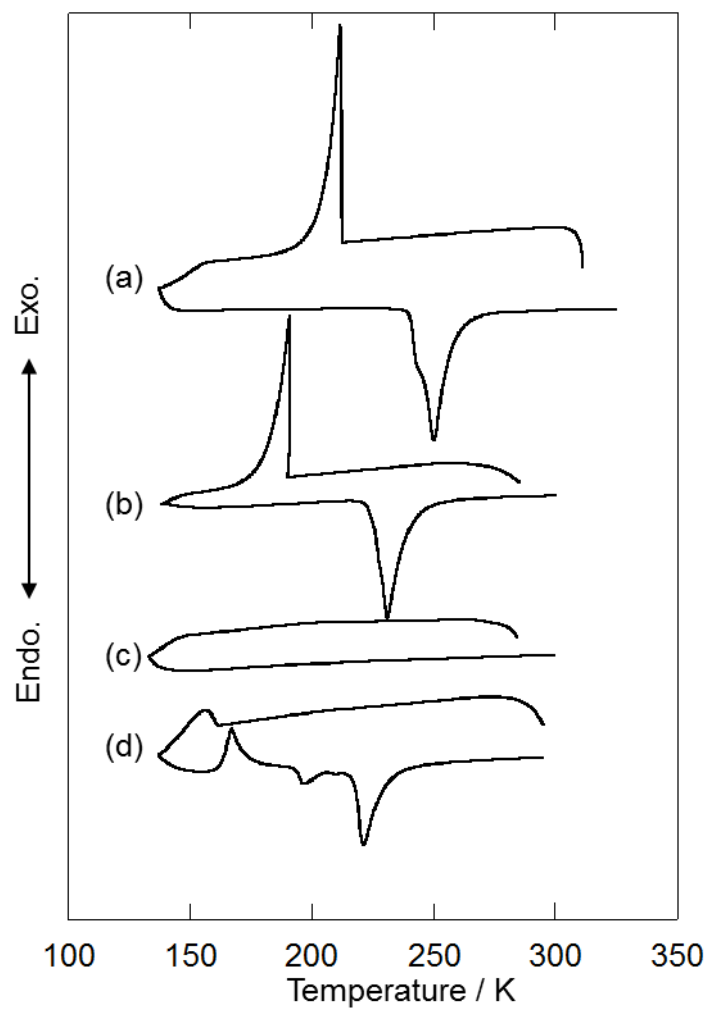Figure 6–2. Thermogravimetric curves of (a) $S_{111}(FH)_{1.9}F$, (b) $S_{112}(FH)_{2.0}F$, (c) $S_{122}(FH)_{2.0}F$, and $S_{222}(FH)_{2.0}F$.

105

Figure 6–3. Differential scanning calorimetric curves of (a) $S_{111}(FH)_{1.9}F$, (b) $S_{112}(FH)_{2.0}F$, (c) $S_{122}(FH)_{2.0}F$, and $S_{222}(FH)_{2.0}F$.
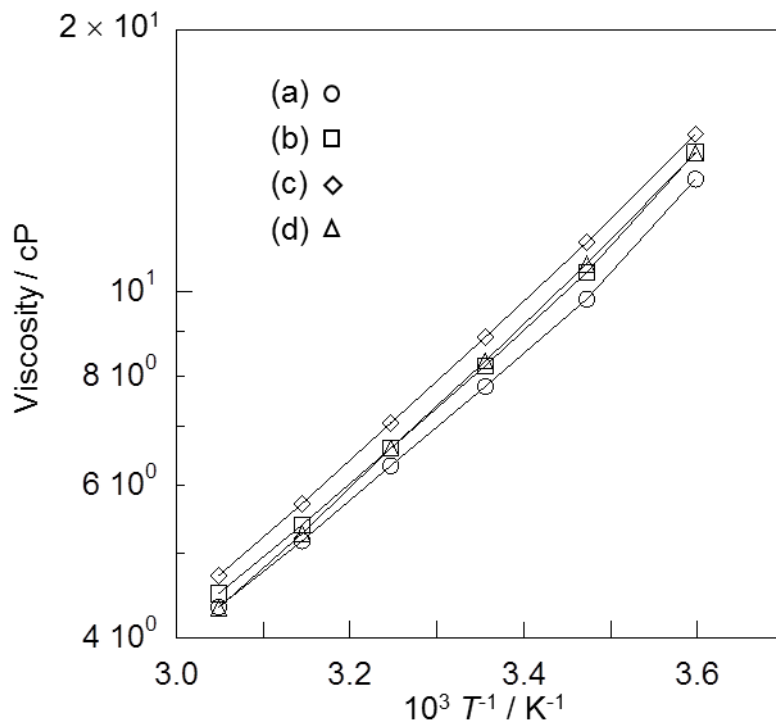
Figure 6–4. Arrhenius plots of viscosity for (a) $S_{111}(FH)_{1.9}F$, (b) $S_{112}(FH)_{2.0}F$, (c) $S_{122}(FH)_{2.0}F$, and (d) $S_{222}(FH)_{2.0}F$.
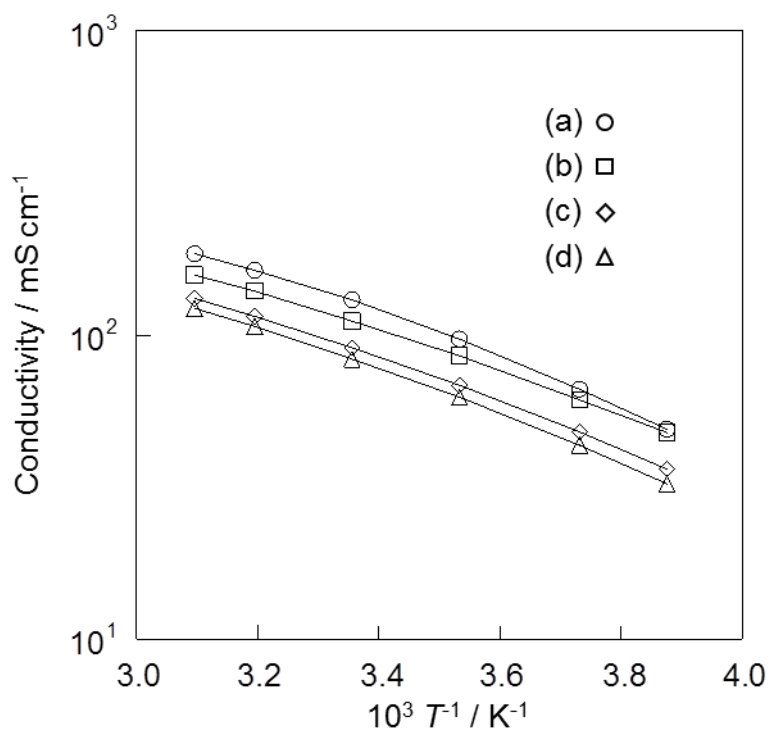

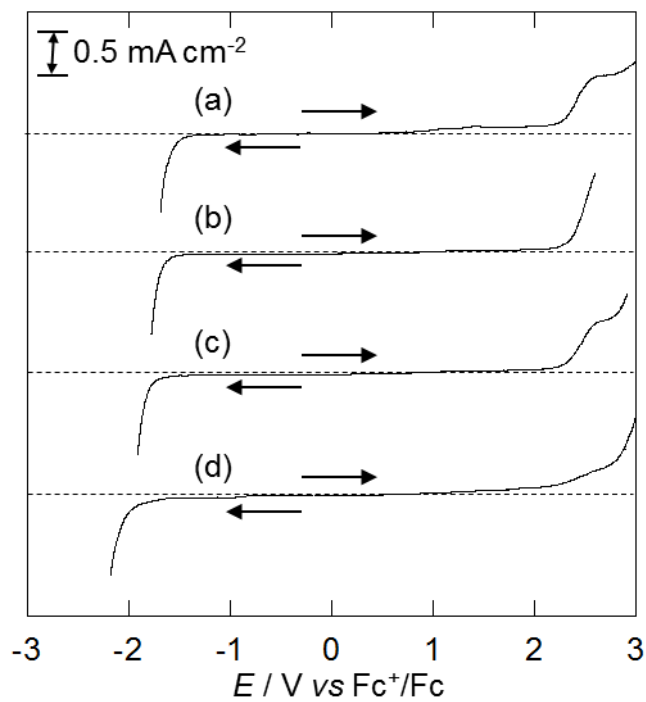Figure 6–5. Arrhenius plots of ionic conductivity for (a) $S_{111}(FH)_{1.9}F$, (b) $S_{112}(FH)_{2.0}F$, (c) $S_{122}(FH)_{2.0}F$, and (d) $S_{222}(FH)_{2.0}F$.

107

Figure 6–6. Linear sweep voltammograms of (a) $S_{111}(FH)_{1.9}F$, (b) $S_{112}(FH)_{2.0}F$, (c) $S_{122}(FH)_{2.0}F$ and (d) $S_{222}(FH)_{2.0}F$ on a vitreous carbon electrode. Potential was referenced to the ferrocenium (Fc^+) / ferrocene (Fc) redox couple.

Chapter 7

Fluorohydrogenate salts based on polyfluoroalkylimidazolium cations

7.1 Introduction

Ionic liquids based on polyfluoroalkylated cations have been studied as hydrophobic ILs with some interesting properties; inertness to organic solvents and oxidizing agents, resistance to corrosive acids and bases, and resistance to extremes of temperature and pressure [1–6]. These ILs were mainly applied as reaction solvents for organic reactions and separations as well as catalysis due to their unique properties [1], whereas there are little reports about the usage as electrolytes for electrochemical devices. In this chapter, fluorohydrogenate salts based on polyfluoroalkylated imidazolium cations are synthesized and characterized, and the effects of the polyfluoroalkyl side-chain on the physicochemical properties of fluorohydrogenate salts are discussed.

7.2 Experimental

The numbers of fluorine atoms in the side-chain of 1-methyl-3-polyfluoroalkylimidazolium cations ($C_{(x+2)F(2x+1)}MIm^+$, x is the number of carbon atoms with fluorine atoms) are 3 ($C_{3F3}MIm^+$), 5 ($C_{4F5}MIm^+$), 9 ($C_{6F9}MIm^+$), 13 ($C_{8F13}MIm^+$), and 17 ($C_{10F17}MIm^+$), where the two carbon atoms from the root of the side-chain are not fluorinated as shown in Figure 7–1. According to the previous report [2], the starting iodides $C_{(x+2)F(2x+1)}MImI$ were prepared by reactions of 1-methylimidazole and nearly equimolar quantities of the corresponding polyfluoroalkyl iodides at 353 K for 48 h. Purification of $C_{3F3}MImI$ was performed by washing with ethyl acetate several times and recrystallization from the acetonitrile solution by adding ethyl acetate. Purification of $C_{4F5}MImI$, $C_{6F9}MImI$,

and C_{8F13}MImI was performed by washing with ethyl acetate several times, chromatography using the activated alumina column with acetone, and recrystallization from the acetone solution by adding diethyl ether. Purification of C_{10F17}MImI was performed by washing with ethyl acetate several times, chromatography using the activated alumina column with acetone, and recrystallization from the acetone solution by adding ethyl acetate. Finally the purified iodides were dried under vacuum at 353 K. The results of elemental analysis of $C_{(x+2)F(2x+1)}$MImI are summarized below. C_{3F3}MImI; Anal. Calcd. for C7H10N2F3I: C, 27.45; H, 3.27; N, 9.15; F, 18.63; I, 41.50. Found: C, 27.33; H, 3.44; N, 9.11, F, 18.05; I, 41.91. C_{4F5}MImI; Anal. Calcd. for C8H10N2F5I: C, 26.98; H, 2.83; N, 7.87; F, 26.68; I, 35.64. Found: C, 26.95; H, 2.81; N, 7.92, F, 26.70; I, 35.65. C_{6F9}MImI; Anal. Calcd. for C10H10N2F9I: C, 26.33; H, 2.21; N, 6.14; F, 37.49; I, 27.82. Found: C, 26.36; H, 2.24; N, 6.24, F, 37.94; I, 28.03. C_{8F13}MImI; Anal. Calcd. for C12H10N2F13I: C, 25.92; H, 1.81; N, 5.04; F, 44.41; I, 22.82. Found: C, 25.3; H, 1.77; N, 4.99, F, 44.38; I, 23.21. C_{10F17}MImI; Anal. Calcd. for C14H10N2F17I: C, 25.63; H, 1.54; N, 4.27; F, 49.22; I, 19.34. Found: C, 25.34; H, 1.44; N, 4.18, F, 49.21; I, 18.99.

All the $C_{(x+2)F(2x+1)}$MIm(FH)$_n$F salts were prepared by reaction of the corresponding iodide and excess anhydrous HF as previously described. In order to compare the effects of fluorine atoms, 1-methyl-3-propylimidazolium fluorohydrogenate (C_3MIm(FH)$_{1.7}$F) was synthesized and characterized, where C_{3F3}MIm(FH)$_{1.7}$F and C_3MIm(FH)$_{1.7}$F have the same number of carbon atoms and there is only the difference between terminal methyl group and trifluoromethyl group in the side-chain. The HF content of fluorohydrogenate salts were determined by titration using aq. 0.1029 M NaOH and weight change before and after the reaction with HF. The (FH)$_n$F$^-$ anions were identified by IR spectroscopy. C_3MIm(FH)$_{1.7}$F; IR (AgCl): ν = 2340 (m), 1985 (m), 1807 (s), 1045 (w) cm^{-1}, C_{3F3}MIm(FH)$_{1.7}$F; IR (AgCl): ν = 2337 (m), 1983 (m), 1807 (s), 1021 (w) cm^{-1}, C_{4F5}MIm(FH)$_{1.7}$F; IR (AgCl): ν = 2350 (m),

1981 (m), 1811 (s), 1022 (w) cm^{-1}, C$_{6F9}$MIm(FH)$_{1.8}$F; IR (AgCl): ν = 2350 (m), 1979 (m), 1811 (s), 1036 (w) cm^{-1}, C$_{8F13}$MIm(FH)$_{2.0}$F; IR (AgCl): ν = 2340 (m), 1977 (m), 1813 (s), 1042 (w) cm^{-1}, and C$_{10F17}$MIm(FH)$_{2.0}$F; IR (AgCl): ν = 2350 (m), 1981 (m), 1815 (s), 1042 (w) cm^{-1} [(FH)$_2$F$^-$, see Figure 7–2 for their IR spectra].

7.3 Results and discussion

7.3.1 Physical properties

At room temperature, C$_{3F3}$MIm(FH)$_{1.7}$F, C$_{4F5}$MIm(FH)$_{1.7}$F, and C$_{6F9}$MIm(FH)$_{1.8}$F are liquid, while C$_{8F13}$MIm(FH)$_{2.0}$F and C$_{10F17}$MIm(FH)$_{2.0}$F are powdery solid. Two solid salts have the vacuum-stable HF content of 2.0 (C$_{8F13}$MIm(FH)$_{2.0}$F and C$_{10F17}$MIm(FH)$_{2.0}$F), suggesting the formation of the one to one crystal phase of the cations and (FH)$_2$F$^-$, while the other three RTILs have the lower HF content (C$_{3F3}$MIm(FH)$_{1.7}$F, C$_{4F5}$MIm(FH)$_{1.7}$F, and C$_{6F9}$MIm(FH)$_{1.8}$F). Previous reports show that the vacuum-stable HF content in FHILs based on imidazolium, pyridinium, pyrrolidinium, and piperidinium cations with short side-chains is 2.3 and those with long side-chains are below 2.3 [7–10]. This trend was not adapted to the present FHILs based on polyfluoroalkylated cations. Long side-chain or polyfluoroalkylated side-chain give strong van der Waals interactions between the side-chains, which may affect the cation-anion interactions and lower the vacuum-stable HF content.

Fluorine containing groups often enhance hydrophobicity due to their low polarity. In the present study, all the C$_{(x+2)F(2x+1)}$MIm(FH)$_n$F salts give a biphasic system at first when contacted with water. However, they slowly dissolved into water and form a single phase after a while although the whole fluorine weight in formula weight in cation is over 50%. Fluorohydrogenate anions are highly polar and form strong interactions with water, resulting in the strong hydrophilicity that overcomes the hydrophobicity of C$_{(x+2)F(2x+1)}$MIm$^+$. The massive introduction of fluorine atom together with extension of the side-chain in this study

was not sufficient to give hydrophobicity to the FHILs. On the other hand, the mixture of water and $C_{(x+2)F(2x+1)}MIm(FH)_nF$ made bubbles when vigorously agitated because the cations with separated polar and non-polar regions show an interfacial activity.

7.3.2 Thermal properties

Thermogravimetric curves of $C_{(x+2)F(2x+1)}MIm(FH)_nF$ and $C_3MIm(FH)_{1.7}F$ are shown in Figure 7–3. Thermal decomposition temperatures based on the onset of large weight loss for $C_{(x+2)F(2x+1)}MIm(FH)_nF$ and $C_3MIm(FH)_{1.7}F$ are around 460 and 530 K, respectively. Gradual weight loss below the decomposition temperature is caused by HF dissociation from $(FH)_nF^-$. The introduction of polyfluoroalkyl side-chain in the cation lowers the thermal stability of the FHIL. Pyrolysis of imidazolium halides occurs by an S_N2 reaction, where the halide ion attacks α-carbon and alkylimidazole leaves [11]. Steric effects of the side-chain in the imidazolium cation are weaker for short side-chain than long side-chain, resulting in the preferential break of C–N bond between nitrogen in imidazolium and α-carbon in short side-chain, and resulting in the formation of imidazole with the long side-chain as a leaving group [11]. In addition, the S_N2 reaction rate for pyrolysis is high in the case of the leaving group with low Lewis basicity. In the present cases, the main leaving group in pyrolysis of $C_{3F3}MIm(FH)_{1.7}F$ and $C_3MIm(FH)_{1.7}F$ is thought to be 1-(3,3,3-trifluoropropyl)imidazole and 1-propylimidazole, respectively. Because the polyfluoroalkyl side-chain withdraws the electron from the aromatic ring through ethylene group and lowers the Lewis basicity of 1-(3,3,3-trifluoropropyl)imidazole compared to that of 1-propylimidazole, thermal decomposition of $C_{3F3}MIm(FH)_{1.7}F$ would be accelerated compared to that of $C_3MIm(FH)_{1.7}F$. In the cases of the cations with longer polyfluorinated side-chains, the clear difference of decomposition behavior was not observed because fluorine atoms distant from the aromatic ring do not effectively withdraw the electrons from the ring.

Differential scanning calorimetric curves of $C_{(x+2)F(2x+1)}MIm(FH)_nF$ and $C_3MIm(FH)_{1.7}F$ are shown in Figure 7–4. Two RTILs, $C_{3F3}MIm(FH)_{1.7}F$ and $C_{6F9}MIm(FH)_{1.8}F$, have large endothermic peaks corresponding to melting. The $C_{4F5}MIm(FH)_{1.7}F$ salt exhibits only a glass transition. In the DSC curve of $C_{8F13}MIm(FH)_{2.0}F$, large endothermic and small endothermic peaks are observed at 326 and 382 K, respectively. As described below, the former peak shows a phase transition from the crystal phase to liquid crystal phase (melting) and the latter peak shows a phase transition from liquid crystal phase to isotropic liquid phase (clearing). In the DSC curve of $C_{10F17}MIm(FH)_{2.0}F$, a large endothermic peak (melting) is observed at 349 K, whereas the peak corresponding to clearing is not observed because the clearing temperature is higher than its decomposition temperature.

7.3.3 Physicochemical properties

Physicochemical properties of $C_{(x+2)F(2x+1)}MIm(FH)_nF$ and $C_3MIm(FH)_{1.7}F$ are summarized in Table 7–1. Introduction of fluorine atoms increases density as observed in the comparison between $C_{3F3}MIm(FH)_{1.7}F$ (1.35 g cm^{-3}) and $C_3MIm(FH)_{1.7}F$ (1.12 g cm^{-3}). The large density of $C_{3F3}MIm(FH)_{1.7}F$ originates from the large difference in atomic weight and the small difference in size between fluorine and hydrogen atoms [12–14], where the difference of the formula weight is large (232 for $C_{3F3}MIm(FH)_{1.7}F$ and 178 for $C_3MIm(FH)_{1.7}F$, respectively) and the difference of molar volume, calculated by FW/ρ, is small (172 cm^3 mol^{-1} for $C_{3F3}MIm(FH)_{1.7}F$ and 159 cm^3 mol^{-1} for $C_3MIm(FH)_{1.7}F$, respectively). The increasing number of fluorine atoms increases the ratio of the weight of the component fluorine to the formula weight of the cation, 31.8% for $C_{3F3}MIm^+$, 41.5% for $C_{4F5}MIm^+$, and 52.0% for $C_{6F9}MIm^+$, respectively, reflecting the increase in density.

The $C_{3F3}MIm(FH)_{1.7}F$ (28 cP at 298 K) salt exhibits a higher viscosity than $C_3MIm(FH)_{1.7}F$ (13 cP at 298 K). Fluorous interaction between adjacent cations is a possible

reason for this phenomenon [15]. Extension of polyfluoroalkyl side-chain leads to higher viscosities (87 cP for $C_{4F5}MIm(FH)_{1.7}F$ and 169 cP for $C_{6F9}MIm(FH)_{1.8}F$) because the fluorous interaction between polyfluoroalkyl side-chains increases [15]. Figure 7–5 shows Arrhenius plots of viscosity and ionic conductivity for the present RTILs and Table 7–2 lists activation energies obtained from these plots. The ionic conductivity decreases with increase in the viscosity for any salts. Both the activation energies increase with introducing a larger number of fluorine atoms. A similar tendency and relatively small discrepancy between the activation energies of viscosity and ionic conductivity suggest that high ionic conductivity is explained by the low viscosity.

Linear sweep voltammograms of $C_{3F3}MIm(FH)_{1.7}F$ and $C_3MIm(FH)_{1.7}F$ are shown in Figure 7–6. The electrochemical stability of $C_3MIm(FH)_{1.7}F$ is similar to $C_3MIm(FH)_{2.3}F$ in spite of the different HF content. The anodic limit of $C_3MIm(FH)_{1.7}F$ is considered to be oxidation of imidazolium cations, including fluorination by fluorohydrogenate anions, about 1 V vs. Fc^+/Fc [9]. For $C_{3F3}MIm(FH)_{1.7}F$ in Figure 7–6, the first oxidation at about 1 V vs. Fc^+/Fc is similar to the case for $C_3MIm(FH)_{1.7}F$ and an improvement of electrochemical stability to oxidation by introducing fluorine atoms was not observed. The smaller current of the first oxidation and the following smaller current below the second oxidation at around 2 V vs. Fc^+/Fc indicates that the oxidation product of $C_{3F3}MIm(FH)_{1.7}F$ suppresses the further oxidation compared to $C_3MIm(FH)_{1.7}F$. The higher onset potential of the second oxidation for $C_{3F3}MIm(FH)_{1.7}F$ shows that $C_{3F3}MIm(FH)_{1.7}F$ has a higher stability to further oxidation than $C_3MIm(FH)_{1.7}F$. On the other hand, electrochemical stability of $C_{3F3}MIm(FH)_{1.7}F$ against reduction is poorer than that of $C_3MIm(FH)_{1.7}F$ because the high electrophilicity of polyfluoroalkyl side-chains raises the acidity of the imidazolium ring.

114

7.3.4 Liquid crystal phase

Figure 7–7 shows POM textures of $C_{8F13}MIm(FH)_{2.0}F$ and $C_{10F17}MIm(FH)_{2.0}F$ at 373 K. The former was obtained by cooling the isotropic liquid, whereas the latter was obtained only by heating the crystal because $C_{10F17}MIm(FH)_{2.0}F$ decomposes without clearing. A fan-like texture spontaneously formed in both the cases. The POM image suggests that the liquid crystal has a smectic structure as observed in other imidazolium ionic liquid crystals [10].

Figures 7–8 shows the XRD patterns of the crystal and liquid crystal phases for $C_{8F13}MIm(FH)_{2.0}F$ in the low-angle and wide-angle ranges, respectively. In the crystal phase, the diffraction peaks are observed over a wide range of angle, whereas those in the liquid crystal are observed only in the low-angle region. The sharp peaks observed in the low-angle region for both the crystal (e.g., 2.75° at 293 K) and liquid crystal (e.g., 3.07° at 333 K) phases indicate formation of layered structures. The shaper peaks in the crystal phase than those in the liquid crystal phase result from the more highly ordered structure of the cations in the crystal phases. Similar phenomenon was observed in 1-dodecyl-3-methylimidazolium fluorohydrogenate ($C_{12}MIm(FH)_{2.0}F$) salts [10]. The two more peaks are observed in the lower angle region than that for the sharp peak found for the crystal phase and may result from the in-plane ordering within the layer. The weak peak around 6.3° observed in the liquid crystal phase corresponds to the 002 diffraction of the smectic phase. The effect of introducing fluorine atoms on the formation of the liquid crystal is confirmed by comparing $C_{8F13}MIm(FH)_{2.0}F$ and 1-methyl-3-octylimidazolium fluorohydrogenate ($C_8MIm(FH)_{2.0}F$), between which the difference is the existence of fluorine atoms [10]. The $C_8MIm(FH)_{2.0}F$ salts does not form the liquid crystal phase, whereas $C_{8F13}MIm(FH)_{2.0}F$ does due to the strong fluorous interaction between two side-chains. The POM image of $C_{10F17}MIm(FH)_{2.0}F$ indicates the phase found above 349 K is the liquid crystal phase, whereas the confirmation of liquid crystal by XRD at such high temperatures was technically difficult.

The layer spacings (d) for crystals and liquid crystals of $C_{8F13}MIm(FH)_{2.0}F$ are shown in Figure 7–9. Figure 7–10 shows a schematic illustration of the crystal–liquid crystal phase transition of $C_{8F13}MIm(FH)_{2.0}F$. The layer spacing of the liquid crystal in $C_{8F13}MIm(FH)_{2.0}F$ is smaller than that of the crystal, which contradicts the general trend for previously known analogues with non-fluoroalkyl side-chains [10,16,17]. The size of $C_{8F13}MIm^+$ along the long axis (from the carbon in the methyl group to the fluorine at the end of the polyfluoroalkyl group) is roughly estimated to be 15 Å according to previous crystallographic works, assuming the polyfluoroalkyl side-chain adopts all-trans conformation [18,19]. The layer spacing in the $C_{8F13}MIm(FH)_{2.0}F$ crystal (32.1 Å at 293 K) is much larger than that of $C_{12}MIm(FH)_{2.0}F$ crystal even with a longer side-chain (26.6 Å at 283 K) [10], and nearly twice larger than the $C_{8F13}MIm^+$ size along the long axis, which suggests that interdigitation does not occur in the bilayer structure of the crystal and that the layer spacing can become much smaller by deeply interdigitating the polyfluoroalkyl side-chains each other when the polyfluoroalkyl side-chains become more fluid by melting.

Reference

[1] V. R. Koch, C. Nanjundiah, R. T. Carlin, U. S. Patent (1998) 5,827,602.

[2] R. P. Singh, S. Manandhar, J. M. Shreeve, *Tetrahedron Lett*. **2002**, *43*, 9497.

[3] H. Xue, J. M. Shreeve, *Eur. J. Inorg. Chem.* **2005**, *13*, 2573.

[4] T. L. Merrigan, E. D. Bates, S. C. Dorman, *J. H. Davis, Jr., Chem. Commun*. **2000**, *20*, 2051.

[5] B. R. Caes, J. B. Binder, J. J. Blank, R. T. Raines, *Green Chem*. **2011**, *13*, 2719.

[6] J. J. Tindale, P. J. Ragogna, *Chem. Commum*. **2009**, *14*, 1831.

[7] M. Yamagata, S. Konno, K. Matsumoto, R. Hagiwara, *Electrochem. Solid-State Lett*. **2009**, *12*, F9.

[8] K. Matsumoto, R. Hagiwara, Y. Ito, *Electrochem. Solid-State Lett*. **2004**, *7*, E41.

[9] R. Hagiwara, K. Matsumoto, Y. Nakamori, T. Tsuda, Y. Ito, H. Matsumoto, K. Momota, *J. Electrochem. Soc*. **2003**, *150*, D195.

[10] F. Xu, K. Matsumoto, R. Hagiwara, *Chem. Eur. J*. **2010**, *16*, 12970.

[11] B. K. M. Chan, N.-H. Chang, M. R. Grimmett, *Aust. J. Chem*. **1977**, *30*, 2005.

[12] M. E. Wieser, T. B. Coplen, *Pure Appl. Chem*. **2011**, *83*, 359.

[13] A. Bondi, *J. Phys. Chem*. **1964**, *68*, 441.

[14] R. D. Shannon, *Acta. Cryst*. **1976**, *A32*, 751.

[15] G. D. Smith, O. Borodin, J. J. Magda, R. H. Boyd, Y. Wang, J. E. Bara, S. Miller, D. L. Gin, R. D. Noble, *Phys. Chem. Chem. Phys*. **2010**, *12*, 7064.

[16] K. Binnemans, *Chem. Rev*. **2005**, *105*, 4148.

[17] A. E. Bradley, C. Hardacre, J. D. Holbrey, S. Johnston, S. E. J. McMath, M. Nieuwenhuyzen, *Chem. Mater*. **2002**, *14*, 629.

[18] Z. Wei, X. Wei, S. Fu, J. Liu, D. Zhang, *Acta Cryst*. **2009**, *E65*, o1159.

[19] F. Xu, K. Matsumoto, R. Hagiwara, *Dalton Trans*. **2013**, *42*, 1965.

117

Table 7–1. Physicochemical properties of the present fluorohydrogenate salts.

	Fw	T_m / K	T_c / K	ρ / g cm^{-3}	η / cP	σ / mS cm^{-1}
C$_3$MIm(FH)$_{1.7}$F	178	152 (T_g)	n.o.	1.12	13	31
C$_{3F3}$MIm(FH)$_{1.7}$F	232	274	n.o.	1.35	28	13
C$_{4F5}$MIm(FH)$_{1.7}$F	282	186 (T_g)	n.o.	1.43	87	5.6
C$_{6F9}$MIm(FH)$_{1.8}$F	384	276	n.o.	1.53	169	2.4
C$_{8F13}$MIm(FH)$_{2.0}$F	488	326	382	–	–	–
C$_{10F17}$MIm(FH)$_{2.0}$F	588	349	dec.	–	–	–

Fw: formula weight, T_m: melting point, T_g: glass transition temperature, T_c: clearing temperature, ρ: density at 298 K, η: viscosity at 298 K, σ: conductivity at 298 K, n.o.: not observed.

Table 7–2. Activation energies calculated from the Arrhenius plots of viscosities and ionic conductivities for the present RTILs.

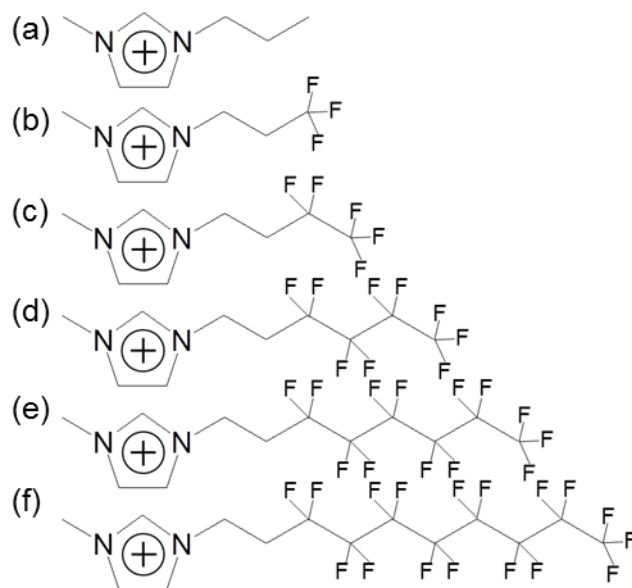|	Activation energy of viscosity / kJ mol^{-1}	Activation energy of conductivity / kJ mol^{-1}
C$_3$MIm(FH)$_{1.7}$F	20.0	17.4
C$_{3F3}$MIm(FH)$_{1.7}$F	27.4	21.2
C$_{4F5}$MIm(FH)$_{1.7}$F	32.9	28.2
C$_{6F9}$MIm(FH)$_{1.8}$F	38.8	30.1

Figure 7–1. Structures of (a) C_3MIm^+, (b) $C_{3F3}MIm^+$, (c) $C_{4F5}MIm^+$, (d) $C_{6F9}MIm^+$, (e) $C_{8F13}MIm^+$, and (f) $C_{10F17}MIm^+$.

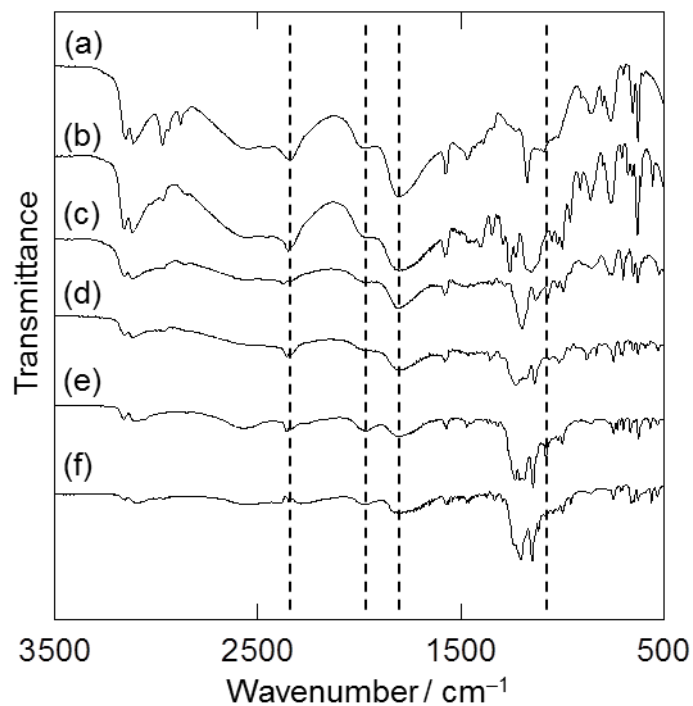Figure 7–2. Infrared spectra of (a) $C_3MIm(FH)_{1.7}F$, (b) $C_{3F3}MIm(FH)_{1.7}F$, (c) $C_{4F5}MIm(FH)_{1.7}F$, (d) $C_{6F9}MIm(FH)_{1.8}F$, (e) $C_{8F13}MIm(FH)_{2.0}F$, and (f) $C_{10F17}MIm(FH)_{2.0}F$.
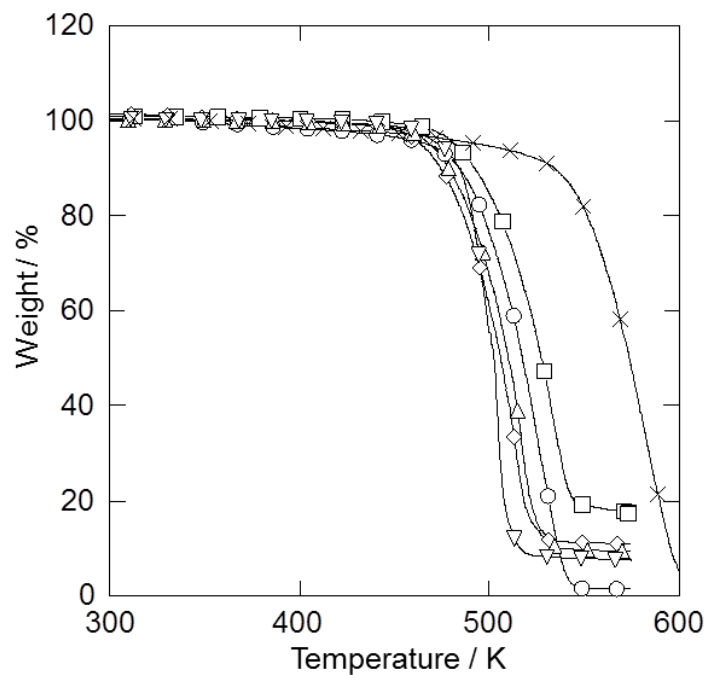
Figure 7–3. Thermogravimetric curves of $C_3MIm(FH)_{1.7}F$ ($\times$), $C_{3F3}MIm(FH)_{1.7}F$ ($\circ$), $C_{4F5}MIm(FH)_{1.7}F$ ($\square$), $C_{6F9}MIm(FH)_{1.8}F$ ($\diamond$), $C_{8F13}MIm(FH)_{2.0}F$ ($\triangle$), and $C_{10F17}MIm(FH)_{2.0}F$ ($\triangledown$).
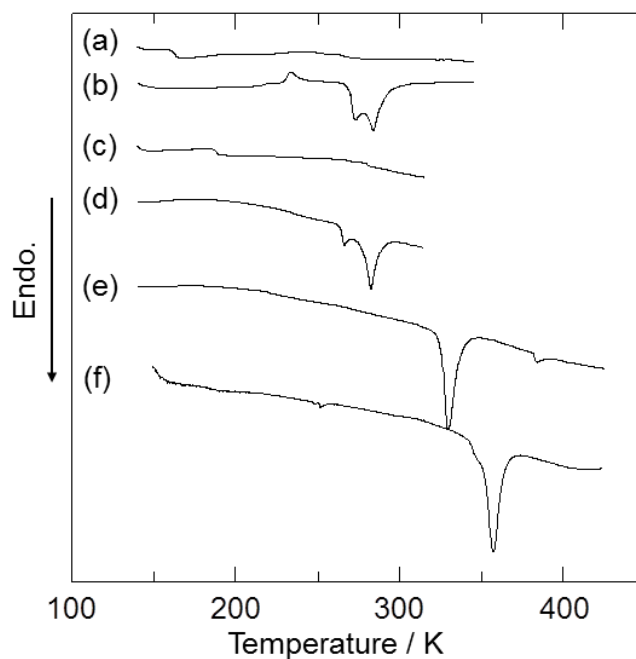
Figure 7–4. Differential scanning calorimetric curves of (a) $C_3MIm(FH)_{1.7}F$, (b) $C_{3F3}MIm(FH)_{1.7}F$, (c) $C_{4F5}MIm(FH)_{1.7}F$, (d) $C_{6F9}MIm(FH)_{1.8}F$, (e) $C_{8F13}MIm(FH)_{2.0}F$, and (f) $C_{10F17}MIm(FH)_{2.0}F$.

120
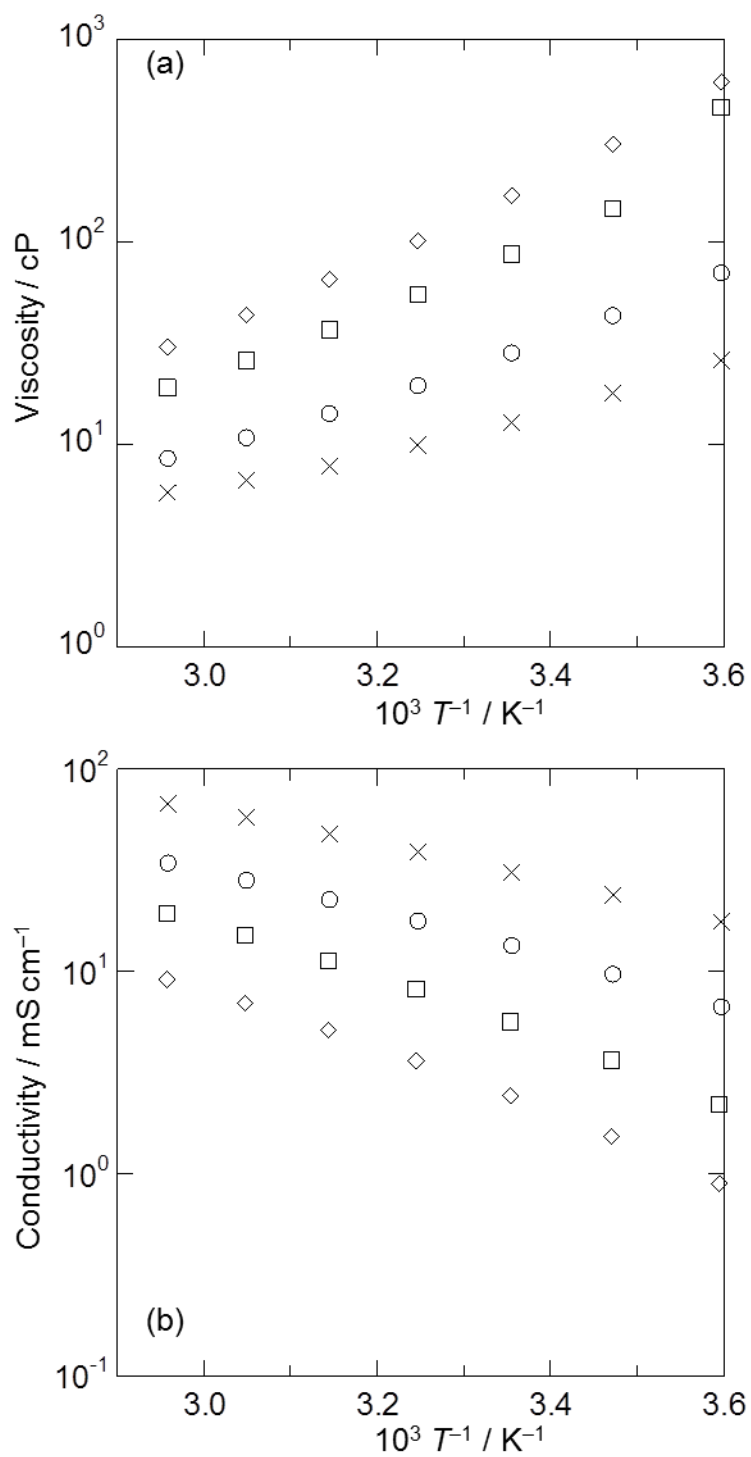
Figure 7–5. Arrhenius plots of (a) viscosity and (b) ionic conductivity for $C_3MIm(FH)_{1.7}F$ (×), $C_{3F3}MIm(FH)_{1.7}F$ (○), $C_{4F5}MIm(FH)_{1.7}F$ (□), and $C_{6F9}MIm(FH)_{1.8}F$ (◇).
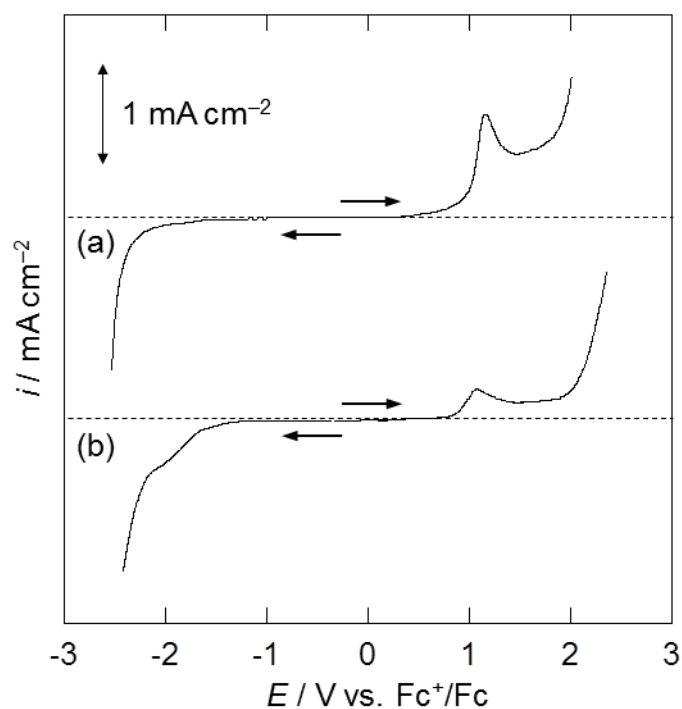
Figure 7–6. Linear sweep voltammograms of a vitreous carbon electrode in (a) $C_3MIm(FH)_{1.7}F$ and (b) $C_{3F3}MIm(FH)_{1.7}F$. Scan rate: 10 mV s^{-1}.
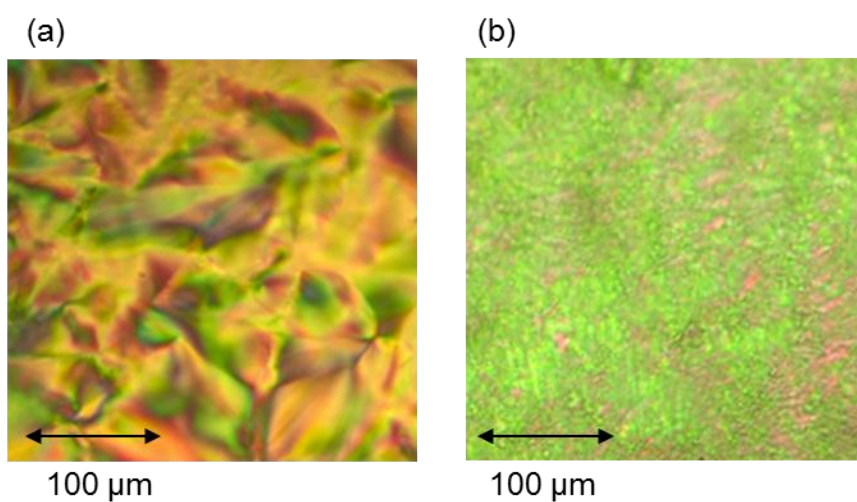

Figure 7–7. Polarized optical microscopic textures of (a) $C_{8F13}MIm(FH)_{2.0}F$ at 373 K on cooling from isotropic liquid phase and (b) $C_{10F17}MIm(FH)_{2.0}F$ at 373 K on heating from crystal phase.

122
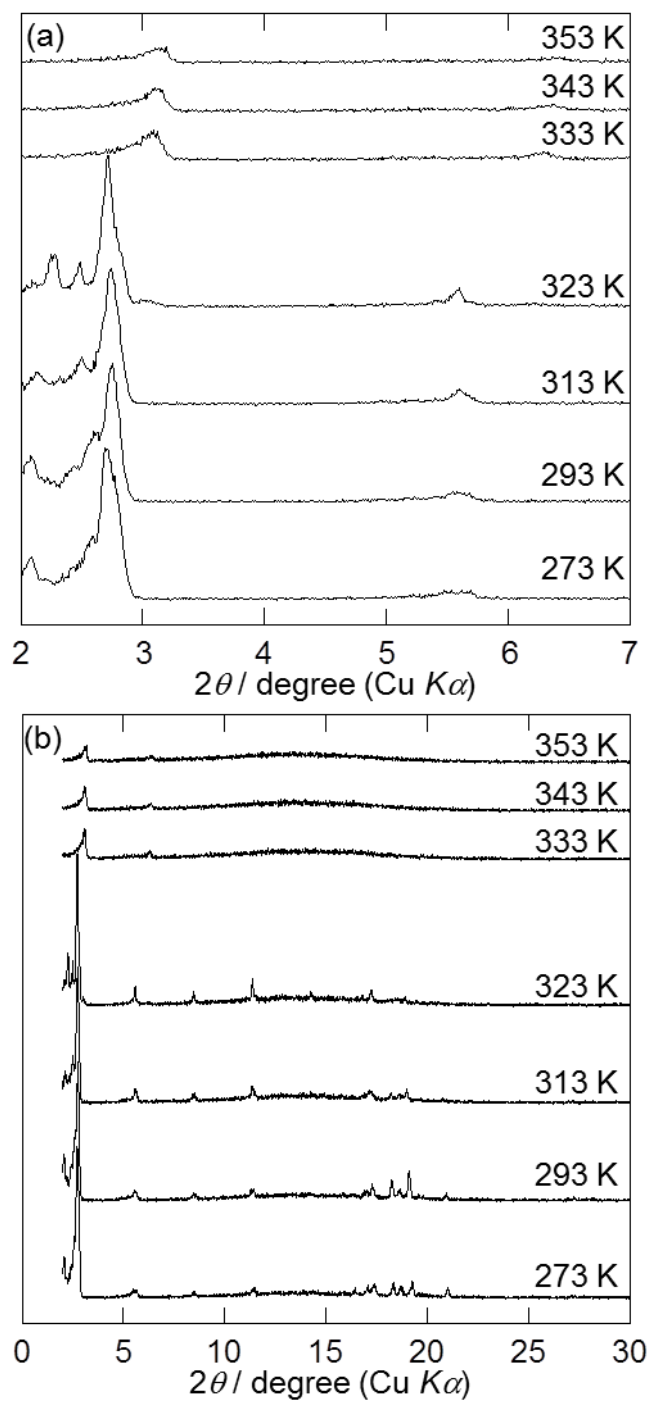
Figure 7–8. X-ray diffraction patterns in (a) the low-angle region and (b) wide-angle region for $C_{8F13}MIm(FH)_{2.0}F$ in the crystal phase (273 – 323 K) and the liquid crystal phase (333 – 353 K).

123
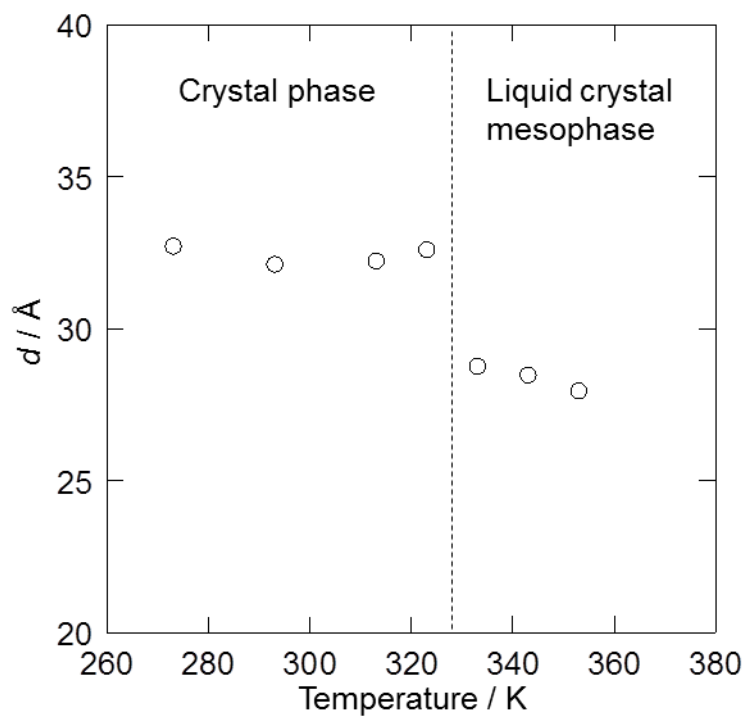
Figure 7–9. Layer spacing of $C_{8F13}MIm(FH)_{2.0}F$ in the crystal phase and liquid crystal phase at different temperatures.
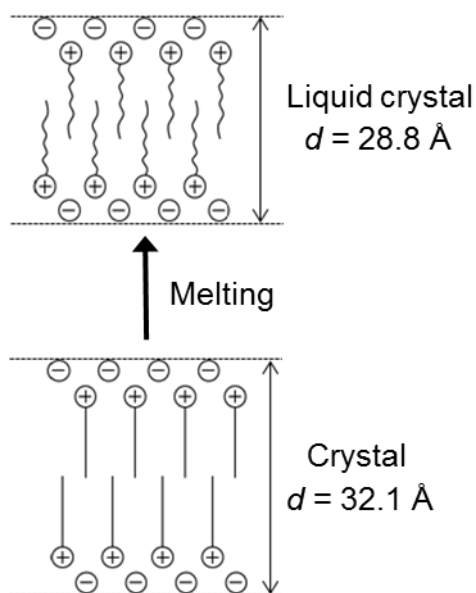

Figure 7–10. Schematic illustration of the crystal–liquid crystal phase transition of $C_{8F13}MIm(FH)_{2.0}F$.

Chapter 8

Electrochemical capacitor using fluorohydrogenate ionic liquid

8.1 Introduction

As described in Chapter 1, RTILs are attractive electrolytes as alternatives to the conventional organic and aqueous electrolytes in electrochemical devices, owing to their unique properties, including negligible vapor pressure, low-flammability, and high electrochemical stability [1–5]. Electrochemical capacitors using RTILs have performance comparable to organic electrolytes, while a drawback for conventional RTILs is their low ionic conductivity as in the cases of most organic electrolytes [4–7]. Highly conductive electrolytes offer a low internal resistance of electrochemical devices, giving a large power density, and low melting points enable an operation at low temperature (e.g., even at 233 K) [8,9]. As described in the previous chapters, FHILs exhibit high ionic conductivity and low melting points and their use leads to offer preferable characteristics for electrochemical capacitors.

Characteristics of electrochemical capacitors employing FHILs have been reported [8–10]. The capacitance of the electrochemical capacitors employing FHILs generally exhibits a large voltage dependence and is larger than that of capacitors using typical RTILs or organic electrolytes, regardless of the cationic structures. Although the redox reactions on activated carbon electrodes are involved in these phenomena, the voltage dependence is not fully understood. Thus, the purpose of the present study is to clarify the mechanism of the voltage dependence of the capacitance. Herein, the electrochemical behavior of activated carbon electrodes in FHIL EMPyr(FH)$_{2.3}$F is investigated by independently monitoring the potentials of the positive and negative electrodes during charge–discharge tests. Cyclic voltammetry and

ac impedance spectroscopy are utilized to facilitate detailed analysis. The Faradaic reaction on the positive electrode is also studied in detail using X-ray photoelectron spectroscopy.

8.2 Experimental

The galvanostatic charge–discharge tests were performed for 300 cycles at a current density of 238 mA g^{-1} for different charging voltages (0.5, 1.0, 1.5, 2.0, and 2.5 V). An alternative current density of 2380 mA g^{-1} was also used to determine the rate ability, where the cell was charged up to a voltage of 2.5 V. The charging voltages were controlled based on the difference between the potentials of the positive and negative electrodes. The CV tests were carried out at a scan rate of 0.2 mV s^{-1}. The ac impedance tests were performed at the applied ac amplitude of 10 mV using different charging voltages of 0.5, 1.0, 1.5, 2.0, 2.5, and 3.0 V within the frequency range of 10 kHz to 2 mHz. Each impedance measurement was initiated after maintaining the electrode at the target potential for 30 min.

8.3 Results and discussion

8.3.1 Cycle property

Figure 8–1 shows the capacitance of the positive and negative electrodes in EMPyr(FH)$_{2.3}$F over the course of 300 galvanostatic charge–discharge cycles between 0 and 2.5 V. The capacitance of the positive electrode decreases in the early cycles due to an irreversible electrochemical reaction. The capacitance of the negative electrode increases during the first few cycles and then gradually decreases. Although the decrease in the capacitance of the negative electrode is attributed to the irreversible reaction, the initial increase in the capacitance is probably due to activation of the electrode. A coulombic efficiency over 99% was achieved after 30 cycles, and the respective capacitances of the positive and negative electrodes at the 300th cycle were 290 and 246 F g^{-1}. Figure 8–2 shows

126

the charge–discharge curves of the positive and negative electrodes at the 300th cycle. The charge curves of both electrodes deviate from linearity because the electrodes are polarized from the rest potential. This behavior suggests that the charge is stored in the double layers in the beginning of charging and the contribution of the Faradaic reaction increases in the high voltage region. On the other hand, the discharge curves approximate linearity for both the positive and negative electrodes as in the case of normal capacitors. The applied charging voltage of 2.5 V at the maximum, which includes both the double-layer and redox capacitances, is divided into 1.15 and 1.35 V for the positive and negative electrodes, respectively, given that the capacitance of the positive electrode is higher than that of the negative electrode.

8.3.2 Redox reaction on the negative electrode in FHIL

Figure 8–3 shows the CVs of the activated carbon electrode in EMPyr(FH)$_{2.3}$F for a negative potential region (−2.0 and +0.1 V vs. Fc$^+$/Fc) corresponding to the behavior of the negative electrode. In the scan range of −2.0 and +0.1 V vs. Fc$^+$/Fc, a cathodic current due to the Faradaic reaction is observed below −1.0 V vs. Fc$^+$/Fc. In correspondence to this, an increasing anodic current is observed in the following positive scan. No clear peak is observed in the cathodic and anodic scans, and the increase in current is moderate. The redox capacitance is roughly 50% of the total capacitance (double-layer + redox capacitances as described below) in the case of charging with a voltage up to 2.5 V. Figure 8–4 shows that there was no difference in the C1s XPS spectra between the charged (potentiostatic electrolysis at −1.2 V vs. Fc$^+$/Fc for 2 h) and discharged activated carbon electrodes. One conceivable redox reaction is that involving (FH)$_n$F$^−$ and the adsorbed hydrogen atom (H$_{ad}$) as follows:

127

$$3 \ (FH)_3F^- + e^- = 4 \ (FH)_2F^- + H_{ad} \tag{8-1}$$

According to previous reports, fluorohydrogenate anions are reduced to evolve hydrogen gas with formation of HF-deficient fluorohydrogenate anions on a platinum electrode at ca. -1 V vs. Fc^+/Fc, and oxidation of hydrogen gas in $(FH)_nF^-$ was also confirmed in a fuel cell utilizing FHILs [11–13]. If the redox capacitance (116 F g^{-1} in the case of a charging voltage to 2.5 V) arises from the reduction of fluorohydrogenate anions to form diatomic hydrogen, the theoretical volume of gas evolved is calculated to be ~15 mL $(g\text{-}C)^{-1}$ which exceeds the storage capacity of the activated carbon. Consequently, it is postulated that atomic hydrogen is generated in the reaction and is adsorbed by the activated carbon. The redox reaction involving surface functional groups on the activated carbon is also a possible reaction. Figure 8–2 illustrates that the potential of the negative electrode reaches -1.2 V vs. Fc^+/Fc in the charge–discharge test when the cell voltage is 2.5 V, where the redox capacitance is observed in addition to the double-layer capacitance as shown in Figure 8–3.

8.3.3 Redox reaction on the positive electrode in FHIL

Figure 8–5 shows the CVs of the activated carbon electrode in $EMPyr(FH)_{2.3}F$ for positive potential regions (-0.8 and $+1.7$ V vs. Fc^+/Fc) corresponding to the behavior of the positive electrode. Another Faradaic reaction is observed in the potential range above $+0.4$ V vs. Fc^+/Fc in the positive scan. The oxidation current decreases above $+1.5$ V vs. Fc^+/Fc and the difference in the anodic and cathodic peak potentials becomes larger as the reversal potential increases. A low coulombic efficiency of 90% is observed for the reversal potential of $+1.7$ V vs. Fc^+/Fc compared to that of 97% achieved at $+1.5$ V vs. Fc^+/Fc. As is shown in Figure 8–2, the potential of the positive electrode reaches $+1.3$ V vs. Fc^+/Fc in the charge–discharge test for the cell voltage of 2.5 V, where the Faradaic reaction has a significant

contribution to the total capacitance. This Faradaic behavior of the activated carbon is unique to the EMPyr(FH)$_{2.3}$F-containing cell and possibly results from the electrochemical reaction involving fluorohydrogenate anions. The reaction occurring above +0.4 V vs. Fc$^+$/Fc was further investigated by XPS analysis of the activated carbon electrodes in three different states, i.e., pristine, charged (potentiostatic electrolysis at +1.2 V vs. Fc$^+$/Fc for 2 h), and discharged states. Figure 8–6 shows the C1s and F1s XPS spectra of the three electrodes. No peaks attributable to the electrolyte or PTFE are observed in the N1s and O1s XPS spectra in Figure 8–7. No peak shift or new peaks are observed in the C1s spectrum of the charged electrode compared to the pristine sample, whereas a new peak is clearly apparent in the F1s spectrum of the charged electrode and almost disappears in that of the discharged electrode. Formation of a strong C–F bond such as in fluorinated graphite ($(CF)_n$) is ruled out on the basis of the C1s XPS spectrum of the charged electrode where no peaks are observed in the region above 290 eV. A possible model for the present Faradaic reaction is presented in Figure 8–8 and involves absorption of F$^-$ or FHF$^-$ in the grain boundary or between insufficiently grown carbon layers. A conceivable redox reaction for this system is as follows:

$$C_m + 3 \; (FH)_2F^- = C_m{}^+(F^-) + 2 \; (FH)_3F^- + e^- \tag{8–2}$$
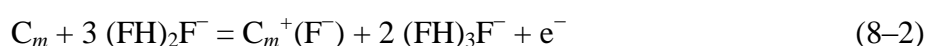
where $C_m{}^+(F^-)$ denotes the oxidized carbon accompanied by absorption of F$^-$. Although intercalation of anions into a graphite electrode occurs to form graphite intercalation compounds [14,15], the one into an activated carbon electrode is not known. This is due to the turbostratic structure of activated carbon composed of microcrystalline domains. In the present case, the small F$^-$ or $(FH)_nF^-$ is considered to be stored in a space such as a micro pore in the activated carbon, which is similar to the p-doping process. The amount of absorbed fluorine atom at the surface of the activated carbon electrode was estimated to be

$C_{1.0}F_{0.082}$ by the C1s and F1s spectra. Although only the surface was observed in the XPS analysis, this ratio of fluorine to carbon strongly suggests the existence of the absorbed fluorine atom according to the redox capacitance in the charge-discharge test. Reduction of this oxidized form occurs in the following cathodic scan with a certain coulombic efficiency. Consequently, both of the two Faradaic reactions (eqs. (8–1) and (8–2)) contribute to the large voltage dependence of the capacitance for the electrochemical capacitors combining activated carbon electrodes and $EMPyr(FH)_{2.3}F$. In the case of other FHILs, the reported dependence of the capacitance on the charging voltage suggests that the same charge–discharge mechanism is operative as in the present study [8–10].

8.3.4 Impedance analysis

Figure 8–9 shows the voltage dependence of the capacitances for (a) the positive and (b) the negative electrodes at different charging voltages (0.5, 1.0, 1.5, 2.0, and 2.5 V) during 300 charge–discharge cycles. The resulting positive and negative capacitances at the 300th cycle are summarized in Table 8–1. The contributions of the double-layer and redox capacitances were evaluated by means of ac impedance measurements. Figure 8–10 shows the Nyquist plots for the impedance spectra of the activated carbon positive and negative electrodes in $EMPyr(FH)_{2.3}F$ at the various charging voltages (i.e., the voltage between the positive and negative electrodes: 0.5, 1.0, 1.5, 2.0, 2.5, and 3.0 V). At 0.5 V, the Nyquist plots for both of the electrodes exhibit typical behavior of double-layer capacitors under a transmission model which is characterized by a slope with a phase angle of −45° in the high frequency range and a locus in parallel with the imaginary axis in the low frequency range (Figure 8–10 (a)) [16]. As the charging voltage increases (Figure 8–10 (b) and (c)), the slope of the straight line in the low frequency region gradually becomes steeper, which indicates an increase in the contribution of the Faradaic reaction under the transmission model [16]. The double-layer

capacitances of the positive and negative electrodes were calculated from the frequency and imaginary component of the impedance spectra at 0.5 V using the equation $C = 1/2\pi f Z_{im} w$, where f and Z_{im} denote the frequency and imaginary component of the obtained impedance, respectively. The obtained values are 150 F g^{-1} for the positive electrode and 140 F g^{-1} for the negative electrode (Table 8–1). These values contain the contribution only from the double-layer capacitance and are similar to the capacitances obtained in the charge–discharge test up to 0.5 V. The positive capacitance is higher than the negative capacitance, conceivably due to the smaller size of the anion relative to that of the cation.

8.3.5 Quantitative evaluation of the double-layer and redox capacitance

In the charge–discharge test shown in Figure 8–9, the cell charged at low voltage exhibits only the double-layer capacitance during operation, whereas the cell charged at a higher voltage shows both the double-layer and redox capacitances. The value of the redox capacitance for each electrode is calculated by subtracting the double-layer capacitance from the total capacitance under the assumption that the double-layer capacitance obtained at 0.5 V remains the same at higher charging voltages. The obtained redox capacitances are given in Table 8–1 and Figure 8–11. The redox capacitance of the positive electrode is larger than that of the negative electrode, and this trend is more prominent at higher voltages, suggesting that charge storage via the Faradaic reaction is more efficient at the positive electrode than at the negative electrode.

8.3.6 Characteristics of the capacitance at a high rate

Figure 8–12 shows the capacitances obtained in the galvanostatic charge–discharge test for 300 cycles at a large current density of 2380 mA g^{-1} to 2.5 V. At the 300th cycle, the capacitances of the positive (188 F g^{-1}) and negative electrode (176 F g^{-1}) were 64.8% and

71.5% of those obtained at the current density of 238 mA g^{-1}, respectively (Table 8–1). At the high charge–discharge rate, the redox reaction is inefficient due to the slower kinetics of the redox reaction relative to double-layer charging. It is, however, worth mentioning that the observed capacitances at 2380 mA g^{-1} are still higher than that of the double-layer capacitors utilizing conventional RTILs.

References

[1] T. Welton, *Chem. Rev.* **1999**, *99*, 2071.

[2] R. Hagiwara, Y. Ito, *J. Fluorine Chem.* **2000**, *105*, 221.

[3] T. Tsuda, C. L. Hussey, *Electrochem. Soc. Interface* **2007**, *Spring*, 42.

[4] T. Sato, G. Masuda, K. Takagi, *Electrochim. Acta* **2004**, *49*, 3603.

[5] S. Shiraishi, T. Miyauchi, R. Sasaki, N. Nishina, A. Oya, R. Hagiwara, *Electrochemistry* **2007**, *75*, 619.

[6] N. Handa, T. Sugimoto, M. Yamagata, M. Kikuta, M. Kono, M. Ishikawa, *J. Power Sources* **2008**, *185*, 1585.

[7] S. I. Fletcher, F. B. Sillars, R. C. Carter, A. J. Cruden, M. Mirzaeian, N. E. Hudson, J. A. Parkinson, P. J. Hall, *J. Power Sources* **2010**, *195*, 7484.

[8] M. Ue, M. Takeda, A. Toriumi, A. Kominato, R. Hagiwara, Y. Ito, *J. Electrochem. Soc.* **2003**, *150*, A499.

[9] A. Senda, K. Matsumoto, T. Nohira, R. Hagiwara, *J. Power Sources* **2010**, *195*, 4414.

[10] K. Matsumoto, K. Takahashi, A. Senda, T. Nohira, R. Hagiwara, *ECS Trans.* **2010**, *33*, 421.

[11] S. Kanematsu, K. Matsumoto and R. Hagiwara, *Electrochem. Commun.* **2009**, *11*, 1312.

[12] T. Enomoto, S. Kanematsu, K. Tsunashima, K. Matsumoto and R. Hagiwara, *Phys. Chem. Chem. Phys.* **2011**, *13*, 12536.

[13] R. Hagiwara, T. Nohira, K. Matsumoto and Y. Tamba, *Electrochem. Solid-State Lett.* **2005**, *8*, A231.

[14] T. Ishihara, M. Koga, H. Matsumoto, M. Yoshio, *Electrochem. Solid-State Lett.* **2007**, *10*, A74.

[15] W. C. West, J. F. Whitacre, N. Leifer, S. Greenbaum, M. Smart, R. Bugga, M. Blanco, S. R. Narayanan, *J. Electrochem. Soc.* **2007**, *154*, A929.

[16] M. Itagaki, S. Suzuki, I. Shitanda, K. Watanabe and H. Nakazawa, *J. Power Sources* **2007**, *164*, 415.

Table 8–1. The positive and negative capacitances obtained in charge–discharge (C–D) tests to different charging voltages and the ac impedance test at 0.5 V.

Charging voltage / V	Positive capacitance / F g^{-1}		Negative capacitance / F g^{-1}	
	Total[a]	Redox[a]	Total[a]	Redox[a]
0.5 (Impedance test)	150	0	140	0
0.5 (C–D test, 238 mA g^{-1})	140	0	130	0
1.0 (C–D test, 238 mA g^{-1})	157	17	147	17
1.5 (C–D test, 238 mA g^{-1})	195	55	160	30
2.0 (C–D test, 238 mA g^{-1})	256	116	203	73
2.5 (C–D test, 238 mA g^{-1})	290	150	246	116
2.5 (C–D test, 2380 mA g^{-1})	188	–	176	–

[a]The total capacitances (double-layer capacitance + redox capacitance) were obtained from the relation $C = It/wV$. The redox capacitances were obtained under the assumption that the double-layer capacitance at 0.5 V (C–D test, 238 mA g^{-1}) does not change at the other voltages. The capacitances in the impedance test are slightly higher than those in the charge–discharge test because the impedance tests were performed under static conditions without a current flow and the charge–discharge tests were performed under dynamic conditions with a current flow of 238 mA g^{-1}.
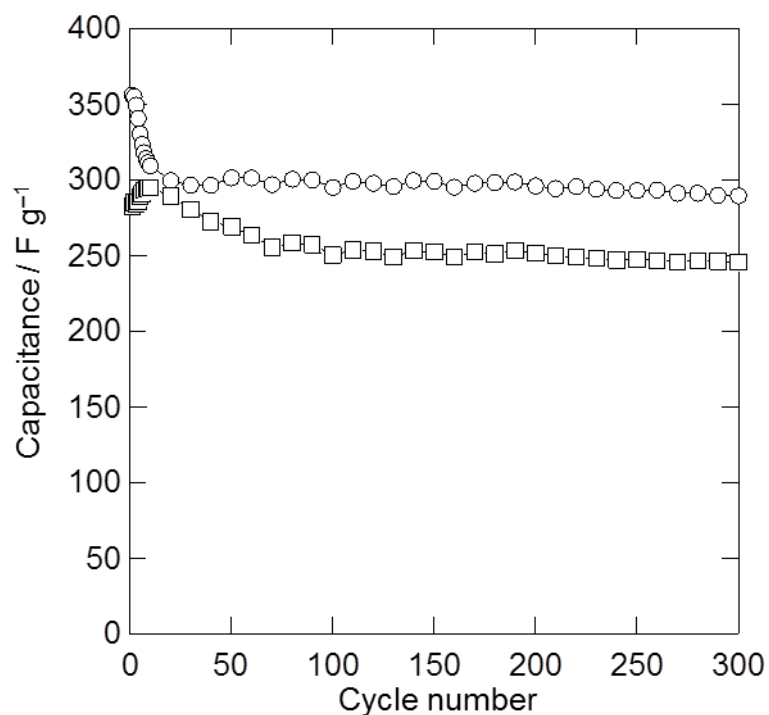
Figure 8–1. Discharge capacitance of the activated carbon positive (○) and negative (□) electrodes in EMPyr(FH)$_{2.3}$F over 300 charge–discharge cycles at a current density of 238 mA g^{-1}.
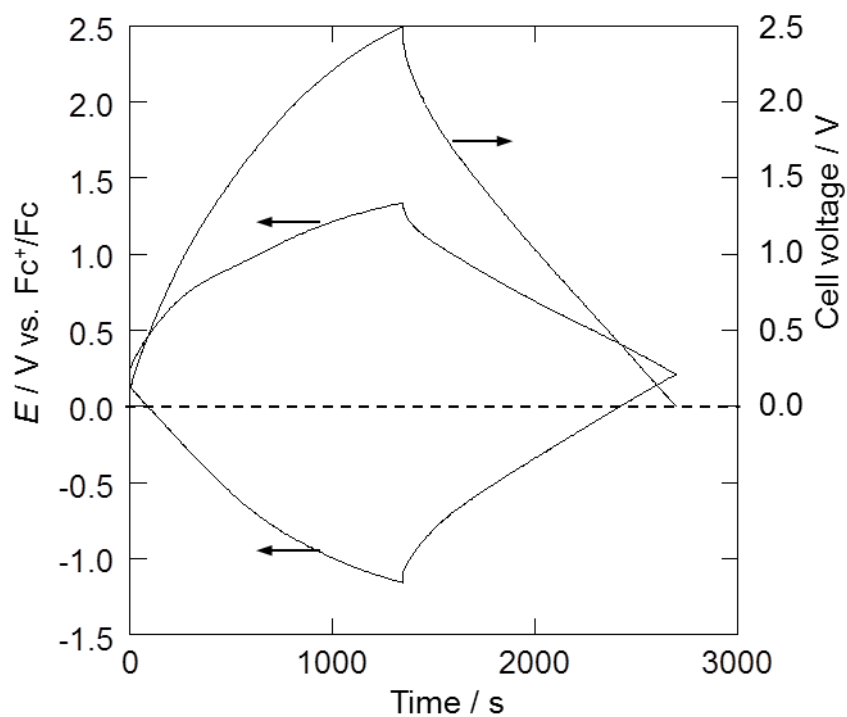

Figure 8–2. Charge–discharge curves of the cell, and activated carbon positive and negative electrodes in EMPyr(FH)$_{2.3}$F at the 300th cycle.
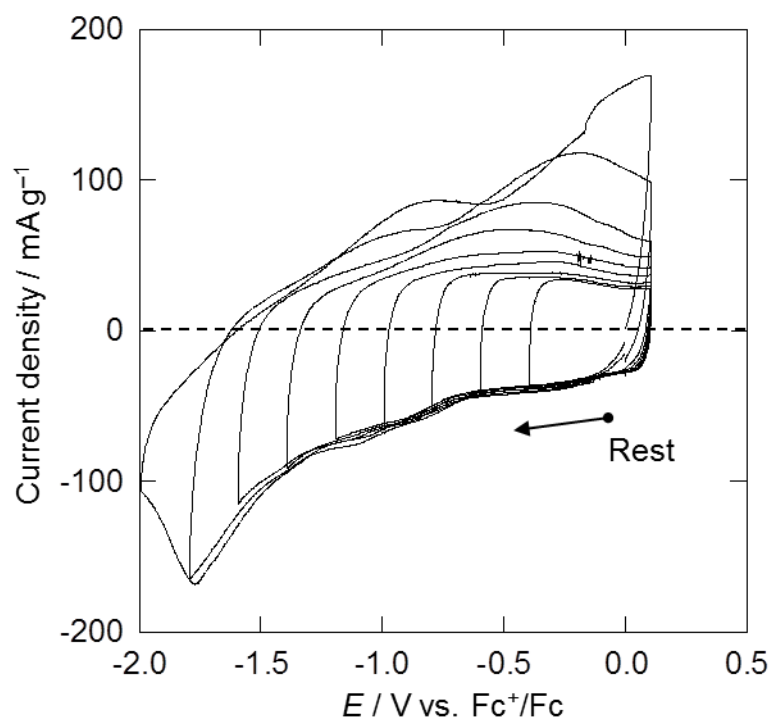
Figure 8–3. Cyclic voltammograms of an activated carbon electrode in EMPyr(FH)$_{2.3}$F. Scan range between −2.0 and +0.1 V vs. Fc$^+$/Fc. WE: Activated carbon. Scan rate: 0.2 mV s^{-1}.
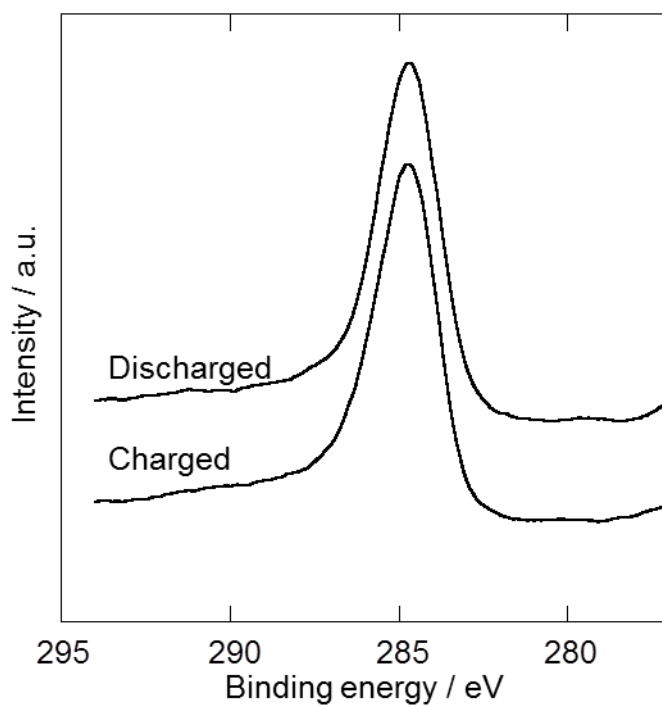
Figure 8–4. The C1s spectra of the two electrodes: charged (potentiostatic electrolysis at −1.2 V vs. Fc$^+$/Fc for 2 h) and discharged activated carbon negative electrodes.
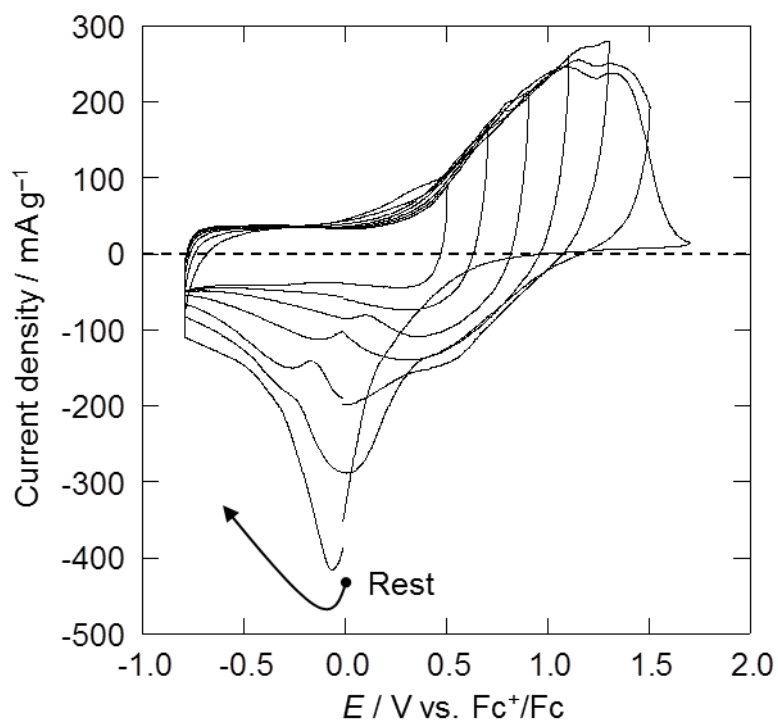
137

Figure 8–5. Cyclic voltammograms of an activated carbon electrode in EMPyr(FH)$_{2.3}$F. Scan range between −0.8 and +1.7 V vs. Fc$^+$/Fc. WE: Activated carbon. Scan rate: 0.2 mV s^{-1}.
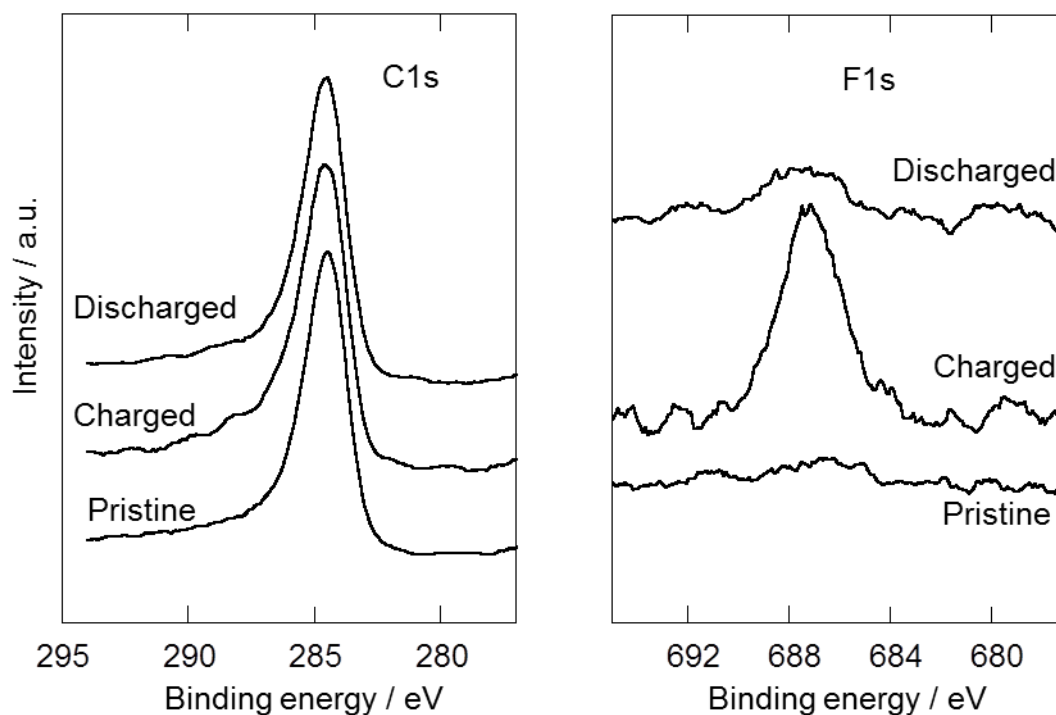

Figure 8–6. The C1s and F1s XPS spectra of the three electrodes: pristine, charged (potentiostatic electrolysis at +1.2 V vs. Fc$^+$/Fc for 2 h), and discharged activated carbon positive electrodes.
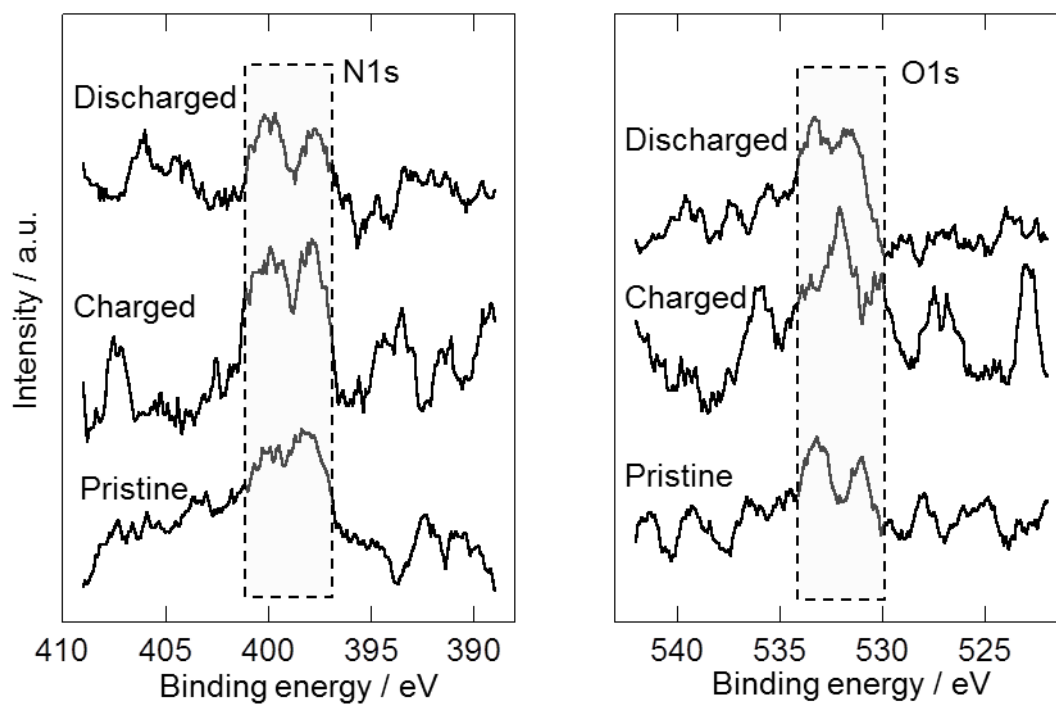
138

Figure 8–7. The N1s and O1s XPS spectra of the three electrodes: pristine, charged, and discharged activated carbon positive electrodes.
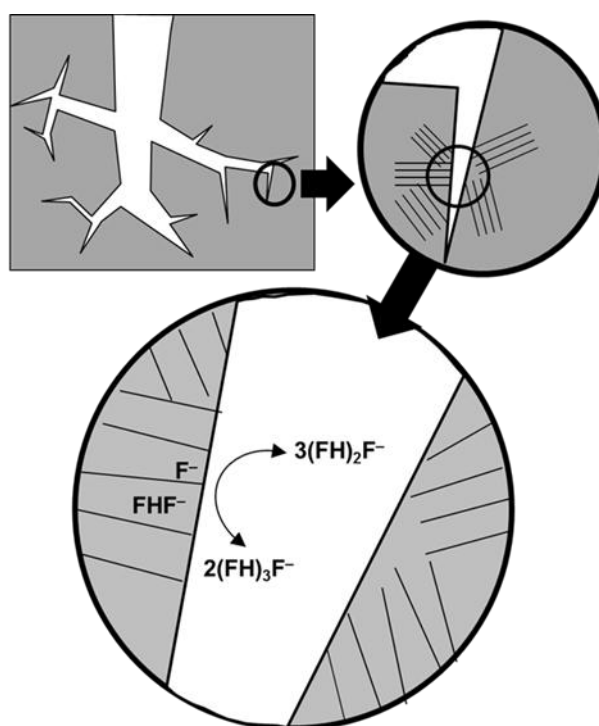

Figure 8–8. Schematic model of the Faradaic reaction for the activated carbon electrode in EMPyr(FH)$_{2.3}$F in the high voltage range (> 0.4 V vs. Fc$^+$/Fc).
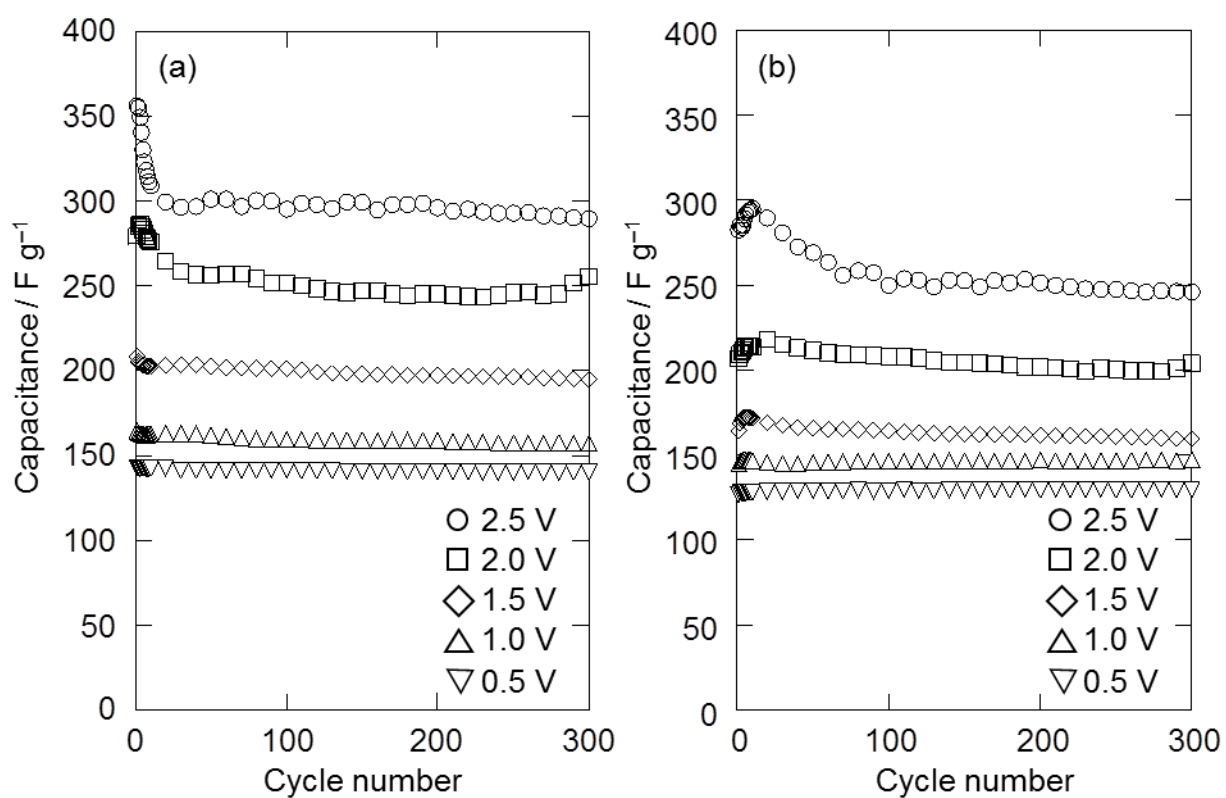
Figure 8–9. Discharge capacitances of the activated carbon (a) positive electrode and (b) negative electrode in EMPyr(FH)$_{2.3}$F for various charging voltages.
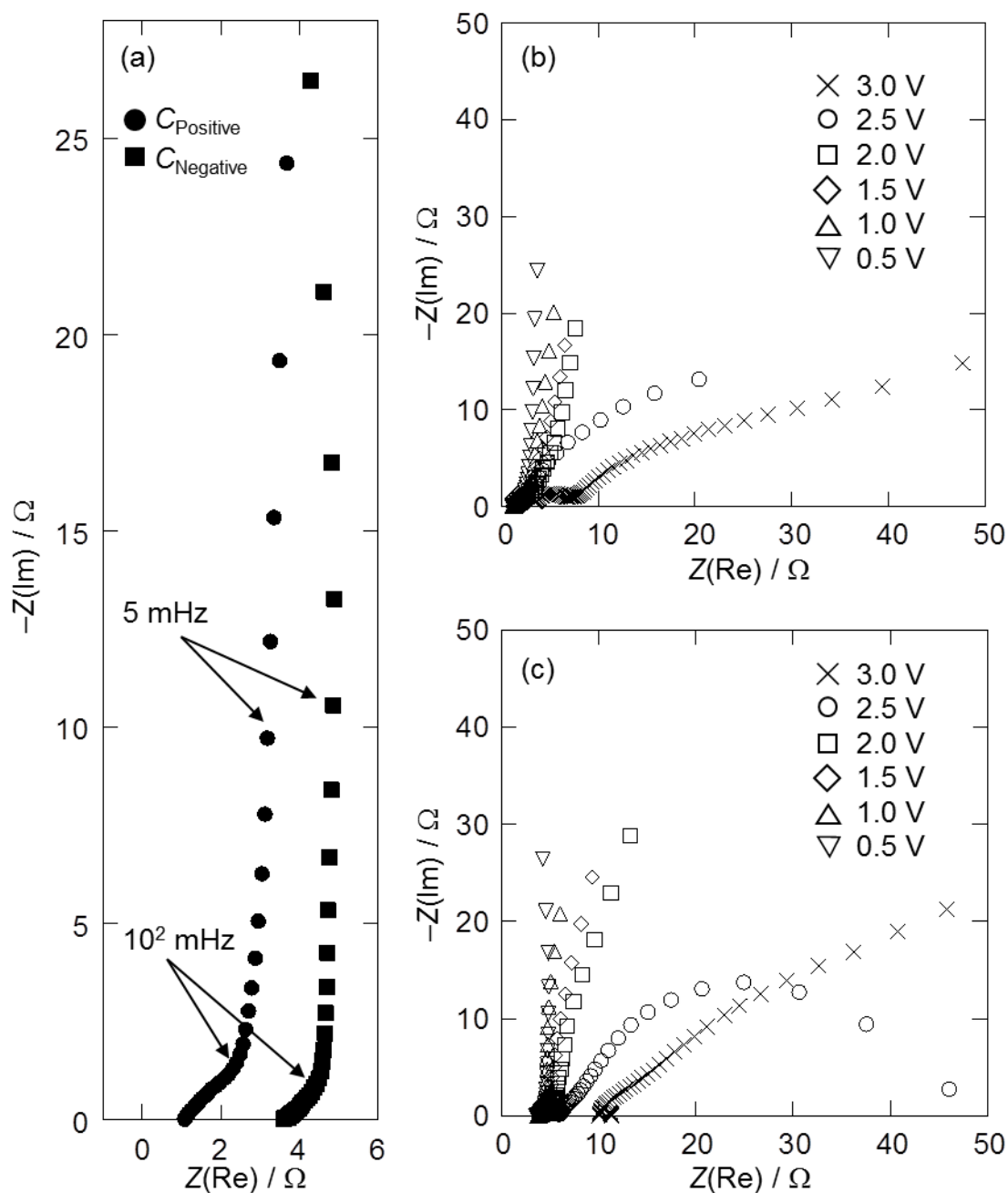
Figure 8–10. Nyquist plots of the impedance spectra for the activated carbon positive and negative electrodes in EMPyr(FH)$_{2.3}$F: (a) plots for the positive and negative electrodes at 0.5 V, (b) plots for the positive and (c) negative electrodes at different charging voltages. The frequency ranges from 10 kHz to 2 mHz.
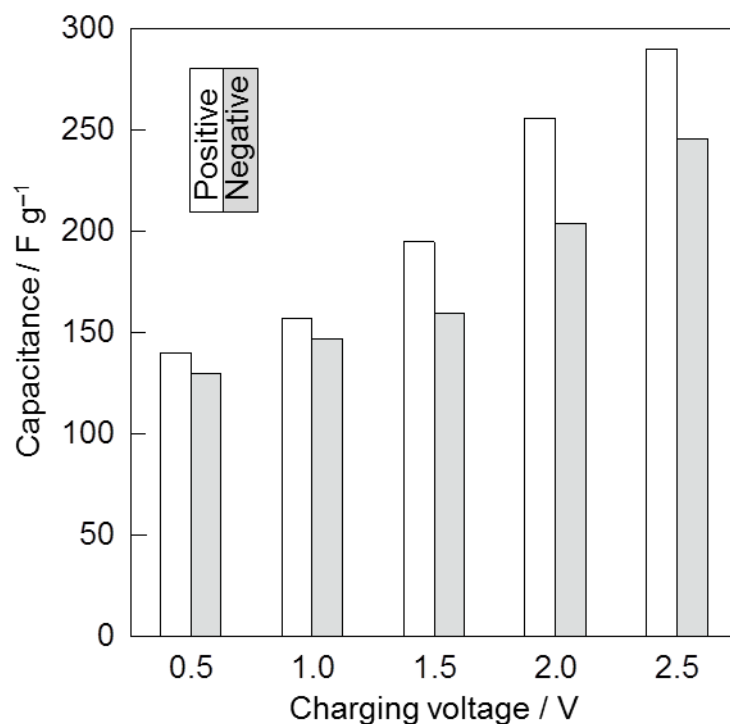
Figure 8–11. Capacitances of the activated carbon positive and negative electrodes in EMPyr(FH)$_{2.3}$F at the 300th cycle for various charging voltages. Current density: 238 mA g^{-1}.
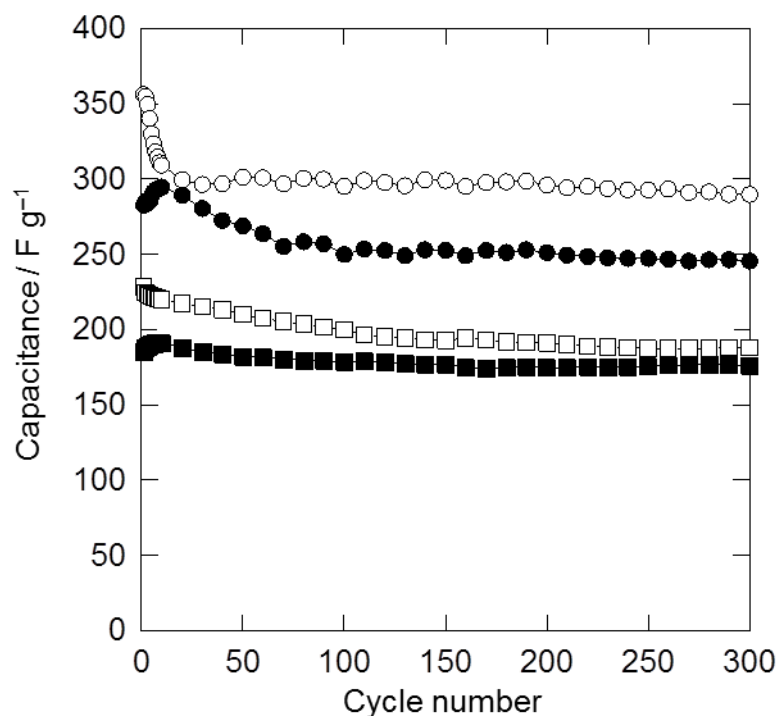

Figure 8–12. Discharge capacitances of the activated carbon positive (○: 238 mA g^{-1} and □: 2380 mA g^{-1}) and negative (●: 238 mA g^{-1} and ■: 2380 mA g^{-1}) electrodes in EMPyr(FH)$_{2.3}$F.

Chapter 9

Electrochemical capacitor using fluorohydrogenate ionic plastic crystal

9.1 Introduction

Many liquid electrolytes have been used in electrochemical devices, whereas solid electrolytes are limited. Replacement of liquid electrolytes to solid electrolytes offers leakage of electrolytes, flexible and thin configuration of electrochemical devices, volumetric stability during the cell operation, and easy packing and handling [1–4]. Polymer electrolytes are used as solid electrolytes because they have preferable features as solid electrolytes described above. They are roughly classified into dry solid polymer electrolytes and gel polymer electrolytes [1,2,5–8].

A dry solid polymer electrolyte uses a polymer host as a solid solvent and does not contain organic liquids, which are utilized mainly for lithium battery. In the dry solid electrolyte such as poly(ethylene oxide) (PEO), cations are coordinately bonded and stored to the polymer host, while anions are stored outside the helix of the PEO chain [7,8]. The cations, captured in the polymer host, migrate by the segmental motion of the polymer chain, which leads to the long range mobility of the cations. The ionic conductivity of the PEO–LiClO$_4$ dry polymer electrolyte is 10^{-5} mS cm^{-1} at 293 K [8]. The ionic conductivity is improved by designing the polymer host, whereas the designed linear and branched polymer suffers from poor mechanical stability. Introduction of functional group (e.g., sulfonate group) sometimes achieves high ionic conductivity and good mechanical stability [9]. The polymer host needs several factors such as (1) sequential functional groups with high electron donating or withdrawing ability to form coordinate bonds to cations or anions, (2) an appropriate distance

between such the functional groups with coordinating center to form multiple intrapolymer–ion bonds, and (3) a low steric barrier to bond rotations so as to facilitate the segmental motions [1,5].

Gel polymer electrolytes are mixed with the polymer host, solvent, and salt where the polymer host acts simply as a stiffener for the low molecular weight solvent which operates as a medium for the mobility of cationic and anionic species [5,8]. Gel polymer electrolytes exhibit cohesive properties of solids and diffusive properties of liquids. Polymer hosts, such as PEO, poly(vinylidene fluoride), poly(acrylonitrile), and poly(vinyl chloride) have been utilized [3,8,10–15]. Organic solvents, such as ethylene carbonate, propylene carbonate, tetrahydrofuran, γ-butyrolactone, and dimethylcarbonate have been employed as plasticizers in gel polymer electrolytes [16,17]. The glass transition temperature of gel polymer electrolytes changes with the proportion of polymer and plasticizer. Ionic conductivities of typical polymer electrolytes utilizing aqueous and organic solvents range between 10^0–10^1 mS cm^{-1} and 10^{-1} – 10^0 mS cm^{-1}, respectively [1,3,8,18,19]. These values are lower than those of liquid electrolytes by an order of magnitude. As described in Chapter 1, RTILs have some unique properties and are also used as a plasticizer instead of organic solvents [20–23], although flammability of the polymer remains and the merit using RTILs diminishes.

Ionic plastic crystals are interesting candidates as solid electrolytes due to their properties described in Chapters 1 and 3, whereas there is no report on utilization of IPCs as solid electrolytes for electrochemical capacitors because the low ionic conductivity of typical IPCs cannot offer a low internal resistance of electrochemical capacitors. Fluorohydrogenate ionic plastic crystals are desirable as solid electrolytes for electrochemical capacitors due to their highly ionic conductivity described in Chapters 3 and 4. In addition, the capacitance of electrochemical capacitors employing FHILs generally has a large voltage dependence and is higher than those of capacitors using typical RTILs or organic electrolytes. This results from

the redox reactions on activated carbon electrode involving fluorohydrogenate anions as described in Chapter 8. Replacement of electrolytes for electrochemical capacitors from FHILs to FHIPCs has a potential to keep the large capacitance and gives the above-mentioned properties as the solid electrolyte. This chapter describes the behavior of the activated carbon electrode in the FHIPC DMPyr(FH)$_2$F.

9.2 Experimental

The galvanostatic charge–discharge tests were performed in a three-electrode cell for 300 cycles at different current densities of 238, 476, and 2380 mA g^{-1}, where the cell was charged up to a voltage of 2.5 V. The charging voltages were controlled based on the voltage between the positive and negative electrodes. The CV tests were carried out in a three-electrode cell at a scan rate of 0.2 mV s^{-1}, using activated carbon working and counter electrodes and the Ag quasi reference electrode. The ac impedance tests were performed in the two-electrode cell at the applied ac amplitude of 10 mV within the frequency range of 10 kHz to 2 mHz. The self-discharge tests were performed by monitoring the cell voltage for 24 h after charging up to 1.0 V at 238 mA g^{-1} in a two-electrode cell. For comparison of the results on the impedance tests and self-discharging tests, the FHIL EMPyr(FH)$_{2.3}$F and typical RTIL EMImBF$_4$ were utilized. Electrodes were impregnated with DMPyr(FH)$_2$F under vacuum above its melting point. For the other liquid electrolytes, electrodes were impregnated under vacuum at room temperature.

9.3 Results and discussion

9.3.1 The double-layer formations and redox reactions on activated carbon electrodes in FHIPC

Figure 9–1 shows the CVs of the activated carbon electrode in the IPC phase of

DMPyr(FH)$_2$F for a negative potential region between -1.6 and $+0.5$ V vs. Ag QRE. In the narrowest potential sweep region, a square shape corresponding to the formation and deformation of the electric double-layer is observed. In this region, more DMPyr$^+$ cations are present on the surface of the activated carbon electrode than $(FH)_nF^-$ anions are. As shown in Chapter 3, only $(FH)_nF^-$ works as charge carrier in the IPC phase and the long-scale migration of DMPyr$^+$ cations would not occur. A plausible explanation about the double-layer formation in this potential region is that $(FH)_nF^-$ around the surface of the activated carbon negative electrode migrates toward the positive electrode and DMPyr$^+$ comes close shortly to the surface of activated carbon by exchanging itself with anions. A cathodic current due to the Faradaic reaction is observed below -0.6 V vs. Ag QRE. In correspondence to this, an increase in anodic current is observed in the following anodic scan (coulombic efficiency of 97% when the reverse potential is -1.6 V vs. Ag QRE). In this potential range, electrochemical behavior of the activated carbon electrode in the IPC phase of DMPyr(FH)$_2$F is similar to that of the FHIL EMPyr(FH)$_{2.3}$F, and thus the redox reaction in the IPC phase of DMPyr(FH)$_2$F would involve the reduction of $(FH)_nF^-$ and the adsorption of atomic hydrogen to the activated carbon (see Chapter 8 in detail).

Figure 9–2 shows the CVs of the activated carbon electrode in the IPC phase of DMPyr(FH)$_2$F for a positive potential region between 0 and $+1.9$ V vs. Ag QRE. When the potential sweep is reversed at 0.5 V vs. Ag QRE, a square shape corresponding to the formation and deformation of the double-layer is observed. As the self-diffusion coefficient of the anion of DMPyr(FH)$_2$F in the IPC phase is 3.44×10^{-7} cm^2 s^{-1} at 298 K as shown in Chapter 3, $(FH)_nF^-$ diffuses to adsorb to the electrode during the anodic can. An anodic current due to another Faradaic reaction is observed above $+0.7$ V vs. Ag QRE. The corresponding cathodic current is observed in the following cathodic scan (coulombic efficiency of 93% when the reverse potential is 1.1 V vs. Ag QRE). As in the case of

electrochemical capacitors utilizing the FHIL EMPyr(FH)$_{2.3}$F, the redox reaction in the IPC phase of DMPyr(FH)$_2$F involves the oxidation of carbon accompanied by absorption of (FH)$_n$F$^-$ or F$^-$ into the activated carbon species (see Chapter 8).

9.3.2 Galvanostatic charge–discharge characteristics

Figure 9–3 shows cycle properties of electrochemical capacitors utilizing DMPyr(FH)$_2$F in the galvanostatic charge–discharge test performed up to the voltage of 2.5 V with a current density of 238 mA g^{-1} for 300 cycles. Stable operation of the electrochemical capacitor using FHIPCs was confirmed during this test. During the starting three cycles, the charge capacitances for the positive and negative electrodes are much higher than the discharge capacitances. The respective coulombic efficiencies at the 1st, 2nd, and 3rd cycles are 65.7, 86.6, and 90.7% for the positive electrode, and 83.4, 91.8, and 94.5% for the negative electrode, whereas they are improved to 99.1 and 98.9% for the positive and negative electrodes at the 20th cycle, respectively. The low coulombic efficiencies during the first few cycles are probably due to the irreversible redox reactions between the anions and activated carbon. After 20 cycles, the coulombic efficiency exceeded 99%, and the capacitances of the positive and negative electrodes at the 300th cycle were 263 and 221 F g^{-1}, respectively. Electrochemical capacitors using FHIL EMPyr(FH)$_{2.3}$F in Chapter 8 showed the capacitances of the positive and negative electrodes at the 300th cycle were 290 and 246 F g^{-1}, respectively. Although the replacement of the electrolytes from FHIL to FHIPC slightly decreases the capacitance, the values obtained for FHIPC are still large compared to the case of a typical ionic liquid EMImBF$_4$ (168 F g^{-1}, single-electrode capacitance calculated from the cell capacitance in ref. 24). Figure 9–4 shows the charge–discharge curves of the cell, and activated carbon positive and negative electrodes in DMPyr(FH)$_2$F at the 1st, 10th, and 300th cycles. The potentials of the positive and negative electrodes reach +1.0 and −1.5 V vs. Ag

QRE in the charge–discharge test when the cell voltage is charged to 2.5 V, where both the Faradaic reactions occur as observed in Figures 9–1 and 9–2. The redox reactions in addition to the double-layer capacitances contribute to the large capacitances obtained in the galvanostatic charge–discharge test.

Figure 9–5 shows the capacitances obtained in the galvanostatic charge–discharge test for 300 cycles at different current densities of 238, 476, and 2380 mA g^{-1} to 2.5 V. The different behavior of the positive and negative capacitances during the first 10 cycles is presumably due to the irreversible electrochemical reactions, penetration of electrolytes, and activation of carbon electrode on the negative electrode. The respective capacitances at large current densities of 476 and 2380 mA g^{-1} at the 300th cycle were 215 and 115 F g^{-1} for the positive capacitance, and 199 and 79 F g^{-1} for the negative capacitance.

9.3.3 The electrolyte resistance in the pore of activated carbon electrode

By means of an ac impedance analysis, the electrolyte resistances are separated into the ones in the bulk (R_{bulk}) and the pore (R_{pore}) of the activated carbon electrode. The R_{pore} means the electrolyte resistance from the top to bottom of the pore, which is reflected by ionic conductivity of electrolytes. A transmission model of the porous electrode shows that a typical behavior of double-layer capacitors is characterized in Figure 9–6 (a) by a Nyquist plot where a slope with a phase angle of –45° (eq. 9–1) in the high frequency range and a locus in parallel with the imaginary axis (eq. 9–2) in the low frequency range [25,26].

$$Z = R_{bulk} + \left(R_{pore}/2\omega C_{dl}\right)^{1/2}(1-j) \qquad 9–1$$

$$Z = R_{bulk} + R_{pore}/3 - j/\omega C_{dl} \qquad 9–2$$

where Z, ω, C_{dl}, and j denote impedance, angular frequency, double-layer capacitance, and imaginary unit, respectively. Figures 9–6 (b) and (c) show Nyquist plots of impedance spectra for electrochemical capacitors utilizing FHIPC DMPyr(FH)$_2$F, FHIL EMPyr(FH)$_{2.3}$F, and the

typical RTIL EMImBF$_4$ with ionic conductivity of 10.3, 74.6, and 13 mS cm^{-1} at room temperature, respectively [27–29]. The R_{bulk} and R_{pore} are 2.4 and 26.6 Ω for DMPyr(FH)$_2$F, 1.3 and 6.6 Ω for EMPyr(FH)$_{2.3}$F, and 2.5 and 31.4 Ω for EMImBF$_4$. The values of R_{pore} reflect the ionic conductivity of these electrolytes, whereas the values of R_{bulk} do not. This is because that the R_{bulk} defined in this form contains the contribution of the other factor such as contact resistance. The formation of double-layer in the IPC was also confirmed by the behavior of impedance spectrum for DMPyr(FH)$_2$F as in the cases for EMPyr(FH)$_{2.3}$F and EMImBF$_4$. The large value of electrolyte resistance of DMPyr(FH)$_2$F lowers the cell voltage during the charge-discharge test at a high rate of 2380 mA g^{-1}, resulted in the low capacitance as shown in Figure 9–5 because the large IR drop suppresses the redox reactions.

9.3.4 Migration of ions in the pore of activated carbon electrode

When an activated carbon electrode is galvanostatically charged, the gradient of the applied potential along the depth direction in the pore gives an inhomogeneity in charging state, depending on the depth in the pore. Although the activated carbon at the top edge of the pore is charged sufficiently, the one at the bottom in the pore is not, resulting in the inhomogeneous distribution of charges and ions in the pore. An open-circuit voltage after the galvanostatic charging decreases by homogenization of the charge distribution in the pore with accompanying the diffusion of ions. In the diffusion-limited process of ions during homogenization, the open-circuit voltage (V_{oc}) decreases proportionally to the square root of time ($t^{1/2}$) [30]. Figures 9–7 (a), (d), and (g) show time (t) dependence of V_{oc} in electrochemical capacitors using DMPyr(FH)$_2$F, EMPyr(FH)$_{2.3}$F, and EMImBF$_4$, respectively, after charging up to 1 V at a current density of 238 mA g^{-1}. The respective IR drops of the cell due to the bulk electrolyte resistance are 11, 6, and 9 mV, respectively. Figures 9–7 (b), (e), and (h) show the relation between V_{oc} and $t^{1/2}$, and Figures 9–7 (c), (f), and (i) are the

magnifications of (b), (e), and (h). The linear decrease in V_{oc} against $t^{1/2}$ during the early 10 seconds is observed for DMPyr(FH)$_2$F and EMImBF$_4$ in Figures 9–7 (c) and (i), respectively, indicating the migration of ions in the pore occurs in the IPC phase of DMPyr(FH)$_2$F and the IL phase of EMImBF$_4$. This linear decrease in V_{oc} against $t^{1/2}$ in this time region is not observed for EMPyr(FH)$_{2.3}$F due to its low R_{pore}.

According to the literature [30], the relation between t and V_{oc} suggests the mechanism of self-discharge; (i) a linear correlation between V_{oc} and $t^{1/2}$ in a diffusion process, (ii) a linear correlation between V_{oc} and $\log(t)$ in a Faradaic process, and (iii) a linear correlation between $\log(V_{oc})$ and t in an ohmic leakage. Figure 9–8 shows the relations between V_{oc} and $\log(t)$ and between $\log(V_{oc})$ and t in electrochemical capacitors utilizing DMPyr(FH)$_2$F, EMPyr(FH)$_{2.3}$F, and EMImBF$_4$, respectively. The linear correlation between V_{oc} and $\log(t)$ for fluorohydrogenate salts after the early several minutes is observed in Figures 9–8 (a) and (c), suggesting that the self-discharge of the electrochemical capacitors using them as the electrolytes is caused mainly in the Faradaic process.

References

[1] N. A. Choudhury, S. Sampath, A. K. Shukla, Energy Environ. Sci. **2009**, *2*, 55.

[2] A. Bhide, K. Hariharan, J. Power Sources **2006**, *159*, 1450.

[3] K. Naoi, M. Morita, *Electrochem. Soc. Interface* **2008**, *Spring*, 44.

[4] A. Lewandowski, A. Świderska, *Solid State Ionics* **2003**, *161*, 243.

[5] C. A. Vincent, Prog. *Solid State Chem.* **1987**, *17*, 145.

[6] T. Kanbara, M. Inami, T. Yamamoto, *J. Power Sources* **1991**, *36*, 87.

[7] P. Lightfoot, M. A. Mehta, P. G. Bruce, *Science* **1993**, *262*, 883.

[8] F. B. Dias, L. Plomp, J. B. J. Veldhuis, *J. Power Sources* **2000**, *88*, 169.

[9] D. J. Bannister, G. R. Davies, I. M. Ward, J. E. McIntype, *Polymer* **1984**, *25*, 1291.

[10] A. M. Stephan, *Eur. Polym. J.* **2006**, *42*, 21.

[11] T. Nagatomo, C. Ichikawa, O. Omoto, *J. Electrochem. Soc*. **1987**, *134*, 305.

[12] K. M. Abraham, M. Alamgir, *J. Electrochem. Soc*. **1990**, *137*, 1657.

[13] D. Peramunage, D. M. Pasquariello, K. M. Abraham, *J. Electrochem. Soc*. **1995**, *142*, 1789.

[14] A. M. Sukeshini, A. Nishimoto, M. Watanabe, *Solid State Ionics* **1996**, *86–88*, 385.

[15] M. Alamgir, K. M. Abraham, *J. Electrochem. Soc.* **1993**, *140*, L96.

[16] G. G. Cameron, M. D. Ingram, K. Sarmouk, *Eur. Polym. J*. **1990**, *26*, 1097.

[17] J. Y. Song, Y. Y. Wang, C. C. Wan, *J. Electrochem. Soc*. **2000**, *147*, 3219.

[18] M. Aoki, K. Tadanaga, M. Tatsumisago, *Electrochem. Solid-State Lett*. **2010**, *13*, A52.

[19] N. A. Choudhury, A. K. Shukla, S. Sampath, S. Pitchumani, *J. Electrochem. Soc*. **2006**, *153*, A614.

[20] A. Lewandowski, A. Świderska, *Appl. Phys. A* **2006**, *82*, 579.

[21] J. Fuller, A. C. Breda, R. T. Carlin, *J. Electrochem. Soc*. **1997**, *144*, L67.

[22] Z. Li, H. Liu, Y. Liu, P. He, J. Li, L. Zheng, J. Li, *Polymer* **2005**, *46*, 7578.

[23] W. Lu, K. Henry, C. Turchi, J. Pellegrino, *J. Electrochem. Soc*. **2008**, *155*, A361.

[24] A. Senda, K. Matsumoto, T. Nohira, R. Hagiwara, *J. Power Sources* **2010**, *195*, 4414.

[25] R. D. Levie, *Electrochim. Acta* **1963**, *8*, 751.

[26] M. Itagaki, S. Suzuki, I. Shitanda, K. Watanabe, H. Nakazawa, *J. Power Sources* **2007**, *164*, 415.

[27] R. Taniki, K. Matsumoto, R. Hagiwara, K. Hachiya, T. Morinaga, T. Sato, *J. Phys. Chem. B* **2013**, *117*, 955.

[28] K. Matsumoto, R. Hagiwara, Y. Ito, *Electrochem. Solid-State Lett*. **2004**, *7*, E41.

[29] A. B. McEwen, H. L. Ngo, K. LeCompte, J. L. Goldman, *J. Electrochem. Soc.* **1999**, *146*, 1687.

[30] B. E. Conway, *Electrochemical Supercapacitors: Scientific Fundamentals and Technological Applications*, Kluwer Academic/Plenum, New York, **1999**.
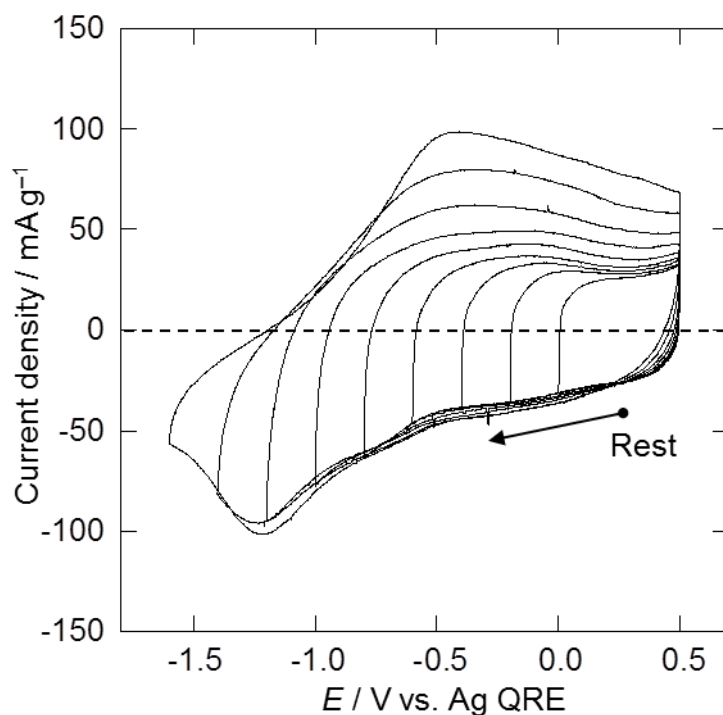
Figure 9–1. Cyclic voltammograms of an activated carbon electrode in the DMPyr(FH)$_2$F IPC.

Scan range: −1.6 and +0.5 V vs. Ag QRE. WE: Activated carbon. Scan rate: 0.2 mV s^{-1}.
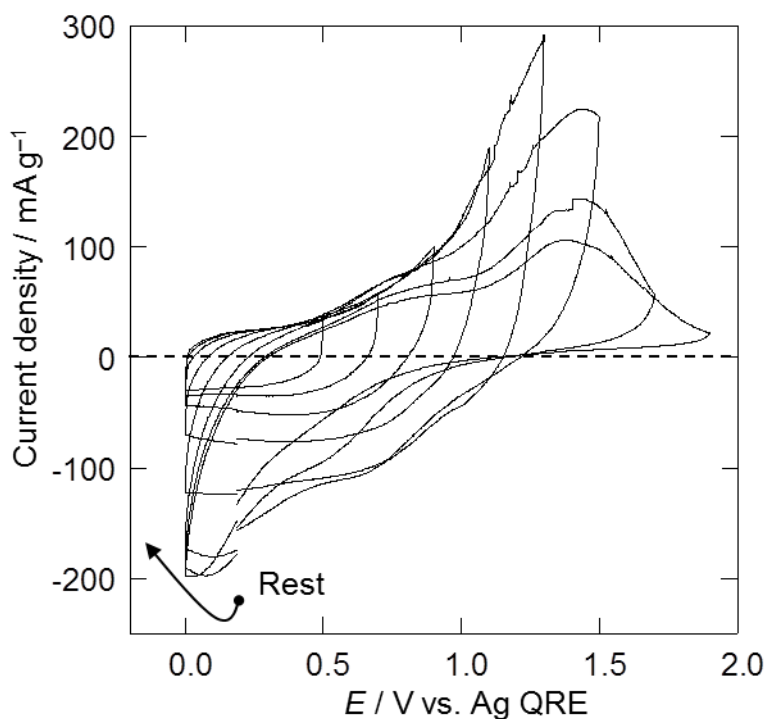
Figure 9–2. Cyclic voltammograms of an activated carbon electrode in the DMPyr(FH)$_2$F IPC.

Scan range: 0 and +1.9 V vs. Ag QRE. WE: Activated carbon. Scan rate: 0.2 mV s^{-1}.
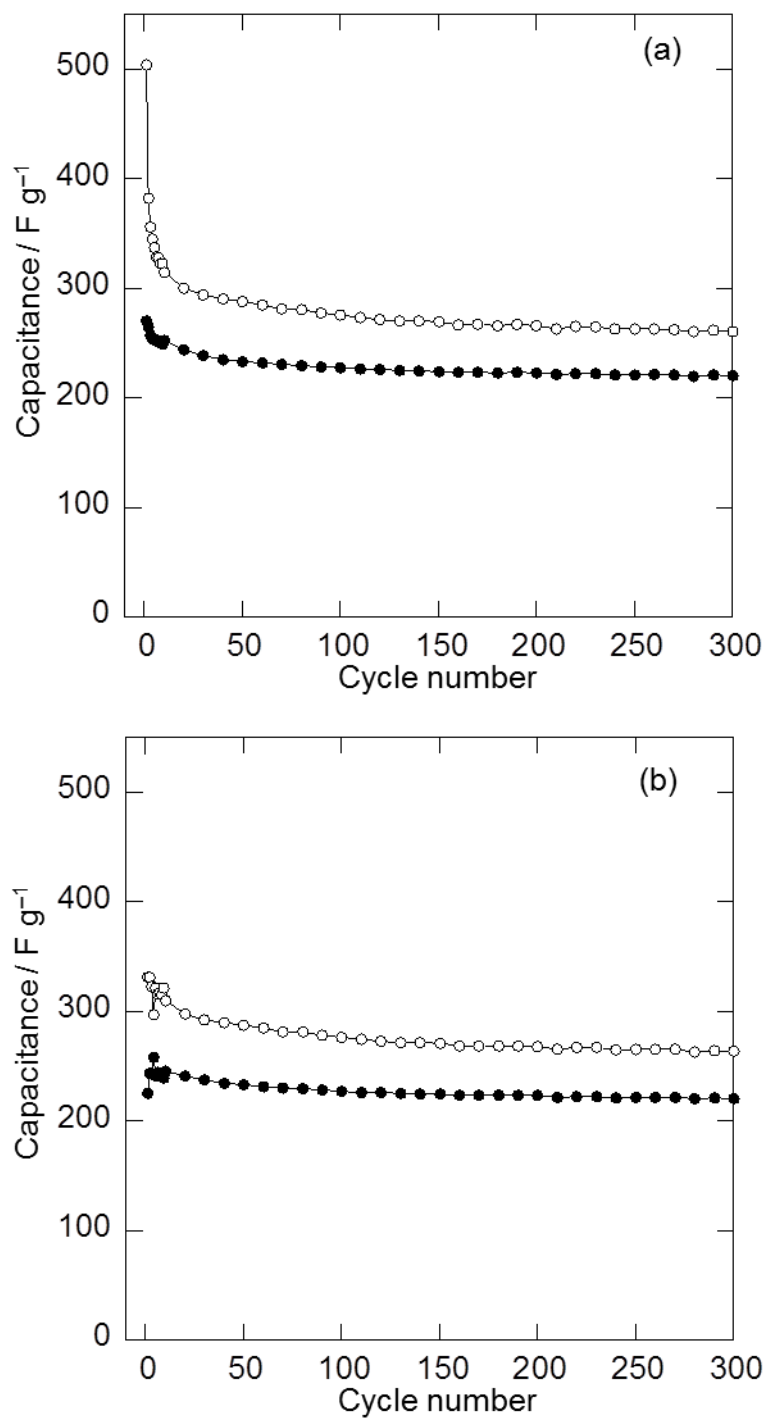
Figure 9–3. (a) Charge and (b) discharge capacitances of the activated carbon positive (○) and negative (●) electrodes in the DMPyr(FH)$_2$F IPC over 300 charge–discharge cycles at a current density of 238 mA g^{-1}.
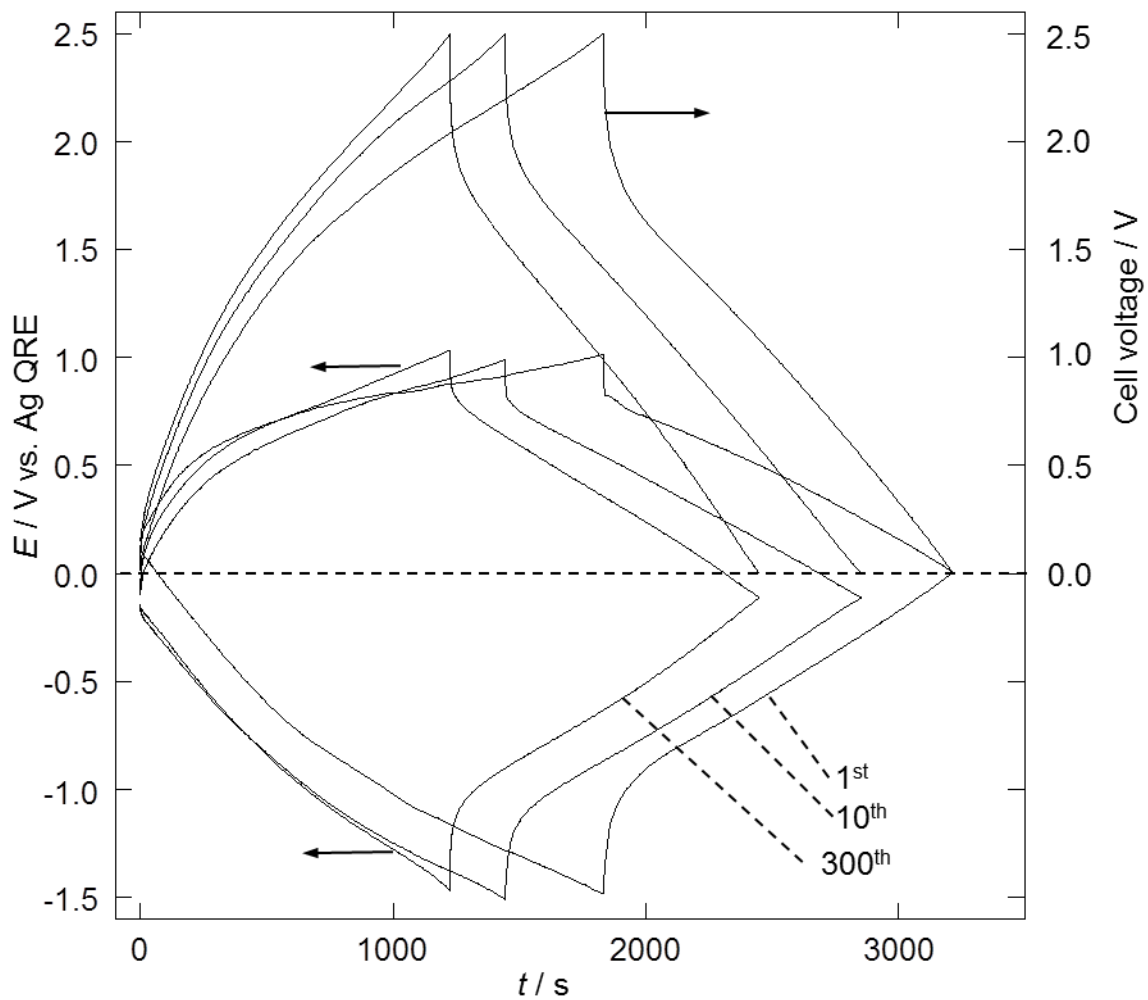
Figure 9–4. Charge–discharge curves of the cell, and activated carbon positive and negative electrodes in the DMPyr(FH)$_2$F IPC at the 1st, 10th, and 300th cycles at a current density of 238 mA g^{-1}.
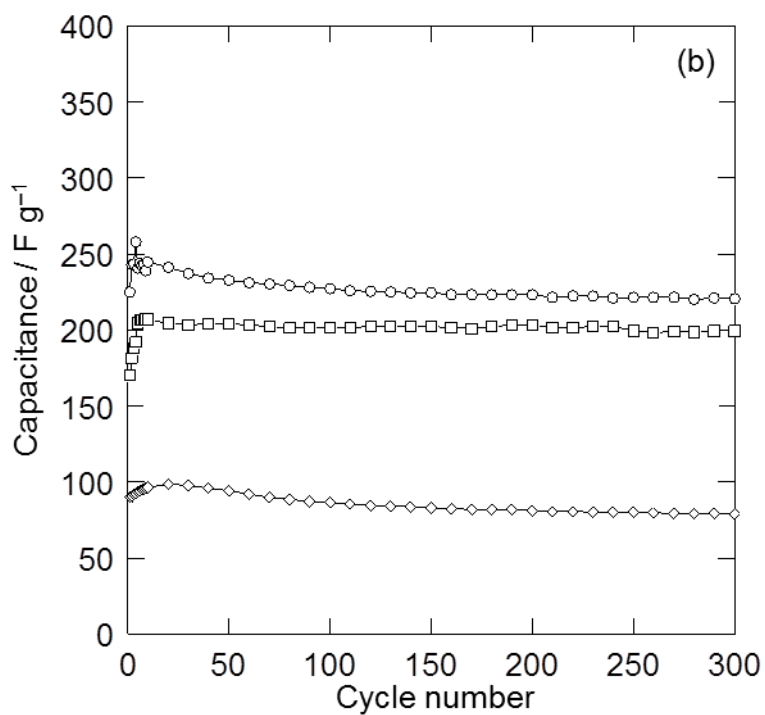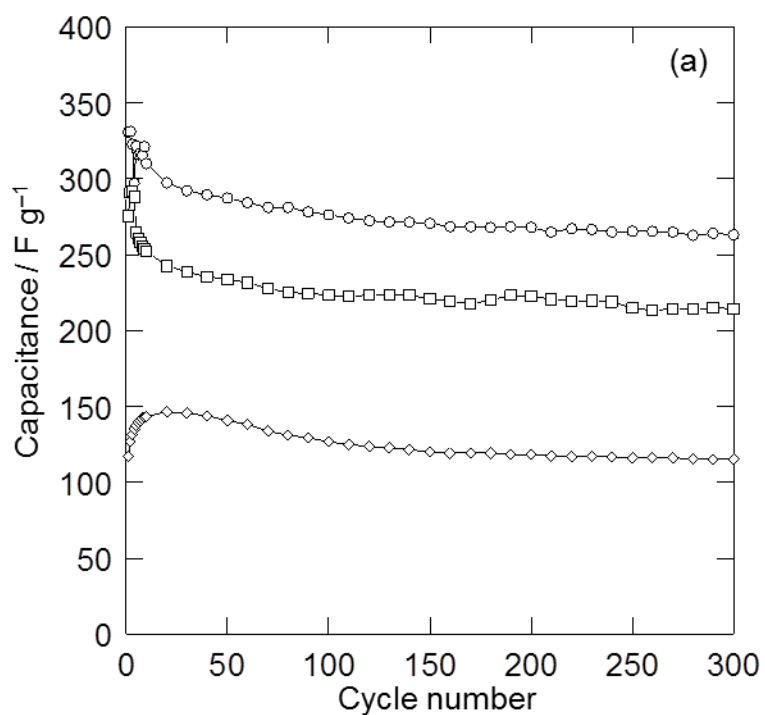
Figure 9–5. Discharge capacitances of the activated carbon (a) positive and (b) negative electrodes in the DMPyr(FH)$_2$F IPC ($\circ$: 238 mA g^{-1}, $\square$: 476 mA g^{-1}, and $\diamondsuit$: 2380 mA g^{-1}). The cycles correspond to that in Figure 9–3.

156
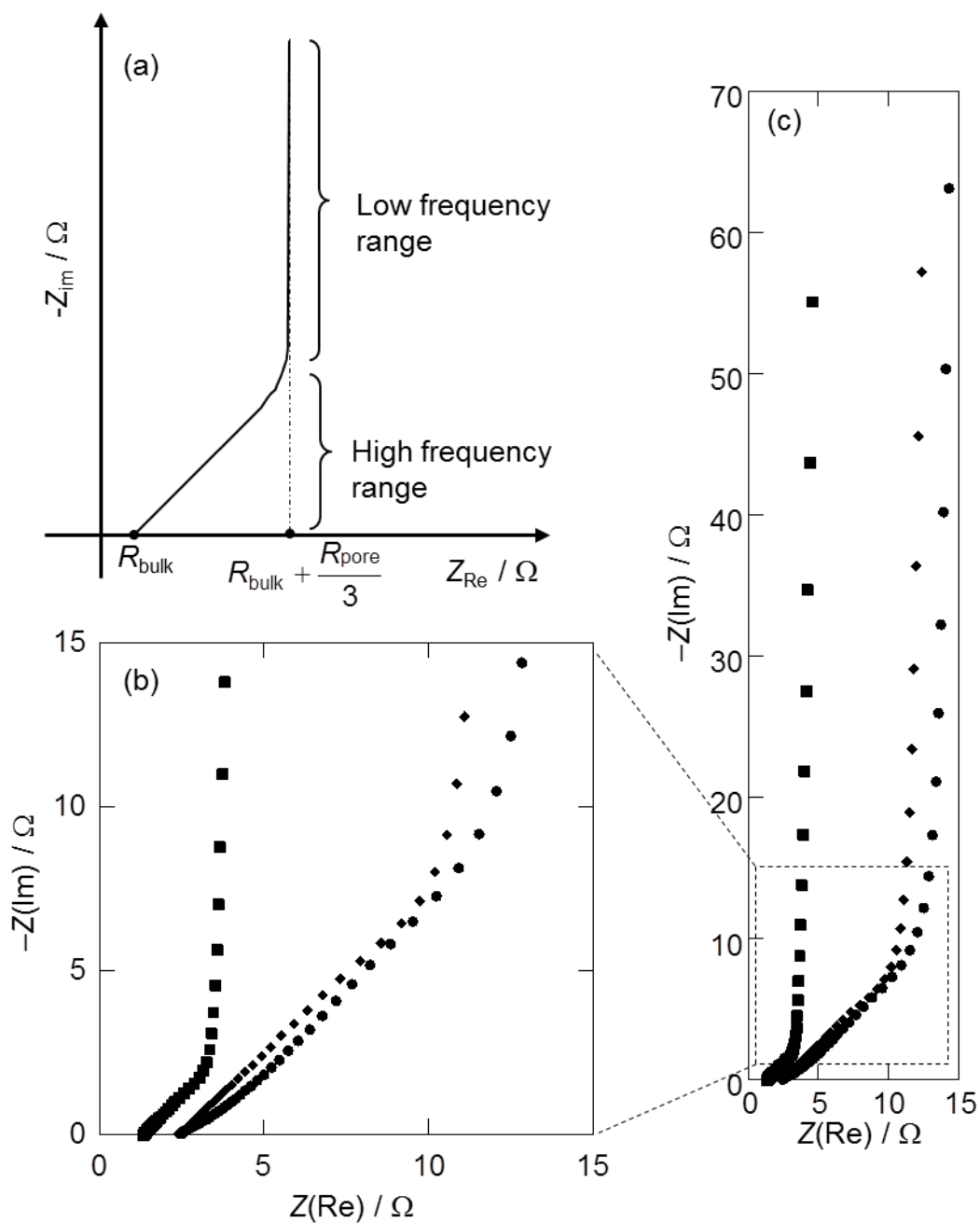
Figure 9–6. Nyquist plots of the impedance spectra for (a) a typical EDLC, (b), and (c) electrochemical capacitors using (♦) DMPyr(FH)$_2$F, (■) EMPyr(FH)$_{2.3}$F, and (●) EMImBF$_4$ at the rest potential. The frequency ranges from 10 kHz to 2 mHz.
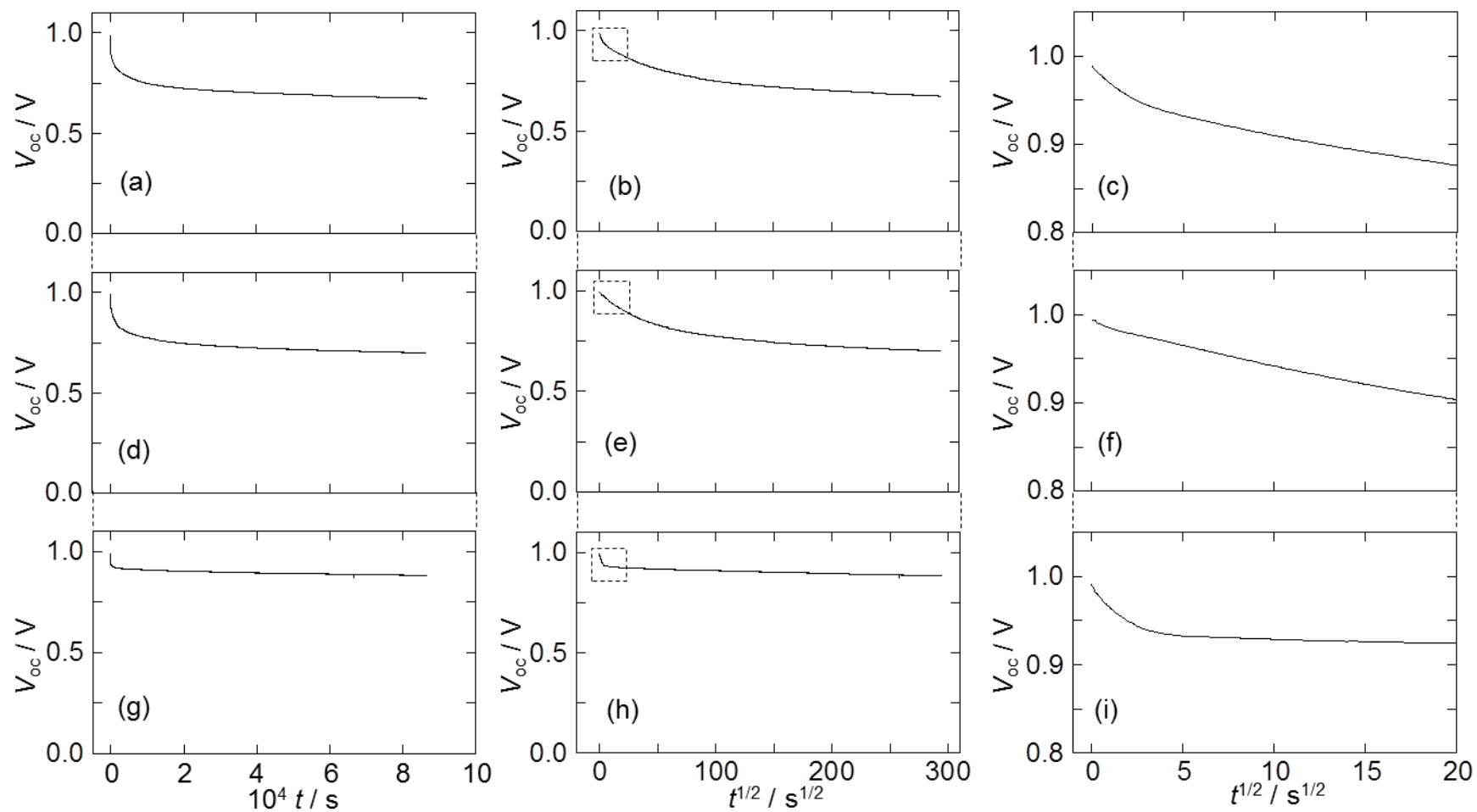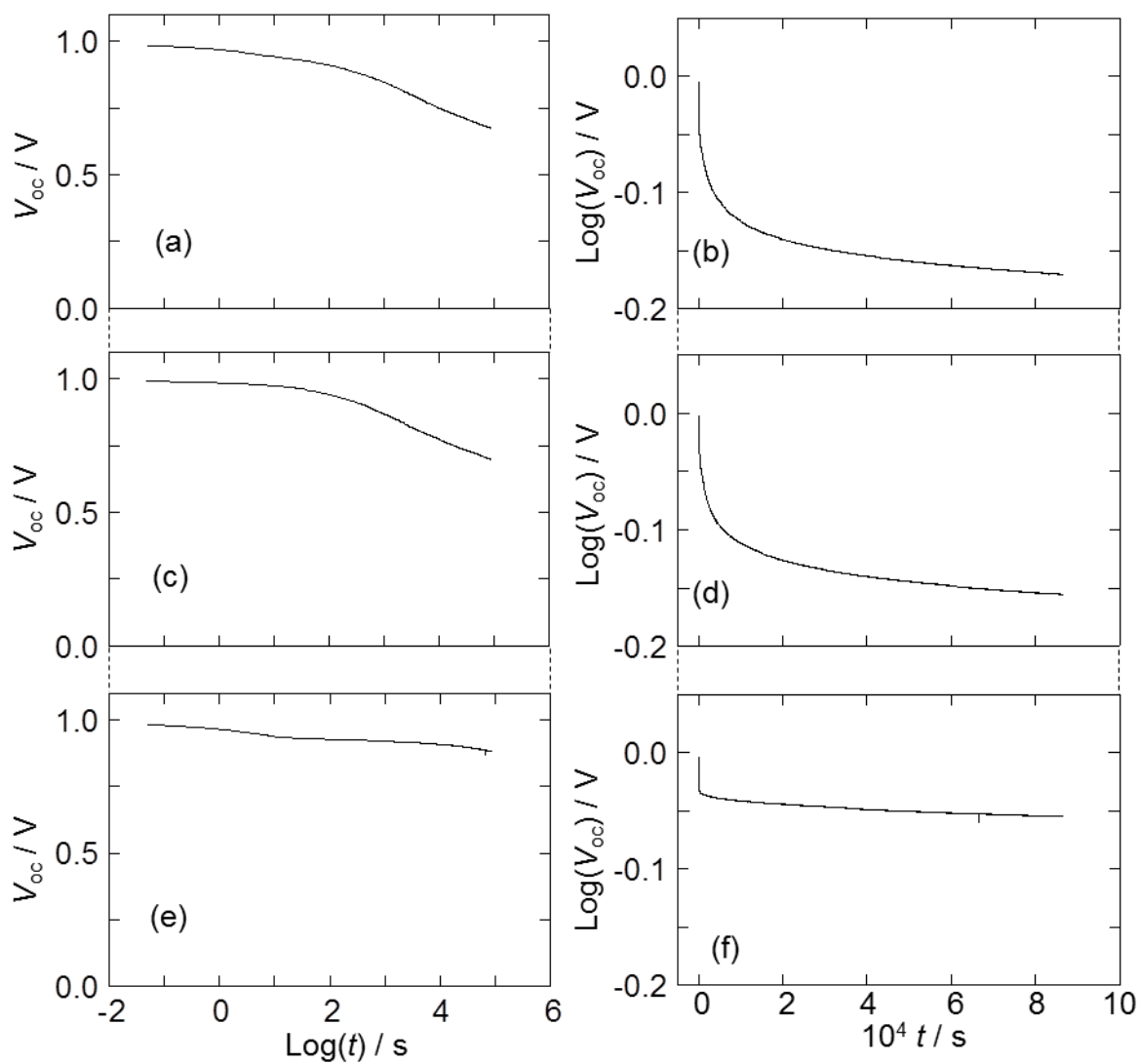
Figure 9–7. Relation between V_{oc} and t and between V_{oc} and $t^{1/2}$ in electrochemical capacitors utilizing DMPyr(FH)$_2$F [(a), (b), and (c)], EMPyr(FH)$_{2.3}$F [(d), (e), and (f)], and EMImBF$_4$ [(g), (h), and (i)], respectively, where (c), (f), and (i) are the magnifications of dotted domains in (b), (e), and (h).

Figure 9–8. Relation between V_{oc} and log(t) and between log(V_{oc}) and t in electrochemical capacitors utilizing DMPyr(FH)$_2$F [(a) and (b)], EMPyr(FH)$_{2.3}$F [(c) and (d)], and EMImBF$_4$ [(e) and (f)], respectively.

Chapter 10

General conclusion

In this study, a variety of fluorohydrogenate salts were synthesized and characterized in view of applications as electrolytes in electrochemical devices. In the former part, new FHILs and FHIPCs based on pyrrolidinium cation, sulfonium cation, azoniaspiro-type cation, and polyalkylimidazolium cation were synthesized and their physicochemical and structural properties were investigated. The latter part deals with detailed electrochemical behavior of activated carbon electrodes in $EMPyr(FH)_{2.3}F$ FHIL and $DMPyr(FH)_{2.0}F$ FHIPC electrolytes for application to electrochemical capacitor. Experimental details on the analyses and apparatus used in this study were summarized in Chapter 2.

In Chapter 3, new IPCs based on fluorohydrogenate anions were prepared, and their physicochemical, structural, and electrochemical properties were investigated. The fluorohydrogenate salts $DMPyr(FH)_{2.0}F$ and $EMPyr(FH)_{2.0}F$ have IPC phases in the temperature ranges of 258–325 and 236–303 K, respectively. These phases have NaCl-type structures and exhibit small entropy changes of fusion. The ionic conductivities of the IPC phases are the highest known for IPC phases, ranging from 10^0 to 10^1 mS m^{-1}. Pulsed-field gradient spin–echo NMR spectroscopy revealed that the anion can move in the IPC phase as a charge carrier. The $DMPyr^+$, without mibility, holds the IPC lattice structure of $DMPyr(FH)_{2.0}F$ and supports the transportation of the anion by rotating locally, whereas a part of $EMPyr^+$ ions are mobile in the IPC lattice while the other cations are fixed to the framework of the crystal lattice. The behavior observed is presumably caused by the difference in the packing of ions in the IPC lattice of $EMPyr(FH)_2F$ and $DMPyr(FH)_2F$, the former being looser than the latter.

In Chapter 4, effects of n in $EMPyr(FH)_nF$ ($1.0 \leq n \leq 2.3$) and $DMPyr(FH)_nF$ ($1.0 \leq n \leq$

2.0) on the thermal and structural properties were discussed. In the EMPyr(FH)$_n$F system, several solid phases, IPC (I) phase, IPC (II) phase, crystal phases of EMPyr(FH)$_1$F, EMPyr(FH)$_2$F, and EMPyr(FH)$_3$F, were observed. The IPC (I) and IPC (II) phases form IPCs with randomly distributed anions in the lattice with wide composition range of HF in (FH)$_n$F$^-$. Melting point of EMPyr(FH)$_n$F in the range of $1.8 \leq n \leq 2.3$ becomes maximal at $n = 2.0$, that of $1.3 \leq n \leq 1.7$ does not change around $260 - 270$ K, and that of $1.0 \leq n \leq 1.2$ increases with decrease in HF content. In the DMPyr(FH)$_n$F system, IPC (I') phase, crystal phases of DMPyr(FH)$_1$F and DMPyr(FH)$_2$F, were observed. The IPC (I') phase also forms the IPC with randomly distributed anions in the lattice with the wide composition range of HF in (FH)$_n$F$^-$. Melting point increases with decrease in HF content. The differences in thermal properties between EMPyr(FH)$_n$F and DMPyr(FH)$_n$F are conceivably due to the existence of mobile EMPyr$^+$ cations in the IPC (I) of EMPyr(FH)$_n$F and absence of mobile DMPyr$^+$ cations in the IPC (I') of DMPyr(FH)$_n$F.

In Chapter 5, new fluorohydrogenate salts based on azoniaspiro-type cations, AS[4.4](FH)$_{2.0}$F, AS[4.5](FH)$_{2.0}$F, AS[5.5](FH)$_{2.0}$F, AS[4.2O2](FH)$_{1.9}$F, AS[5.2O2](FH)$_{2.0}$F, AS[2O2.2O2](FH)$_{2.0}$F, DEPyr(FH)$_{2.0}$F, and N$_{2222}$(FH)$_{2.0}$F, were synthesized and characterized. The increase in the number of the rings in cations raises the thermal stability. The increase in the number of carbon atoms in the ring from 4 to 5 slightly lowers the thermal stability. The AS[$x.y$](FH)$_n$F salts without oxygen atom in the ring have higher thermal stability than those with oxygen atom. The introduction of the ring structure lowers the melting point in the case of fluorohydrogenate salts. The decrease in the number of carbon atoms in the cation decreases the melting point. Introduction of oxygen atom to azoniaspiro cations lowers the melting point. Physicochemical properties were examined for the two salts giving RTILs, AS[4.4](FH)$_{2.0}$F and AS[4.2O2](FH)$_{1.9}$F.

In Chapter 6, trialkylsulfonium fluorohydrogenate ionic liquids (S$_{111}$(FH)$_{1.9}$F, S$_{112}$(FH)$_{2.0}$F,

161

$S_{122}(FH)_{2.0}F$, and $S_{222}(FH)_{2.0}F$) were reported. The vacuum–stable HF composition in the anion differs, depending on the cationic structure. The world record ionic conductivity at 298 K to date is observed for $S_{111}(FH)_{1.9}F$ (131 mS cm^{-1}). The ionic conductivity decreases in the order of $S_{111}(FH)_{1.9}F > S_{112}(FH)_{2.0}F$ (111 mS cm^{-1}) $> S_{122}(FH)_{2.0}F$ (91 mS cm^{-1}) $> S_{222}(FH)_{2.0}F$ (83 mS cm^{-1}). Electrochemical windows of $S_{111}(FH)_{1.9}F$, $S_{112}(FH)_{2.0}F$, $S_{122}(FH)_{2.0}F$, and $S_{222}(FH)_{2.0}F$ are 4.09, 4.20, 4.37 and 4.93 V, respectively.

In Chapter 7, new fluorohydrogenate salts based on $C_{(x+2)F(2x+1)}MIm(FH)_nF$ were synthesized and characterized. These salts are miscible with water. Three RTILs were obtained; $C_{3F3}MIm(FH)_{1.7}F$ (T_m: 274 K) $C_{4F5}MIm(FH)_{1.7}F$ (T_g: 186 K), and $C_{6F9}MIm(FH)_{1.8}F$ (T_m: 276 K), whereas the other salts, $C_{8F13}MIm(FH)_{2.0}F$ and $C_{10F17}MIm(FH)_{2.0}F$, were in the crystal phase at room temperature. The introduction of fluorine atoms resulted in the increase in the density and viscosity, decrease in the ionic conductivity, and lower electrochemical stability against reduction. The liquid crystal phase was observed in $C_{8F13}MIm(FH)_{2.0}F$ and $C_{10F17}MIm(FH)_{2.0}F$. Introducing fluorine atoms to the side-chain promotes the formation of the liquid crystal phase, whereas the interdigitation of polyfluoroalkyl side-chains does not occur in the crystal phase.

In Chapter 8, the double-layer and redox capacitances of positive and negative activated carbon electrodes in $EMPyr(FH)_{2.3}F$ were evaluated based on charge–discharge tests, cyclic voltammetry, and ac impedance spectroscopy. The Faradaic reactions differ at the positive and negative electrodes, and both reactions contribute to the large voltage dependence of the capacitance. The most conceivable reaction at the positive electrode is the oxidation of carbon accompanied by absorption of $(FH)_nF^-$ or F^- and the corresponding reduction. The most probable reaction at the negative electrode is the reduction of $(FH)_nF^-$ to generate atomic hydrogen on the activated carbon and the corresponding oxidation of atomic hydrogen with $(FH)_nF^-$. In the case of charging up to 2.5 V at a current density of 238 mA g^{-1}, the

double-layer capacitance and redox capacitances of the positive electrode are 140 and 150 F g^{-1}, respectively. Correspondingly, the negative capacitance is the sum of the double-layer capacitance of 130 F g^{-1} and the redox capacitance of 116 F g^{-1}.

In Chapter 9, the behavior of the activated carbon electrode in FHIPC DMPyr(FH)$_{2.0}$F was investigated by charge–discharge tests, cyclic voltammetry, ac impedance spectroscopy, and self-discharge test. The square shapes corresponding to the formation and deformation of electric double-layer in cyclic voltammetry were observed in the IPC phase of FHIPC DMPyr(FH)$_{2.0}$F for positive and negative electrodes. The redox reactions on both the electrodes occur in the similar potential to that of the electrochemical capacitors using FHIL EMPyr(FH)$_{2.3}$F. Stable operation of the electrochemical capacitor using FHIPC DMPyr(FH)$_{2.0}$F was confirmed for 300 cycles and the capacitances of the positive and negative electrodes at the 300th cycle were 263 and 221 F g^{-1}, respectively. Migrations of ions in the pore of activated carbon electrode were observed by the impedance analysis and self-discharge test.

List of publications

Chapter 3

Ryosuke Taniki, Kazuhiko Matsumoto, Rika Hagiwara, Kan Hachiya, Takashi Morinaga, Takaya Sato

The Journal of Physical Chemistry B **2013**, *117*, 955–960.

"Highly conductive plastic crystals based on fluorohydrogenate anions"

Chapter 4

Ryosuke Taniki, Kazuhiko Matsumoto, Rika Hagiwara

To be submitted.

"Pyrrolidinium based fluorohydrogenate salts with different HF contents"

Chapter 5

Ryosuke Taniki, Kazuhiko Matsumoto, Rika Hagiwara

To be submitted.

"Fluorohydrogenate ionic liquids based on azoniaspiro-type cations"

Chapter 6

Ryosuke Taniki, Kazuhiko Matsumoto, Rika Hagiwara

Electrochemical and Solid-State Letters **2012**, *15*, F13–F15.

"Trialkylsulfonium fluorohydrogenate giving the highest conductivity in room temperature ionic liquids"

Chapter 7

Ryosuke Taniki, Naoki Kenmochi, Kazuhiko Matsumoto, Rika Hagiwara

Journal of Fluorine Chemistry **2013**, *149*, 112–118.

"Effects of the polyfluoroalkyl side-chain on the properties of 1-methyl-3-polyfluoroalkylimidazolium fluorohydrogenate ionic liquids"

Chapter 8

Ryosuke Taniki, Kazuhiko Matsumoto, Toshiyuki Nohira, Rika Hagiwara

Journal of The Electrochemical Society **2013**, *160*, A734–A738.

"Evaluation of Double-Layer and Redox Capacitances of Activated Carbon Electrodes in *N*-ethyl-*N*-methylpyrrolidinium fluorohydrogenate Ionic Liquid"

Chapter 9

Ryosuke Taniki, Kazuhiko Matsumoto, Toshiyuki Nohira, Rika Hagiwara

To be submitted.

"Electrochemical capacitor utilizing fluorohydrogenate ionic plastic crystal"

Acknowledgement